Experimental investigation of Vortex Beams for inter-satellite Free Space Optical Communications

Thesis Report

Edward Pauwels 4491149

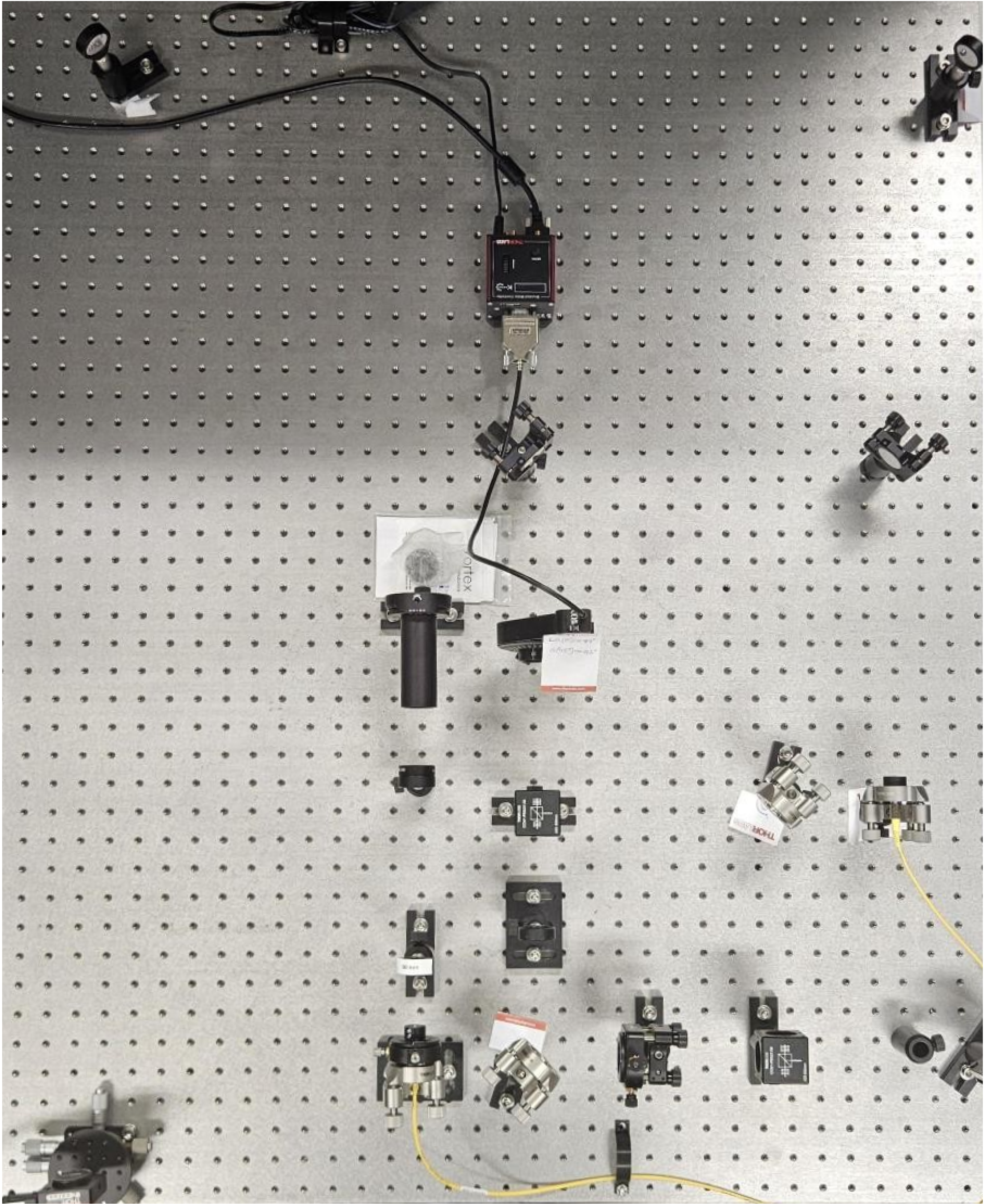

Contents

Abstract

Free-Space Optical Communication (FSOC) governs the use of lasers to communicate over often large distances in the open air. This technology has emerged as a promising alternative to traditional radio-frequency communication for inter-satellite links as the higher electromagnetic frequencies offer higher bandwidth, improved security, reduced system mass and reduced power requirements. Despite these advantages, FSOC systems remain highly sensitive to pointing errors due spacecraft-induced jitter, which can significantly degrade link performance. Recent theoretical work has proposed the use of non-Gaussian beams, specifically combinations of Laguerre-Gaussian modes, to mitigate jitter-induced power bit error rate and power outage probability.

This thesis presents an experimental investigation of such beam superpositions for FSOC. An experimental optical setup was proposed and implemented to generate specific combinations of Gaussian and Laguerre-Gaussian beams using polarising beam splitters and a spiral phase plate. In parallel, a pre-existing propagation simulation program using the principles of Fourier optics and a number of its approximations such as Fresnel and Fraunhofer, was extended to model beam propagation and component misalignment of the experimental setup. Experimental measurements were then systematically compared to both simulated and theoretical beam profiles.

The obtained beam profiles, both measured and simulated, were subjected to similar power outage probability analysis as the Laguerre-Gaussian profile in the theory, and from this it could be concluded that while the experimental profiles performed worse than the theoretical, they still outperformed the original fundamental Gaussian profile by over an order of magnitude.

The decrease in power outage probability meant that in theory the power of the source could be lowered and still perform to industry norms. The experiment's beam shaping section operated at 83.4% throughput, a loss of power which did not negate the theoretical power gains of up to 40%. This loss was introduced by the beam shaping components such as the polarising beam splitters and the spiral phase plate, but did not override the theoretical gains in communication stability obtained by using these specific beam profiles, thus showing the potential in this type of system.

During the verification and validation of both the programs and the experimental setup, it was shown that the beams produced by the experiment and those produced by the simulation program matched closely with an R^2 value of over 0.9, however the propagation distance possible was not sufficient to allow the beam to fully develop. In addition, it was discovered that the vortex beam produced by a spiral phase plate was not in fact a pure Laguerre-Gaussian beam as assumed, but instead a closely resembling vortex beam with orbital angular momentum. Since over 80% of the produced vortex beam's intensity distribution matched that of a Laguerre-Gaussian beam of the same charge as the spiral phase plate, it was taken as a sufficient approximation and further research into this discrepancy was proposed as future work.

After the beam intensity profile had successfully been analysed and modelled, the simulation program could also compute the results of misalignment, both displacement and rotation, of various components in order to perform a sensitivity analysis, the results of which matched what was seen in the lab. The simulation program could then be used to determine the real misalignment of components and thus resulted in better aligned measurements. The spiral phase plate proved to be highly sensitive to linear displacement where the centre of the impinging beam does not align with the centre of the spiral phase plate, but only slightly sensitive to rotational errors about the vertical axis.

Overall, the findings obtained during this thesis project provide experimental validation of the proposed concept and offer practical insights into the feasibility of non-Gaussian beam shaping as a robustness-enhancing technique for future FSOC systems, while presenting interesting ideas for future development.

List of Abbreviations and Symbols

Abbreviations

FSOC	Free-Space Optical Communication
RF	Radio Frequency
G	Gaussian
LG	Laguerre-Gaussian
HG	Hermite-Gaussian
IG	Ince-Gaussian
OAM	Orbital Angular Momentum
HWP	Half-Wave Plate
SPP	Spiral Phase Plate
PBS	Polarising Beam Splitter
PBC	Polarising Beam Combiner
OD	Optical Density
LP	Linear Polariser
MFD	Mode Field Diameter
NA	Numerical Aperture
PDF	Probability Density Function
BER	Bit Error Rate
POP	Power Outage Probability

Symbols

C	Channel Capacity [$bits/s$]
B	Bandwidth [Hz]
S	Signal Power [W]
N	Noise [W]
θ	Angle [rad or °]
λ	Wavelength [m]
D	Aperture size [m]
I	Intensity [W/m^2]
$\Delta\phi$	Phase retardation [rad]
n	Refractive index [$-$]
t	thickness [m]
h	Height [m]
ℓ	Charge of vortex [$-$]
k	Wavenumber [m^{-1}]
w_0	Beam Waist [m]

w	Beam radius $[m]$
R	Radius of Curvature $[m]$
z_R	Rayleigh Range $[m]$
η	Efficiency $[-]$
R^2	Coefficient of determination $[-]$
E	Electric Field Distribution $[V/m]$
z	Propagation Distance $[m]$
L_p^ℓ	Generalised Laguerre Polynomial
ψ	Gouy Phase
p	Order of Laguerre-Gaussian $[-]$
ϵ_0	Permittivity of free space $[-]$
P	Power $[W]$

Preface

This paper serves as the conclusion to my master thesis project of the Space Engineering Master at Delft University of Technology. This thesis was performed under the supervision of Pierre Piron and Mario Badás Aldecocea at the Space Instrumentation group.

I would like to express my sincere gratitude to both of my supervisors, for their invaluable guidance, for their willingness to help at all times of the day and week and for allowing me to have this unforgettable experience.

I would like to thank the TTW-FREE Optical Wireless Superhighways NWO perspective program for their financial contribution.

I would like to thank Eva, for being an amazing partner and always standing by my side. I would also like to thank my parents, for always supporting me and believing in me after all this time.

Thank you to my friends, for enduring my endless discussions about topics that few understand (and even fewer care about).

And finally thank you to everyone who helped during this project, Fabien Schmutz the lab technician, the other members of the Space Instrumentation group, other optics experts at the university, and the people at Vortex Photonics. Without your combined effort this project would not have been possible.

Edward Pauwels

1

Introduction

The rapidly increasing demand for high-data-rate communication between spacecraft has driven the development of alternatives to conventional radio-frequency systems. Free-Space Optical Communication (FSOC), using laser beams to transmit information through free space (i.e. air, water or vacuum as compared to fiber-optic cables), offers several compelling advantages over radio frequency communication. These include, but are not limited to, significantly higher available bandwidth, narrower beam divergence, enhanced link security and reduced size, mass, and power requirements. As a result, FSOC has become a key technology for future space communication architectures, improving inter-satellite relay networks, deep-space missions, and satellite-ground communication infrastructures.

Despite these advantages, FSOC systems face a number of challenges that limit their operational effectiveness. Due to the narrow beam divergence of optical links, even small pointing errors can result in large fluctuations in received power or complete link loss. While slow pointing errors can be corrected using attitude control and beam steering mechanisms, higher-frequency jitter, arising from sources such as reaction wheels, moving mechanisms and thermal effects, remains difficult to mitigate. Over long inter-satellite distances, these micro-vibrations on a transmitter can lead to significant deviations of the centre of the beam from the receiver aperture and significantly degrade communication performance metrics such as bit error rate and power outage probability.

Most existing FSOC systems use fundamental Gaussian beams, which are optimal in terms of minimal divergence but are particularly sensitive to misalignment since their peak intensity lies at their centre, and any pointing error then leads away from this peak causing less total power to be received. Recent theoretical research has proposed the use of alternative beam profiles, such as Laguerre-Gaussian beams or superpositions of multiple profiles, to reduce sensitivity to this pointing jitter [1]. Among the various non-Gaussian beam profiles, Laguerre-Gaussian beams are characterised by their annular shape and orbital angular momentum in their phase. Two parameters, the charge ℓ and order p, determine the size and amount of rings in the profile respectively.

By redistributing optical power away from the beam centre, these non-Gaussian beams may offer better performance characteristic under jitter-dominated conditions. However, these theoretical gains do not account for the additional optical components required to generate such beams, which introduce losses, aberrations, and alignment sensitivities of their own.

The primary objective of this thesis is to experimentally investigate the feasibility of using Gaussian-Laguerre-Gaussian beam superpositions for inter-satellite FSOC, based on a preceding paper [1].

Specifically, this work aims to answer the following research questions:

- **Do the additional optical components required for vortex beam generation introduce losses that outweigh the theoretically predicted performance gains?**
- **How closely do experimentally generated beam profiles match numerical simulations and theoretical models?**
- **Does the experimentally observed communication-relevant performance align with theoretical expectations?**

To address these questions, an experimental optical bench setup was designed to generate and analyse superposed Gaussian and Laguerre-Gaussian beams. Comprehensive simulation and analysis programs were developed to model the experimental setup and quantitatively compare experimental results to theory.

The experimental setup was based upon a setup proposed by Badás et al. [1], and was adapted and expanded upon using components already available in the lab where possible, while some crucial components had to be purchased. In this proposed setup, a Gaussian beam was linearly polarised and then split into two orthogonally polarised beams. One of these beams would then impinge upon a spiral phase plate, after which both beams would be superposed and propagate to a sensor. It was assumed that a spiral phase plate interacting with a Gaussian beam would create a Laguerre-Gaussian beam, an assumption that would eventually be discovered to be wrong.

The thesis is structured as follows: first, chapter 2 provides background theory on FSOC, beam shapes and how to create these shapes. Chapter 3 then describes the optical propagation and beam analysis programs, the theory behind them and how they functioned. chapter 4 details the experimental setup and iterations it went through such as modal filtering by use of fiber coupling, while chapter 5 presents verification and validation results of both the programs and the experimental setup itself as well as a sensitivity analysis for misaligned components and beam development. Finally, chapter 6 discusses the experimental results, their implications for FSOC system design and offers ideas for future research.

2

Background

In this chapter, a state of the art review of Free-Space Optical Communication (FSOC) is given and its current challenges and future development are explored. This knowledge will then be used to determine an appropriate subject for this thesis to study and lay out the research questions. First, a brief history of FSOC is given to gain an understanding of the current capabilities. Then, the working principles and structure of a typical FSOC system are discussed. From this, the current challenges of FSOC systems can be understood. Finally, the concept of beam shaping, which will be crucial to this project, is laid out and the most relevant beam shape families are explored.

2.1. Free-space optical communication

The laser was officially invented in 1958 by C. Townes and A. Schawlow [2]. Only a few years later, in 1963, the first communication system using a laser travelling through open air from one end of an optical bench to another was demonstrated at Bell Labs [3] using a Helium-Neon laser with a wavelength of 633nm, giving it a red colour. While this was an important first step, the systems during this time suffered heavily from atmospheric disturbances and alignment issues, further discussed in section 2.3. Outside of the atmosphere these disturbances would be eliminated, but the typically large distances (hundreds or thousands of kilometres) involved made the alignment issues difficult to overcome.

In 1995, after significant improvements in adaptive optics, tracking equipment and laser sources, the Japanese space agency NASDA established the first space-to-ground optical communication link [4]. The geostationary satellite ETS-VI was equipped with a 20 kg experimental laser communication equipment system, and received an uplink beacon to establish a link and guide the pointing assemblies in steering the downlink laser. This test was devised to develop an inter-satellite link system and managed to maintain a 1 Mbps transfer rate for a maximum of 0.3 seconds at a time [5].

After the first successful demonstration of FSOC, the beginning of the twenty-first century has seen several missions using FSOC for both satellite-to-ground and inter-satellite communication. Table 2.1 summarises a few notable missions and why they represented a breakthrough in FSOC.

Year	Mission	Notable details	References
1995	ETS-VII	First satellite-to-ground link	[4, 5]
2005	Spot-4 & Artemis	First inter-satellite link	[6, 7]
2005	MESSENGER	Longest FSOC link (24 million km)	[8, 9]
2008	TerraSAR-X & NFIRE	First gigabit inter-satellite link	[10, 11]
2013	LRO	FSOC with a Lunar satellite	[12, 13]
2014	Scylight	Satellite-to-aircraft link	[14, 15]
2014	OPALS	Link re-establishment after cloud blocking	[16]
2015	Sentinel-1A & Alphasat	Demonstration of multi-nodal FSOC network	[17, 18]
2020	SOLISS	Bidirectional FSOC link between ground and ISS	[19, 20]
2022	TBIRD	200 Gbps optical downlink	[21]
2023	PSYCHE	Deep space optical communication (over 300 million km)	[22, 23]

Table 2.1: Table of notable space missions involving FSOC

While this list is far from complete, it shows the fast rate at which the field of FSOC in space flight is developing. Some missions are still ongoing, such as the PSYCHE mission, with the goal to study the asteroid Psyche at around 3 AU. Onboard the spacecraft is the Deep Space Optical Communications (DSOC) subsystem, having demonstrated deep space optical communication capabilities using a 1550nm (infrared) laser. As for future missions, JAXA has set its focus on miniaturisation of the technology for use on cubesats with its ETS-9 and CubeSOTA missions [24], while ESA and NASA are looking to expand their relay system to lunar space by way of the LunaNet initiative [25]. General Atomics and Kepler Communications announced in September 2025 a successful demonstration of an air-to-space optical communication system, linking the Kepler satellite with a flying aircraft [26].

2.2. Principles of FSOC

Ever since the first radio transmission in 1900, Radio Frequency (RF) communication technology has continued to develop. Due to its widespread use and rather limited frequency range of 3 kHz to 300 GHz, countries have had to cooperate and regulate who gets to use what frequency band and where [27]. This limited frequency range can have two effects: signals of similar frequency can overlap at the receiver and cause interference, while the Shannon-Hartley capacity theorem [28] puts a hard limit on the maximum amount of information that can be sent over a channel.

$$C = B\,\text{log}_2(1 + S/N) \tag{2.1}$$

where C is the channel capacity, B the bandwidth, S the received signal power and N the channel noise power.

Furthermore, RF signals spread out over large angles, reducing the received power and introducing security risks. Generally, the divergence angle of an electromagnetic wave is proportional to its wavelength and transmitter aperture size follows [29]

$$\theta_{\text{Div}} \propto \frac{\lambda}{D} \tag{2.2}$$

where θ_{Div} is the divergence angle, λ is the carrier wavelength and D the aperture diameter. Here it can be seen that in order to decrease the beamwidth the aperture or antenna must be made larger. This can be impractical in cases where size or cost are a limiting factor.

While for lasers the Shannon-Hartley capacity theorem also applies, the higher frequency range of existing laser sources [30], 10^6 to 10^8 Hz, allows for much higher modulation frequencies leading to a larger bandwidth. Laser beams also diverge less due to this higher frequency as they share the proportionality of the divergence angle in equation (2.2).

The narrow beam divergence and small wavelengths of lasers requires systems with very precise component alignment and the ability the accurately steer both in- and output beams. An example of such a system is represented by the block diagram of the ETS-VI's Laser Communication Equipment (LCE), shown in figure 2.1.

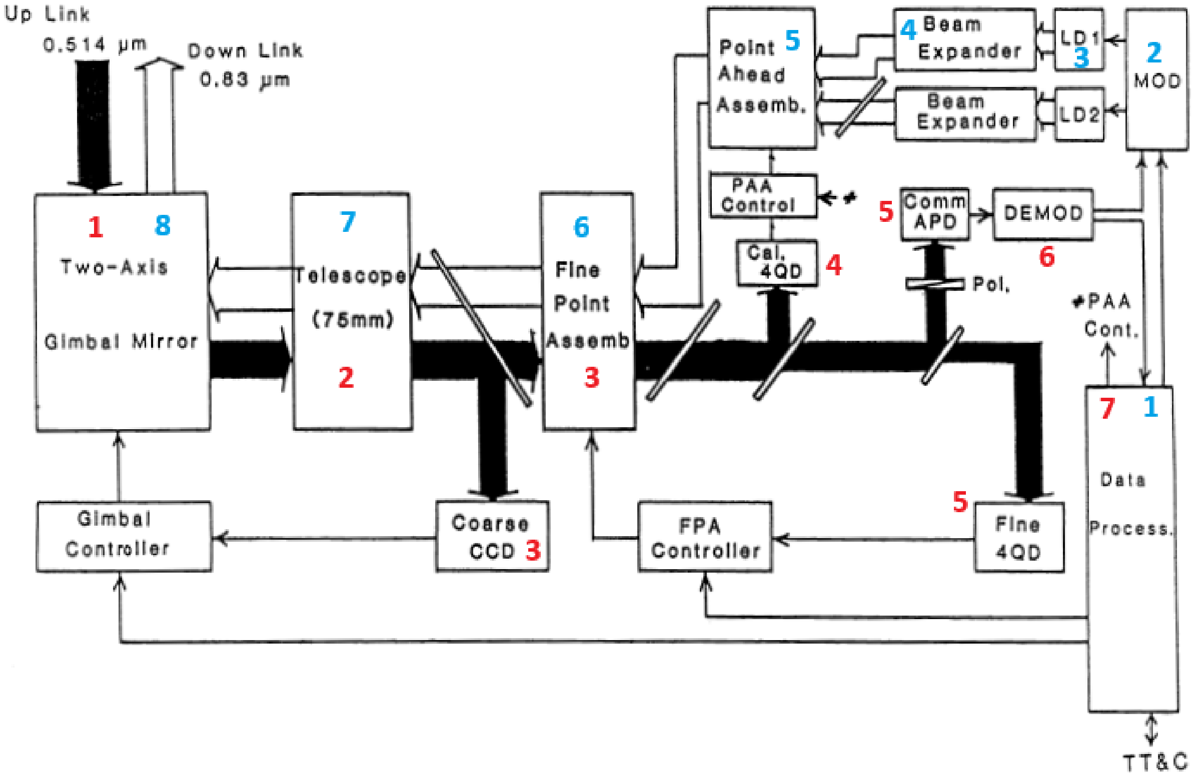

Figure 2.1: ETS-VI LCE system block diagram adapted from [5]

First observing the down link path, indicated by the white arrow and blue numbers: an electrical signal is sent from the data processor to the modulator. In turn, this modulator will cause one of the diode lasers to emit an optical signal. This beam has is then processed in the beam expander, achieving the desired beam width and divergence angle. Next, the beam passes through the Point Ahead Assembly and the Fine Pointing Assembly, both systems which use moving parts and feedback loops to determine and steer the direction of the beam. This direction is determined by the data processor dependant on relative velocities between transmitter and receiver. Finally, the beam is further expanded and sent out by use of a gimbal mirror.

The up link path, shown by the black arrow and red numbers, is somewhat similar, but in a reverse order: the incoming beam is contracted by the telescope and then split and redirected to the coarse Charge Coupled Device (CCD) and the fine Four-Quadrant Diode (4QD) (both optical detector types). These sensors detect the position of the beam and guide the moving parts to steer the beam onto the

Avalanche Photodiode (APD), where the signal is transformed into an electrical one and demodulated.

Most optical communication setups can be divided into three groups according to their function: Signal generation/detection, beam steering and beam manipulation. While this paper will not delve into signal generation (modulation) or beam steering, beam shaping will be integral to the setup to be experimentally verified.

2.3. Challenges in FSOC

The design and operation of FSOC systems is influenced by certain limitations and challenges, some unique to FSOC and some not. While general sources of challenges will be discussed below, this paper will emphasise the research into the influence and mitigation of spacecraft-induced jitter and thus this source will be given its own separate section in section 2.3.2.

2.3.1. General

For most spacecraft design aspects the thermal radiation environment in space is an important factor. This radiation can come from a large number of sources and is highly dependent on time and location. For a spacecraft in orbit around the Earth the main sources are the Sun and the Earth itself. The first issue this radiation can cause is thermal loading and imbalance. Many components in an FSOC system require precise positioning and are susceptible to thermal expansion [31, 32]. This expansion can cause misalignment or even damage components, and could also come from heat transfer of the spacecraft and its systems themselves. Misalignment of components can cause a loss of communication performance, in the form of a decreased signal-to-noise ratio or an increased probability of power outage at the receiver, both of which are important communication characteristics.

A second issue with the radiation environment in space is that this radiation (light from the sun for example) can enter the receiver aperture and thus false positives or over-exposure can become issues in extremely fine-tuned systems [33].

Both of these effects are investigated, however they are not exclusive to FSOC, so they will not be treated here. Similarly for the atmospheric effects, while the atmosphere has both absorptive and scattering/wandering effects on a laser beam [34, 35], its influence on the chosen FSOC system will be outside of the scope of this project.

As with any optical system, FSOC systems come with their inherent issues. Operational errors are unavoidable, can come from a large variety of sources such as limitations on alignment and manufacturing or inherent losses due to material interaction and can have significant effect [36, 37, 38, 39].

2.3.2. Jitter

A large influence on the FSOC system design is vibration of the spacecraft. Due to moving parts, thermal load imbalance, gravitational variation and other factors, a satellite is never truly motionless. This resultant motion consists of both drift, which can be countered by attitude control, and jitter. Jitter consists of stochastic, medium-to-high frequency micro-vibration motions, ranging from 1 Hz to 1 kHz [31]. These are caused by moving components such as momentum wheels or steering mirrors. The multi-layered nature of jitter has been studied by intensive in-orbit measurements, showing that the distribution of vibrational frequencies is highly spacecraft dependent [40, 41, 42].

While these vibrations might seem small, the large distances over which inter-satellite FSOC occurs mean that even a tiny angular error can cause fluctuations in received power or for the beam to miss its target entirely. When using a Gaussian beam, typical for FSOC, figure 2.2 illustrates how any pointing error in physical space causes the centre of the beam to move away from the receiver and decreases the measured intensity from its peak in point 1 to a lower value in point 2.

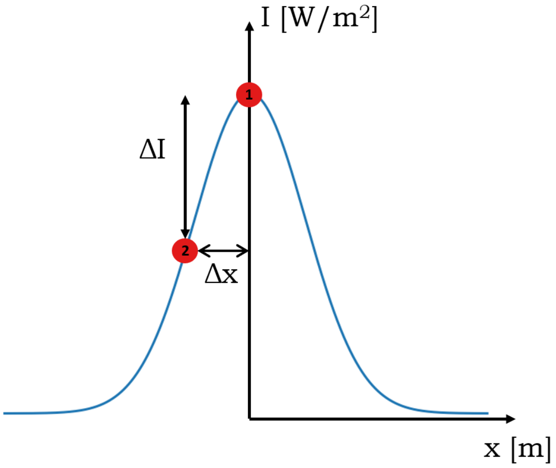

Figure 2.2: Instantaneous pointing error at the receiver (Δx) leading to a lower measured intensity ($\Delta \mathcal{I}$) and thus power.

A lower received intensity and power can reduce the communication performance of the link between transmitter and receiver by causing bit errors or, if a low enough threshold is crossed, complete power outages. These two occurrences are major performance characteristics in any communication system, and are usually expressed as a percentage or probability. In this form, they are known as Bit Error Rate (BER), the percentage of bits being wrongly read as having the opposite value, and Power Outage Probability (POP), the probability of having a BER so high that the countermeasures in place such as bit error correction algorithms start to fail. Much work has been performed in minimising both of these metrics by optimising different aspects of the transmitter or receiver architecture, such as total beam power, beam divergence, receiver aperture, modulation algorithm, etc.[43, 44, 45, 46, 47]

Of special interest to this paper is a theoretical solution presented by Badás et al., where instead of a standard Gaussian laser beam, the intensity profiles of different types of stable beam shape families are investigated [1]. In figure 2.3 it is shown that for an arbitrary intensity profile a pointing error does not necessarily lead to a decrease in received signal power. This can then result in both a decreased BER and POP and thus a more stable connection for the same total beam power. However, this redistribution of power does result in a lower peak intensity and thus has to be taken into account for receiver sensitivity.

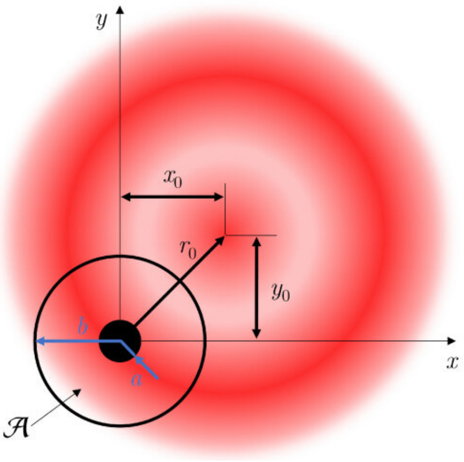

Figure 2.3: "Generic far-field irradiance distribution in the receiver's aperture plane for a de-centred beam. a and b are the inner and outer radius of the aperture and r_0 is the instantaneous pointing error in meters." Image and description taken from [1].

The instantaneous pointing error due to jitter has been shown to follow a Rayleigh distribution, being a combination of independent Probability Density Functions (PDFs) in elevation and azimuthal angles [46]. The intensity profile of the beam within the receiver aperture area can then be combined with these PDFs to achieve a time-independent distribution of the received power [1]. From this distribution the average BER and the POP can be obtained, and iterations can be made to find the optimal intensity profile. This process is illustrated in figure 2.4 where (a) shows the intensity profile in two dimensions and (b) is the power collected as a function of pointing error r_0. (c) shows the PDF of the jitter expressed as a pointing error between the desired and actual centre of the beam. These can then be combined and integrated in (d) into the received power PDF, which below a certain threshold will result in a power outage.

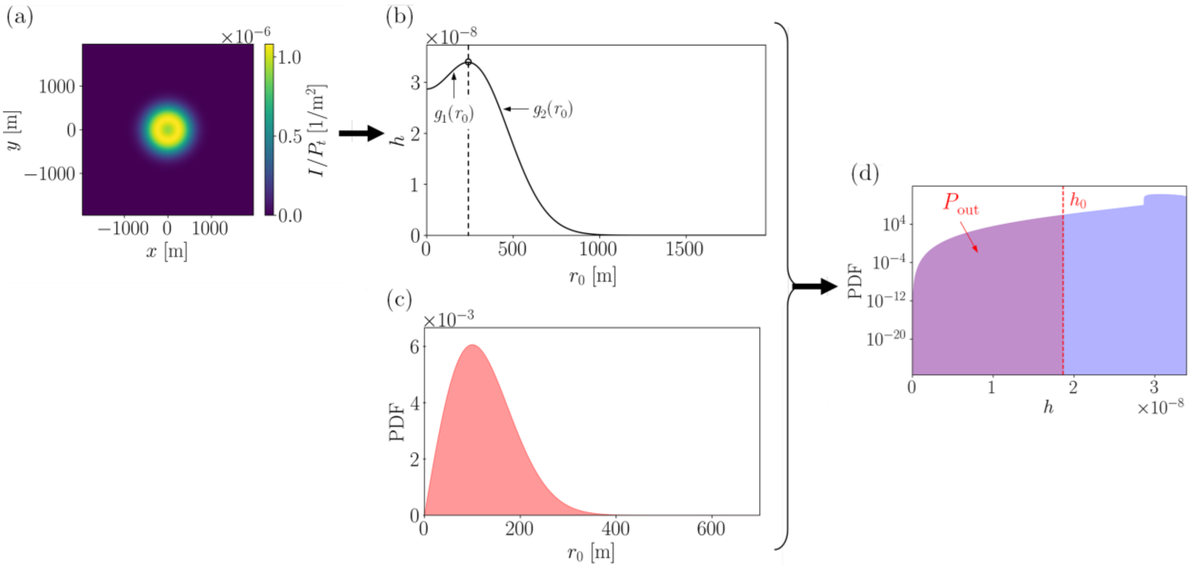

Figure 2.4: General process for obtaining the POP from an intensity profile (a) and the PDF of the pointing error (c), resulting in the received power as a function of pointing error (b) and finally in the PDF of the POP. Figure taken from [1]

While other papers have proposed the use of Bessel or Airy beams [48, 49, 50] for spatial mode multiplexing, mitigation of propagation medium turbulence and other objectives, the paper by Badás et al. proposes the use of a superposition of orthogonally polarised Gaussian and Laguerre-Gaussian beams to mitigate jitter-induced communication errors and further proposes a mock-up setup of how to achieve such a beam, shown in figure 2.5. This proposed setup will be the starting point for creating an experimental setup to validate the results from the theoretical paper.

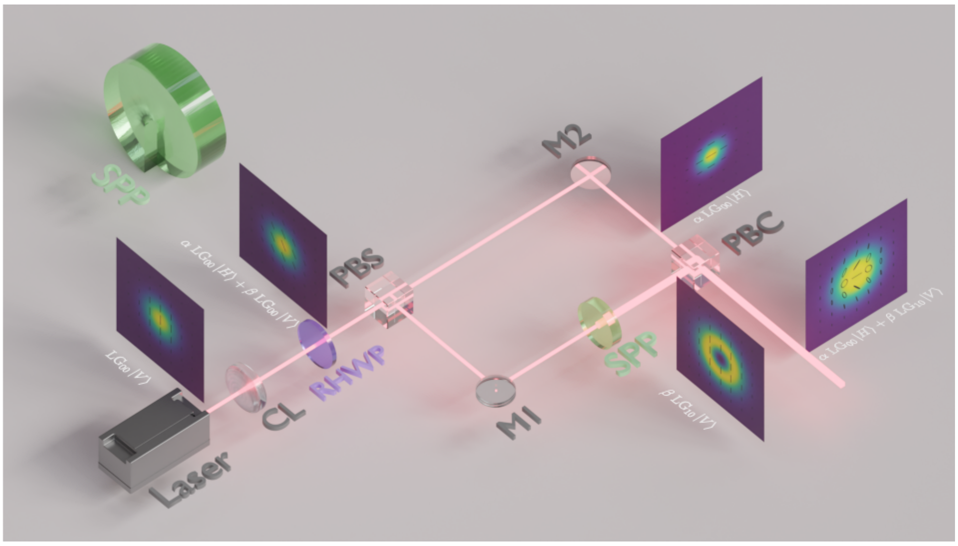

Figure 2.5: Proposed system from [1].

This proposed system starts from a linearly polarised, Gaussian laser source, followed by a rotatable Half-Wave Plate (HWP) to change the polarisation state. The beam is then split into two orthogonally polarised beams by use of a polarising beam splitter. One of these beams then encounters a Spiral Phase Plate (SPP), which is assumed to transform a zeroth order Gaussian beam into a higher order LG beam carrying Orbital Angular Momentum (OAM). From here both beams are then once again brought together using two mirrors and another polarising beam splitter. This superposed beam then travels on to the sensor.

It is important to note that for most of the duration of this project, the assumption was made that an SPP would transform an impinging Gaussian beam into a pure LG one. This assumption was made in the original paper, as well as seemingly in a number of other papers where it was either not stated or omitted [51, 52, 53]. However, this assumption turned out to be wrong, as the beam produced by an SPP is instead an infinite superposition of LG modes [54] which closely resembles the pure LG beam of the same charge as the SPP. The majority of the work in this thesis was performed using said assumption, however a detailed discussion on the obtained beam shape will be given in section 5.3. To distinguish from the LG beam, the beam obtained from the SPP will from here on be called vortex beam.

To ease future representation of how this setup evolves, it can be divided into three functional blocks: beam preparation containing the source and the HWP, beam shaping containing the beam splitters and the SPP, and beam output containing the sensor, shown in figure 2.6.

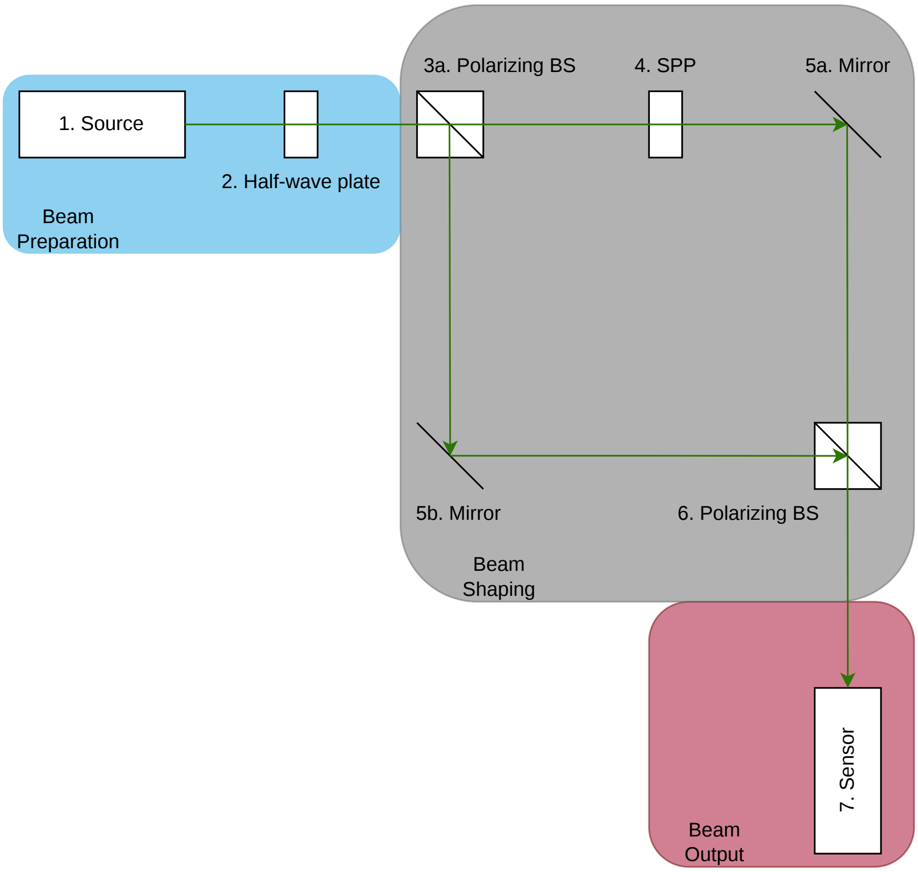

Figure 2.6: Diagram of proposed setup

The core component of this whole system is the SPP, which can impart OAM upon an incoming beam by making use of differential phase retardation. Orthogonal to the beam propagation axis an SPP has a spiral-shaped element which over an angle from 0 to $2\pi/\ell$ increases the phase retardation of the beam passing through. A continuous spiral would result in a local phase retardation of $\Delta\phi = \ell\theta$ with θ being the azimuthal angle, however due to manufacturing limitations on continuous height increase, this is most commonly done by using a spiral staircase increasing the thickness, as shown in figure 2.7 such that the local phase retardation follows equation (2.3).

$$\Delta\phi = \frac{2\pi}{\lambda}(n_{\text{SPP}} - n_0)t \tag{2.3}$$

where t is the local thickness of the steps, dependent on azimuthal angle and the amount of steps per staircase.

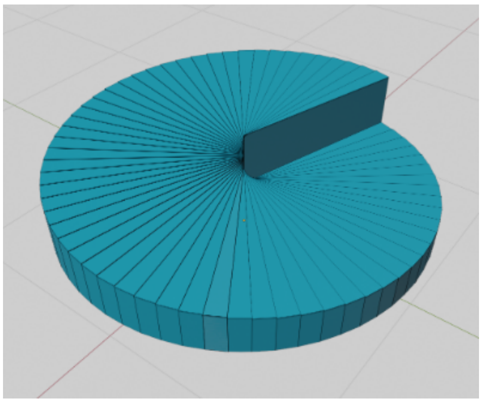

Figure 2.7: SPP of charge $\ell = 1$, image taken from [55].

The total height h of these spiral staircases is determined by the material of the SPP, the operating wavelength and the required charge of the SPP following equation (2.4) and is equal to the number of steps per staircase times the height increase of each step. The charge of an SPP also determines the amount of times this staircase pattern is repeated.

$$h = \frac{\lambda \ell}{n_{\text{SPP}} - n_0} \tag{2.4}$$

Other than SPP's, other options for generating vortex beams include spiral phase mirrors [56], which are reflective versions of SPP's, and spatial light modulators [57], pixelated screens where the individual pixel's optical properties can be adjusted.

The component which will determine the polarisation state of the beam, and thus the fraction of vortex beam to Gaussian beam is the HWP. This is a type of birefringent device that has different indices of refraction between orthogonal polarisation components of light, effectively altering the polarisation state of the beam. For linearly polarised light, the rotation of the polarisation direction is twice the angle between the incoming polarisation direction and the fast axis of the HWP [58].

The second component which deals with polarisation are the polarising beam splitters. Non-polarising beam splitters work by partially reflecting incoming light and partially transmitting it, with the refraction-transmission ratio dependent on the materials used. A polarising beam splitter however reflects or transmits light based on its polarisation state. Depending on the convention, a polarising beam splitter could reflect horizontally polarised light and transmit vertically polarised light or vice versa. In this setup, one is present to split the beam into two and will be called the Polarising Beam Splitter (PBS) and another is present to superpose the beams, to be called the Polarising Beam Combiner (PBC).

One of the main conclusions of the theoretical paper is the power saving potential of using the proposed Laguerre-Gaussian beam combination over standard beams. Depending on the specifics, up to 20 or 40% less power is required to achieve the same BER and POP. This is only when looking at the output however, as the generation of these beams will require extra components not used in traditional systems. These components carry their own transmissive or reflective losses which could counteract these theoretical gains. Thus a major research question to be answered is: ***Do the added components introduce losses that are greater than the predicted gains?***

A major component of the experiment will be beam shaping, which in this case specifically means to transform the intensity profile of an incoming beam into a different profile for the outgoing beam. The next section will therefore present beam shaping methodologies and the theory used.

2.4. Principles of beam shaping

To achieve a beam intensity profile other than the Gaussian beam, which is the fundamental mode of most laser cavities [59], one can make use of a number of methods such as truncating, (partial) reflection, refraction and diffraction [60]. To achieve the desired beam shape, high precision and accurate alignment is required.

Truncating is a beam shaping method where part of the beam is obstructed. Most often this is done by placing an iris or a pinhole in order to only allow the centre of the beam to continue. This can result in an intensity distribution which is nearly uniform over the cross section [61]. Restricting the beam in this way can also lead to a diffraction pattern and the formation of Airy discs [62]. An experimental example of the Airy pattern at the focal point is shown in figure 2.8. Aside from these Airy patterns, clipping also means losing a potentially significant amount of the beam's energy, making it an unattractive method where power is a driver.

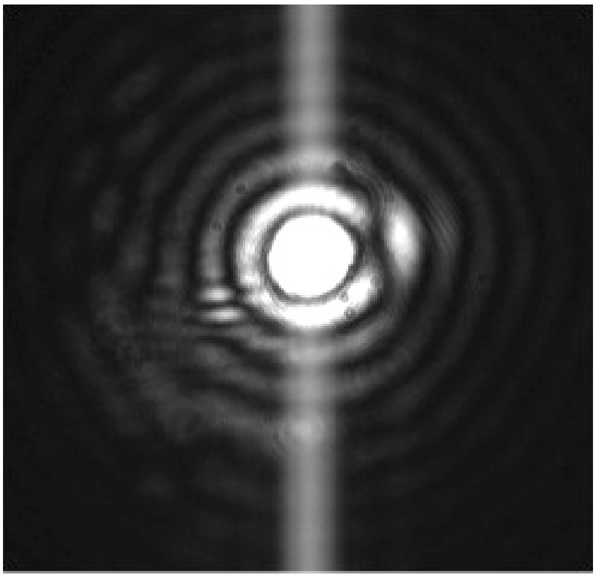

Figure 2.8: Airy diffraction pattern, image taken from [63].

The second beam shaping method is by use of Refractive Optical Elements (ROE). These elements have in common that they make use of Snell's law of refraction, where optical path length a wavefront encounters changes when transitioning from one medium to another. This change in path length is in proportion to the ratio of the refractive indexes of both media. One of the most common ROE is a lens, as shown in figure 2.9. These elements often use varying material thicknesses in order to alter the intensity profile of an incoming beam.

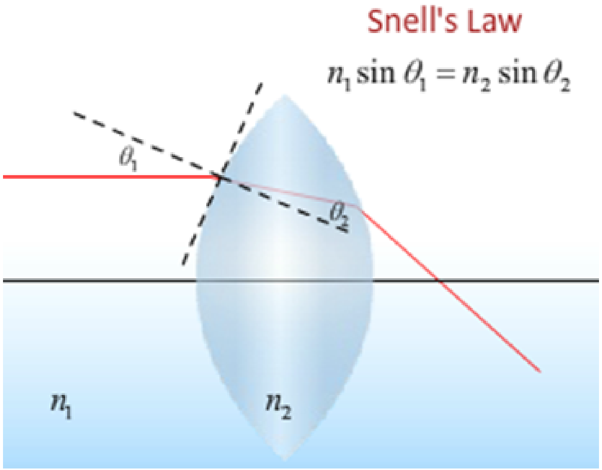

Figure 2.9: Snell's law applied to a lens, image taken from [64].

For beam shaping, some of the most notable ROE are aspheric beam shapers (from Gaussian to top-hat, [60]), axicons (from Gaussian to Bessel beam, [65]), SPP's (from Gaussian to vortex, [55]), spatial light modulators (holograms created by phase-controlled liquid crystals, capable of producing a large number of states, [57]) and bi-refractive elements such as wave plates which carry different refractive indexes dependent on the polarisation state of incoming light. Figure 2.10 shows how light is refracted through an axicon.

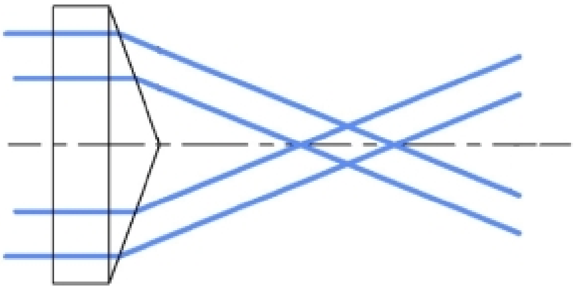

Figure 2.10: Light rays travelling across an axicon, image taken from [65].

The last commonly used method for beam shaping is through the use of Diffractive Optical Elements (DOE). Instead of refraction, these elements use diffraction caused by microscopic structures on the substrate [60]. This means that the use of these elements is highly specific and their optical characteristics are more dependent on operating wavelength and their specific shapes tend to require the incident to be accurately aligned, but in return they offer high spatial efficiency and allow for the creation of complex beam shapes [66]. One downside for FSOC is that they are often not stable propagation modes and will deteriorate when beyond their working distance [67]. DOEs can generally be divided into two categories: beam splitters, which split the beam into a number of smaller 'beamlets' and beam shapers, phase elements transforming the input into uniform spots along a predetermined intensity distribution. Figures 2.11 and 2.12 show result from different diffractive beam splitters and shapers.

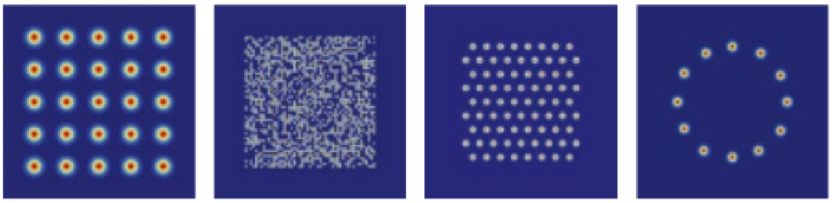

Figure 2.11: Different beam splitter spot distributions, left to right: 5 × 5 array, random, hexagonal array, circle. Image and caption taken from [67].

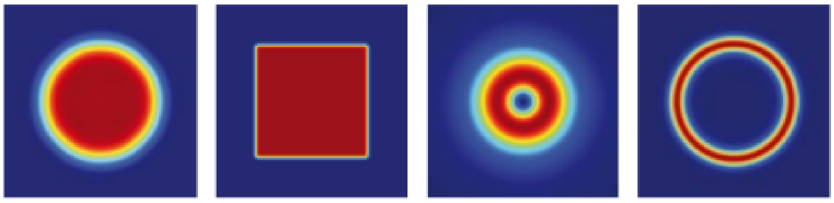

Figure 2.12: Results of different beam shapes, left to right: homogenizer, top-hat, vortex lens, and diffractive axicon. Image and caption taken from [67].

To experimentally verify the setup proposed in [1], proper beam shaping will need to be achieved. An important questions to analyse will be: ***How closely does the output of the experimental setup match to the simulations?*** Alongside this, similar analysis should be performed on the experimentally obtained intensity profile to ask: ***Does the communication performance of the experimental output match the theoretical performance?*** Only then can a determination be made on whether the proposal results in a more robust system with a lower power requirement, even over the added amount of components. If possible, the resulting system can then be expanded to include a jitter simulating section to completely determine the potential benefits of non-Gaussian beam shapes under spacecraft conditions.

To be able to compare the eventual measurements to a simulation however, proper understanding of the theory behind the simulation and propagation of light is a priority. Therefore, the following section will introduce the most pertinent beam shape families and their characteristics.

2.5. Beam Shape Families

For FSOC, it is imperative to have a beam profile which remains consistent regardless of propagation distance, such that the relative shape of the beam does not change. This is required as distance between transmitter and receiver can vary significantly, and precise knowledge of the beam profile at the receiver is needed for proper communication. Physicists have derived stable families of solutions to the paraxial wave equation (2.5), governing all light waves travelling along a dominant axis.

$$\nabla_{\perp}^{2} U - 2jk\frac{\partial U}{\partial z} = 0 \tag{2.5}$$

Where $U(x, y, z)$ is the complex scalar wave amplitude field, and is related to the electrical field as $\vec{E} = U\,\exp(j(kz - \omega t))\vec{n}$ where $\vec{n}$ is the unit vector of the field, k is the wave number $\frac{2\pi}{\lambda}$, z is the main propagation direction and $\nabla_{\perp}$ is the transverse Laplace operator.

As stated, there exist several solutions to this equation, each using different coordinate systems. The following sections will cover a few of the notable families of solutions, giving the derived electric field equation, their intensity distribution, important characteristics/uses and how they are generated. Many of these families carry unique characteristics which make them suitable for the application in multiple fields.

2.5.1. Laguerre-Gaussian Beams

Laguerre-Gaussian beams (LG beams) are part of a beam family that uses the cylindrical coordinates r, θ and z, yielding the solution

$$E_{p,l}(r,\theta,z) = C\frac{w_0}{w(z)}\left(\frac{\sqrt{2}r}{w(z)}\right)^{|\ell|} L_p^{|\ell|}\left(\frac{2r^2}{w^2(z)}\right)\text{exp}\left(-\frac{r^2}{w^2(z)}\right)$$
$$\text{exp}\left(-jkz - j\frac{kr^2}{2R(z)} + j\ell\phi + j(2p+|\ell|+1)\psi(z)\right) \quad (2.6)$$

where:

- C is a normalization constant;
- $L_p^{|\ell|}$ is the generalized Laguerre polynomial;
- w_0 is the beam waist;
- $R(z) = z[1+(\frac{z_R}{z})^2]$ is the radius of curvature with z_R the Rayleigh range $z_R = \frac{\pi\omega_0^2}{\lambda}$;
- ℓ is the azimuthal index or charge and can be any integer;
- p is the radial order and can be any integer ≥ 0.
- $\psi(z)$ is the Gouy phase shift defined as arctan$(\frac{z}{z_R})$

The plots for this equation with varying charges and orders are shown in figure 2.13.

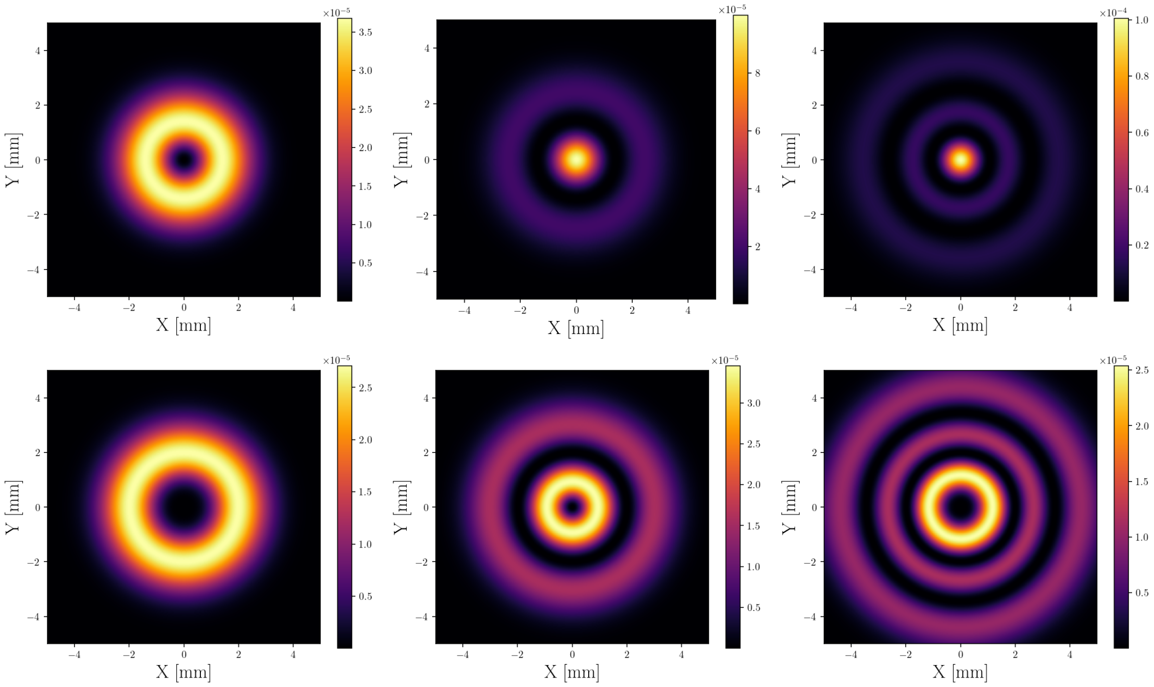

Figure 2.13: Plots of LG beams for varying indexes and orders. Top row from left to right shows $(p,\ell) = (0,1)$, $(p,\ell) = (1,0)$ and $(p,\ell) = (2,0)$, while bottom row shows $(p,\ell) = (0,2)$, $(p,\ell) = (1,1)$ and $(p,\ell) = (2,2)$. Image generated in Python.

LG beams are sometimes denoted as $LG_{p,\ell}$, to specify the order and charge they carry. One of the main characteristics of LG beams is their rotational symmetry and the OAM, which will introduce a torque upon any element placed within the beam path [68]. The main goal when generating a higher order LG beam is imparting OAM onto the incoming beam. SPPs and SLMs accomplish this by spirally increasing the thickness or refractive index, while vortex retarders use a polarisation technique where the fast axis rotates continuously over the area of the element [69]. More detailed information will be given in chapter 4.

Due to their OAM, LG beams are used in optical tweezers as ring traps or utilising their spinning nature [70] or as carriers for optical communication, as the order and index give rise to a new degree of freedom for multiplexing [71],both in classical and quantum communication [72].

2.5.2. Hermite-Gaussian Beams

Hermite-Gaussian Beams (HG beams) are similar to LG beams, however here Cartesian coordinates are used, yielding the solution in equation (2.7) [73].

$$E_{m,n}(x,y,z) = Cw_0 \frac{H_m(\frac{\sqrt{2}x}{w(z)})H_n(\frac{\sqrt{2}y}{w(z)})}{w(z)} \text{exp}\left(-\frac{x^2+y^2}{w(z)^2}\right) \text{exp}\left(-j\left[kz-(1+n+m)\psi(z)+\frac{k(x^2+y^2)}{2R(z)}\right]\right) \quad (2.7)$$

where H_m and H_n are Hermite polynomials with m and n the mode indices representing the number of nodes in horizontal and vertical directions respectively. The other components have been defined in previous sections. Figure 2.14 shows the plots of various HG beams.

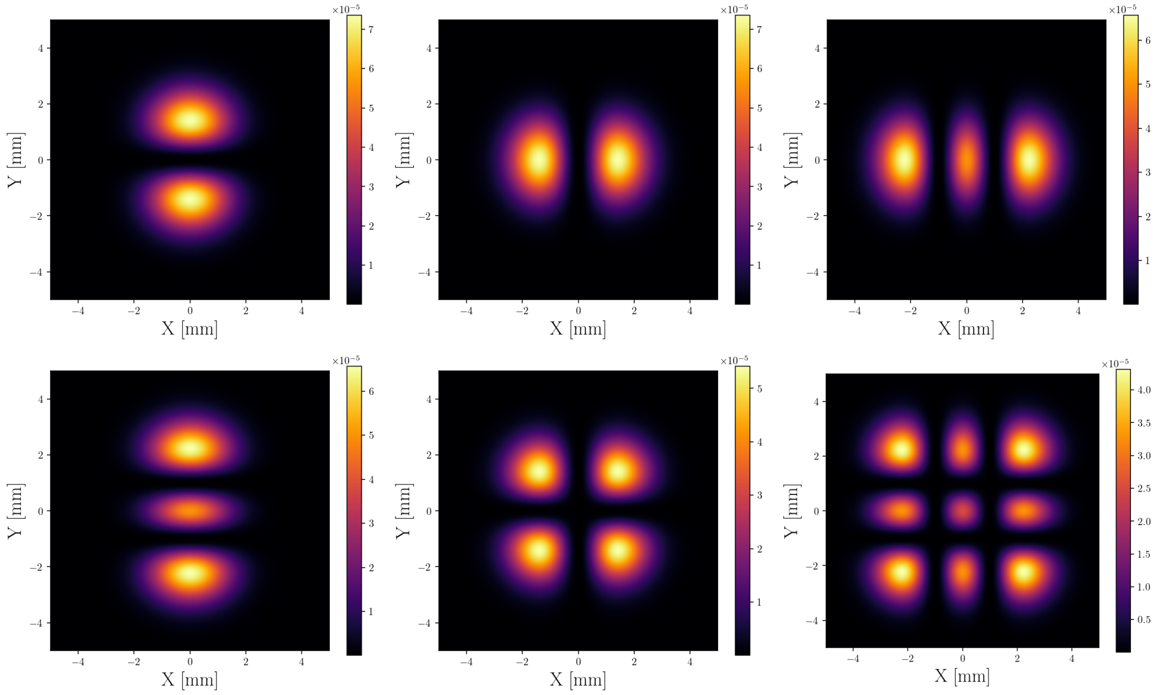

Figure 2.14: Plots of HG beams for varying nodes. Top row from left to right shows $(m,n) = (0,1)$, $(m,n) = (1,0)$ and $(m,n) = (2,0)$, while bottom row shows $(m,n) = (0,2)$, $(m,n) = (1,1)$ and $(m,n) = (2,2)$. Image generated in Python.

HG beams are the fundamental modes in rectangular laser cavities [74], and can relatively easily transformed into other beam shapes such as Ince-Gaussian or LG beams. Furthermore, the multiple peak intensity nodes make HG beams suited for optical trapping at multiple spots [75].

2.5.3. Ince-Gaussian Beams

Ince-Gaussian Beams (IG beams) assume a solution using elliptical coordinates ζ and η. The solution then yields the electrical field shown in equation (2.8) [76].

$$E_{p,m}(\zeta,\eta,\epsilon) = C\frac{w_0}{w(z)}S_p^m(i\zeta,\epsilon)S_p^m(\eta,\epsilon)\,\mathrm{exp}\left(-\frac{r^2}{w^2(z)}\right)\mathrm{exp}\left(j\left(kz+\frac{kr^2}{2R(z)}-(p+1)\psi(z)\right)\right) \quad (2.8)$$

Where the undefined elements are:

- S_p^m is an Ince polynomial of order p and degree m (p and m must have the same parity such that $(-1)^{p-m} = 1$ and obey $0 \leq m \leq p$ for odd Ince polynomials and $1 \leq m \leq p$ for even Ince polynomials);
- $\epsilon = \frac{2f^2}{w_o^2}$, called the elliptical parameter with f the semi-focal separation;
- ζ and η are the radial and angular elliptical coordinates respectively ($\zeta \in [0,\infty)$, $\eta \in [0,2\pi)$), defined as $x = f\cosh(\zeta)\cos(\eta)$, $y = f\sinh(\zeta)\sin(\eta)$;

IG beams are a type of middle point between HG (in Cartesian coordinates) and LG (in cylindrical coordinates) beams. Where the elliptical parameter goes to 0, the IG beam approaches the LG solution, and the HG solution where $\epsilon \to \infty$ [77]. Plots for this equation for varying p and m are shown in figure 2.15.

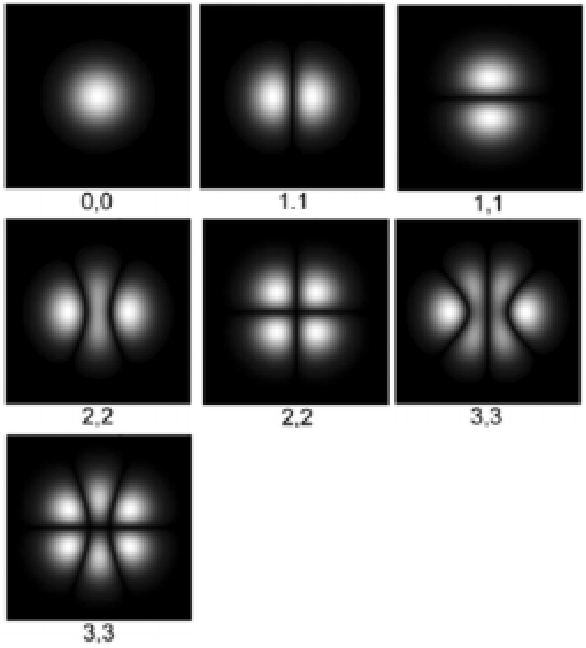

Figure 2.15: Plots of IG beams using different values for p and m,$w_o = 3$ and $\epsilon = 2$. From left to right, the top row shows the plots for $(p,m) = (0,0)$, $(p,m)_{even} = (1,1)$ and $(p,m)_{odd} = (1,1)$. The middle row shows plots for $(p,m)_{even} = (2,2)$, $(p,m)_{odd} = (2,2)$ and $(p,m)_{even} = (3,3)$. The final row shows the plot of $(p,m)_{odd} = (3,3)$. Image adapted from [78].

Interesting to note is that when both p and m are zero, the resulting intensity distribution becomes what is called the Gaussian mode. This is the fundamental solution to the paraxial wave equation which minimizes both divergence and transversal extension [68]. Due to all three discussed beam families using the same solution method, it is a fundamental mode which shows up in all of them.

Its expression in cylindrical coordinates follows

$$E_{\text{Gaussian}}(r,\theta,z) = C\frac{w_0}{w(z)}\,\text{exp}\left(-\frac{r^2}{w^2(z)}\right)\text{exp}\left(-ikz - i\frac{kr^2}{2R(z)} + i\psi(z)\right) \tag{2.9}$$

and its intensity profile is shown below in figure 2.2.

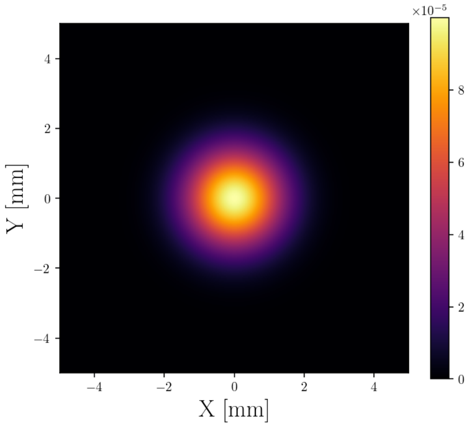

Figure 2.16: Fundamental Gaussian mode

IG beams can be generated by use of holograms [79] or as a fundamental mode of specific resonators [76]. They have found uses in quantum communication, optical communication and storage, medicine and optical trapping [80, 81, 82, 83, 84].

With this information, all is in place to start the experimental process to implement the proposed setup [1]. First a simulation tool will be made to predict the outcomes of the setup and to later verify its output. This verification will be aided by an analysis tool, both of which will be explained in the next chapter. Before this, it can be enlightening to clearly restate the research questions which will be answered during the course of this project:

- **Do the added components required for beam shaping introduce losses that are greater than the predicted gains?**
- **How closely does the beam shape of the output of the experimental setup match to that of the beam propagation simulations?**
- **Does the communication performance of the experimental output match the theoretical performance when subjected to similar calculations as used in the original paper?**

3

Simulation and Analysis Tools

To validate any experimental setup, it first has to be modelled in a simulation. This simulation allows for comparison of the simulated outcome against experimentally obtained values. For this experimental setup, Fourier propagation optics was studied to understand an optical propagation program written by Mr. Aldecocea. This program was then adapted such that it reflects the order and location of components in the experiment. Furthermore, capabilities were added with the goal of eventually performing a sensitivity analysis which could in the future allow for easier problem solving. Finally, a separate program was written to read the experimental and/or simulated data and analyse the obtained results.

3.1. Setup Simulation using General Fourier Optics

At its core, Fourier optics works by expressing the initial electric field perpendicular to the beam's propagation axis and finding its state at any arbitrary z position as a superposition of plane waves [85]. The beam is then propagated and when an optical component (lens, mirror, ...) is encountered, its phase effect on the electric field is added.

In practice, the different states of the electric field is represented by matrices, and the various components the beam will encounter are then represented as phase screens or matrices dependent on component type and specific parameters. For example, a thin lens will introduce a quadratic phase factor shown in equation (3.1) [86].

$$T_{\text{lens}}(x,y) = \exp\left(-j\frac{\pi}{\lambda f}(x^2+y^2)\right) \tag{3.1}$$

The electric field is then sequentially multiplied by these phase screens and allowed to propagate. This propagation is essentially a solution of the Rayleigh-Sommerfeld diffraction integral over some distance z [87], equation (3.2). This integral takes a lot of computational time however and so multiple approximations have been derived from here. Two notable ones are the Fresnel approximation and the Fraunhofer approximation, both of which assume that the propagation distance z in the diffraction integral is very large. The approximated integrals for Fresnel and Fraunhofer are shown in equation (3.3) and equation (3.4) respectively, where $\mathcal{F}$ denotes the Fourier transform [88].

$$E(x,y,z) = \frac{1}{j\lambda}\int\int E_0(x',y')\frac{z}{r}\frac{\exp(jkr)}{r}dx'dy' \tag{3.2}$$

$$E_{\text{Fresnel}}(x,y,z) \approx \frac{\exp\left(jk(z+(\frac{x^2+y^2}{2z}))\right)}{j\lambda z}\mathcal{F}\left\{E_0(x',y')\exp\left(\frac{jk(x'^2+y'^2)}{2z}\right)\right\}(\frac{x}{\lambda z},\frac{y}{\lambda z}) \tag{3.3}$$

$$E_{\text{Fraunhofer}}(x,y,z) \approx \frac{\exp\left(jk(z+(\frac{x^2+y^2}{2z}))\right)}{j\lambda z}\mathcal{F}\left\{E_0(x',y')\right\}(\frac{x}{\lambda z},\frac{y}{\lambda z}) \tag{3.4}$$

here E_0 represents the electric field in the input at $z=0$.

Another method of propagating light is done by the angular spectrum method, where the electric field is decomposed into plane waves [89]. All mentioned methods use Fourier transforms in their implementation and are thus part of what is commonly called Fourier optics.

An additional strength of Fourier optics is that aberrations in components can also be represented as phase screens, which would take the form shown in equation (3.5). This allows for implementation of a sensitivity analysis on component placement and alignment.

$$T_{\text{aber}}(x,y) = \exp\left(\phi_{\text{aber}}(x,y)\right) \tag{3.5}$$

For this project the phase screen of an SPP is especially important. This component will be explained in more depth in chapter 4, but for the simulation it is important to know that the physical component consists of a transparent plate with stepwise spiral staircases on top (figure 2.7). The amount of staircases is dependent on the charge of the SPP, but each one consists of a number of steps and has a total step height dependent on the wavelength and the material used.

This component is simulated by the propagation program by calculating the local phase delay caused by light travelling through a different medium, with a local variation in height representing the steps, shown in equation (3.6). The outgoing electric field is then calculated using equation (3.7).

$$\Delta\phi = \frac{2\pi}{\lambda}(n-n_0)t_{\text{local}} \tag{3.6}$$

$$E_{\text{out}} = E_{\text{in}}\exp\left(j\Delta\phi\right) \tag{3.7}$$

here n is the refractive index of the SPP material and t_{local} is the local height of the steps which is dependent on the azimuthal angle and charge of the SPP. The phase screen of an $\ell = 2$ SPP can then be shown to look like

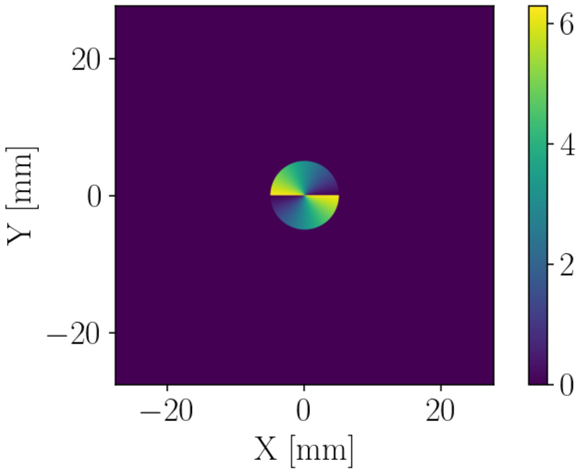

Figure 3.1: Phase screen of an SPP of charge 2

3.2. Polarisation in Fourier Optics

The proposed experimental setup makes use of orthogonally polarised beams to accomplish its beam shaping and superposition without inducing interference. In order to introduce polarisation states and polarising components to the Fourier method, Jones calculus must be considered. In Jones calculus, the electric field is represented as a vector state of fields depending on their polarisation state, shown in equation (3.8) [90].

$$\mathbf{E}(\mathbf{x},\mathbf{y}) = \begin{bmatrix} E_x(x,y) \\ E_y(x,y) \end{bmatrix} \tag{3.8}$$

This vector will have complex components for elliptically or circularly polarised light, and only real components for linear polarised light.

Similar to refractive components, polarising components will multiply the field by a transformation function, the Jones matrix [91]. For example, an HWP aligned with the horizontal direction as the fast axis has as its Jones matrix

$$\boldsymbol{J}_{\textbf{HWP}} = j \begin{bmatrix} 1 & 0 \\ 0 & -1 \end{bmatrix} \tag{3.9}$$

.

3.3. Functional Flow of the Simulation Tool

From the theory in both the chapter and the section above, an optical propagation program was written by the author of the preceding paper, Mr. Badás [1]. Parts of this program were altered and expanded upon in order to have it represent the setup to be built in the lab. The final version of the program operated following the steps shown in figure 3.2.

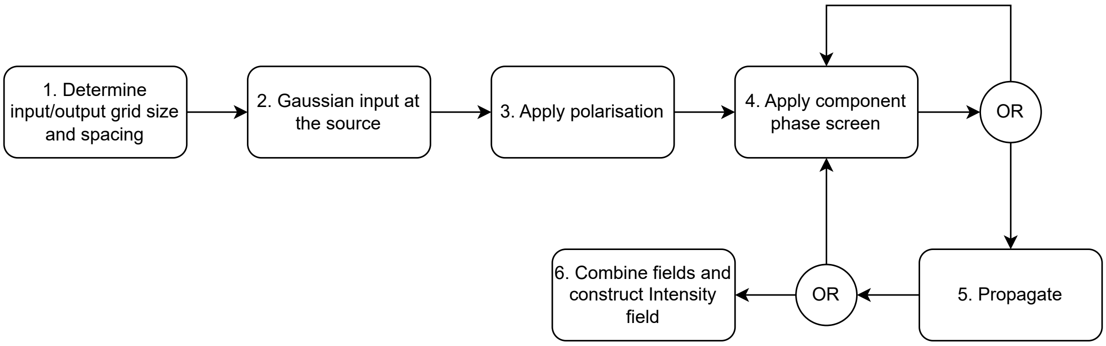

Figure 3.2: Flow diagram of the simulation tool

In step 1 the grid size and spacing for both the in- and output are determined according to four conditions which must be fulfilled when using Fresnel propagation [92]. These conditions arise from propagation geometry and restrictions on facets such as sampling.

$$\delta_2 \leq -\frac{D_2}{D_1}\delta_1 + \frac{\lambda \Delta z}{D_1} \tag{3.10}$$

$$N = \frac{D_{\text{grid}}}{\delta_2} \geq \frac{D_1}{2\delta_1} + \frac{D_2}{2\delta_2} + \frac{\lambda \Delta z}{2\delta_1 \delta_2} \tag{3.11}$$

$$N \geq \frac{D_1 \lambda \Delta z}{\delta_1(\lambda \Delta z - D_2 \delta_1)} \tag{3.12}$$

$$\Delta z \geq \frac{D_1 \delta_1 R}{\lambda R - D_1 \delta_1} \tag{3.13}$$

where subscripts 1 and 2 refer to the input and output grid respectively, δ is the grid spacing, N is the sampling amount, D is the grid size, Δz is the propagation distance and R is the radius of curvature.

From these conditions the grid spacing (or pixel size) for both the input plane and the output plane, as well as sampling amount are determined. This information is then used to construct all the grids which will be required. These grids take the form of a three dimensional matrix $(2 \times N \times N)$, such as

$$\boldsymbol{A} = \left[\boldsymbol{A}_{||}, \boldsymbol{A}_{\perp}\right] \tag{3.14}$$

where $\boldsymbol{A}_{||}$ and $\boldsymbol{A}_{\perp}$ are both matrices of dimension $(N \times N)$ representing the two orthogonal polarisation states.

One of these grids is the input, where a Gaussian beam is then constructed following equation (2.6) setting both p and ℓ to 0. This Gaussian beam is then rotated by a Jones Matrix in order to obtain the desired polarisation state at the input. Following this, a cycle of applying component phase screens and propagating the beam takes place until the setup has been followed through.

Finally, the polarisation fields are vectorially summed and the resulting modulus is squared, resulting in the intensity field. This intensity field is then plotted and saved for later use in the analysis program.

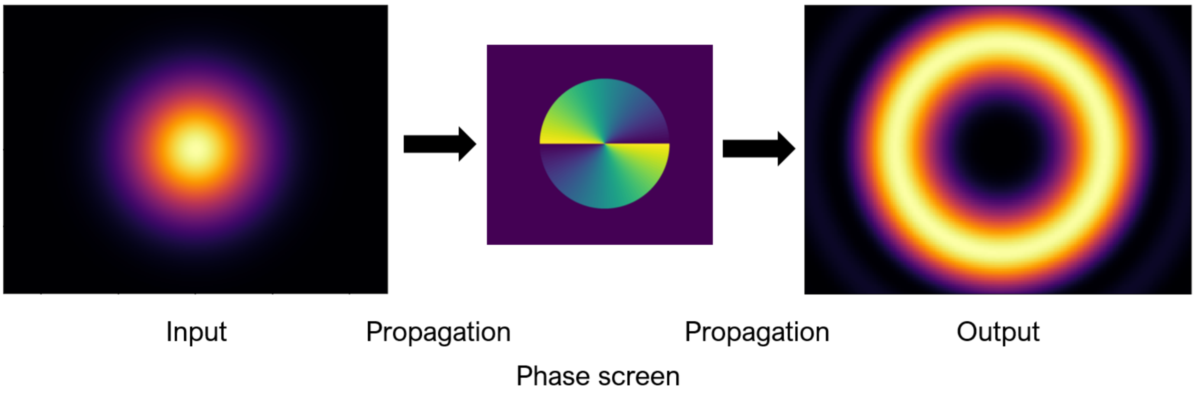

Figure 3.3: Simplified simulation process from in- to output

3.4. Sensitivity Analysis

In general, the sensitivity analysis of an optical system will include its response to two types of misalignment: displacement and rotation. Displacement is the non-optimal placement of a component in (x, y) coordinates, such that the component's principal axis does not coincide with the beam's desired propagation axis, which is the z axis. Components can also be misaligned in tip or tilt angle (rarely in roll, as most components are functionally radially symmetrical). Some components might not change their output under these conditions (such as neutral densities), but most refractive components will produce a worse result [93]. Another potentially important effect that misalignment can cause or worsen is scattered light reflected by a component, which in complicated optical systems can cause cross-talk between components. However, this aspect will not be investigated in this paper.

In order to characterise the system's response, three main changes can be made: The grid can be displaced to simulate a component being at the wrong (x, y) position, the propagation distance can be altered to simulate a component being at the wrong z coordinate and a phase error screen $T_{error} = \exp(jk(\theta_x x + \theta_y y))$ can be added to simulate tilt or yaw errors [94]. For this last point, it is important to also include an (x, y, z) displacement to the grid, since rarely does rotational misalignment occur along the primary axes of the component due to the mount. This functionality was mainly used to simulate errors in aligning the SPP.

These techniques make it possible to determine the most sensitive component and to later cross-reference the results in order to further refine the experimental setup. Figure 3.4 shows an example of applying displacement and rotation on the SPP.

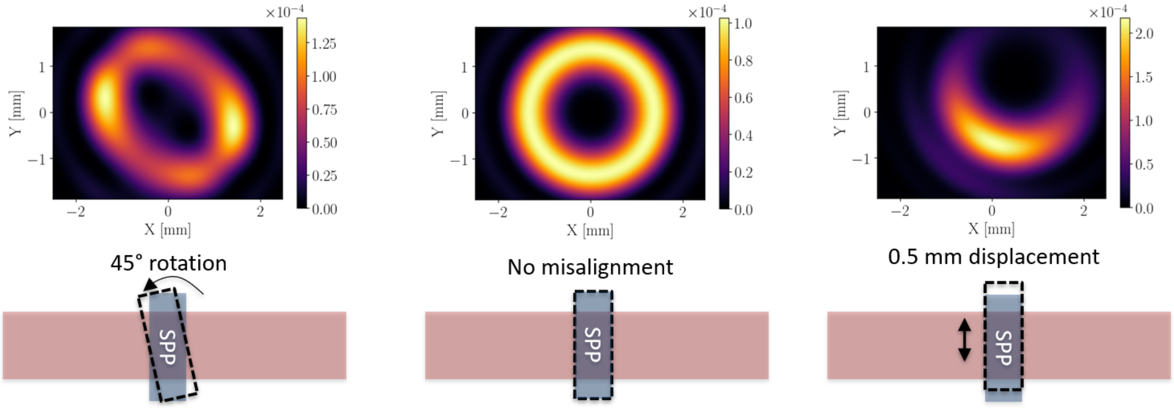

Figure 3.4: Simulated rotation and displacement of the SPP

From this image, it can be seen that in order to properly distort the beam, large amounts of angular misalignment need to take place, while only small amounts of linear misalignments already have a large impact on the vortex beam profile. These findings will be compared to the experimental results and verified in chapter 5.

3.5. Measurement Analysis Tool

The main use of the measurement analysis tool is to read and compare one set of data to another such as experimental data to simulated data or simulated data to pure LG beams, as well as estimate certain beam characteristics.

All measurements and simulations were stored as .tif files, with a consistent naming and storage location scheme. This allows the program to easily find, read and store the data as a large array. Alongside this array, the name of the file also helps assign information such as dataset and the value of the specific variable said dataset aimed to investigate (orientation of the HWP for example).

After a measurement is loaded, it is first normalised such that its integral is equal to one (given that the data is of intensity fields, the contained power will be one). Then, depending on the comparison to be made, a second data point is loaded or an vortex beam profile is generated.

The generation of this vortex beam is done in two ways, depending on HWP orientation: When the expected location of the peak intensity lies at the centre of the beam, a *curvefit* [95] operation is called to return the centre coordinates and beam waist which produce the best match with the function for the combined intensity of a Gaussian beam and a LG beam using equation (3.15).

$$I_{\text{total}} = \eta_{\text{SPP}} \cos^2(2\theta_{\text{HWP}}) I_{\text{vortex}} + \sin^2(2\theta_{\text{HWP}}) I_{\text{G}} \tag{3.15}$$

where I_{vortex} and I_{G} are given by equations (3.16) and (3.17), which are simplified and normalised versions of the general equation (equation (2.6)) for LG beams with $p = 0$ (and $\ell = 0$ for the Gaussian beam), θ_{HWP} is the orientation of the HWP and η_{SPP} is the transmission efficiency of the SPP.

$$I_{\text{vortex}} = C_{\ell p}^{\text{LG}} \left(\frac{\sqrt{2}r}{w}\right)^{2|\ell|} \exp\left(\frac{-2r^2}{w^2}\right) \tag{3.16}$$

$$I_{\text{G}} = C_{\ell p}^{\text{G}} \exp\left(\frac{-2r^2}{w^2}\right) \tag{3.17}$$

This method works best for measurements and simulations where the Gaussian beam is dominant, such that the maximum intensity peak lies at the centre of the beam. Where the vortex path dominates however, imperfections in the setup and an undeveloped beam (to be explained in Chapter 5, but demonstrated in figure 3.6) can cause the *curvefit* algorithm to return a beam waist which does not match with reality. To reduce this issue for HWP orientations beneath a certain threshold a new function was used which matched the location of the maxima of the data with the maxima of equation (3.15), found by differentiation. The results are shown below.

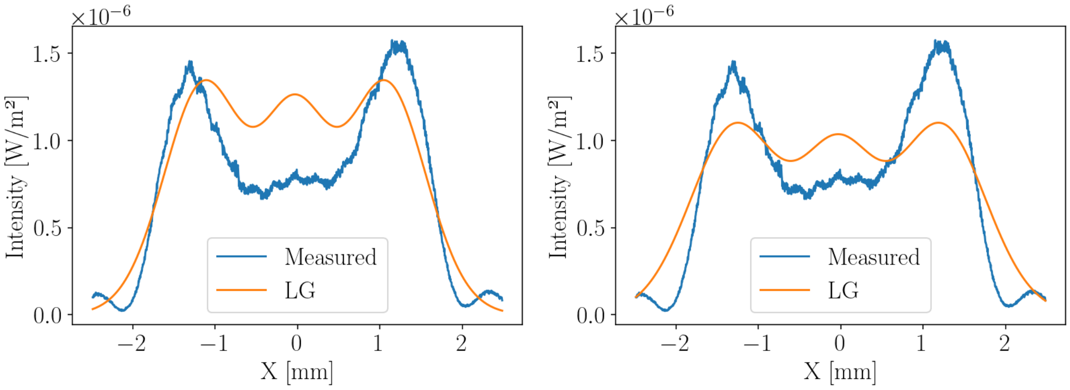

(a) Horizontal slice showing measured data compared to an LG beam using the *curvefit* function.

(b) Horizontal slice showing measured data compared to an LG beam obtained by matching the maxima.

Figure 3.5: Horizontal slices showing the effect of matching the peaks of a normalised LG beam to the obtained data, for an HWP angle of $13.5°$.

To remove the influence of irregularities in the setup which would cause local peaks to be shifted, this operation was done on one-dimensional slices of the intensity profile, rotated around a previously determined central point. The average of these beam waists was then used as the true waist, and the deviation can be used to show potential ellipticity or other errors present in the beam.

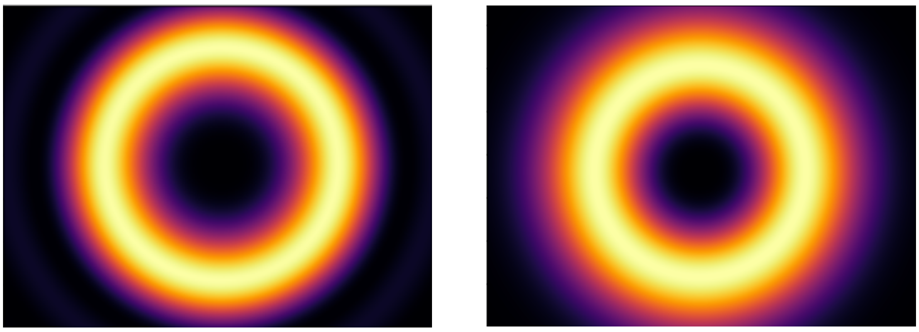

(a) Vortex beam simulated with $z \approx 4m$

(b) LG beam with $z = \infty$

Figure 3.6: Intensity profiles showing the simulated beam on the left and an LG beam on the right

When the relevant data has been loaded and the vortex beam has been estimated and generated, the program then calculates the coefficient-of-determination, R^2, by use of equation (3.18).

$$R^2 = 1 - \frac{\int (I_1 - I_2)^2 dA}{\int I_1^2 dA} \tag{3.18}$$

where subscript 1 detonates the baseline data and subscript 2 the data to be compared to said baseline, dA refers to the area covered by each individual ”segment” of the profile, in this case a single pixel.

This equation was once again used on each slice of the data to be analysed, resulting in a list of R^2 values corresponding to angular orientation. For these values a 0 represents a dataset being compared to an empty field and 1 means a perfect match. Finally, the program plots the relevant intensity profiles and returns the average R^2, beam waist and centre coordinates.

4

Setup and experimental process

Parallel with the simulation and analysis programs, the physical setup was constructed in the lab. This was a process which occurred in multiple phases and required knowledge on the available components, how they function and interact with one another, what physical limitations mean for the system and how proper alignment is done. At first, a rough simulation program was constructed to obtain first order estimations of the optical power and intensity distribution throughout the system proposed in the precursor paper, giving an estimate of what will be required of the various components. Then a list of required components was compared to those already available to determine which components were missing and what operating variables such as beam size, wavelength, source power, etc. would be best for the project to come.

4.1. Initial radiometric budget

To start implementing the proposed setup, a number of components would have to be acquired. Determining which components were appropriate was done by the use of a radiometric budget estimation program. This program was created with the goal to determine what the intensity profile and beam power would look like at various positions in the setup given a combination of component transmissivity/reflectivity, source power and sensor pixel sensitivity.

The angular position of the HWP's fast axis with respect to the horizontal plane could be adjusted to effectively give a ratio of the beams transmitted and reflected by the PBS. Finally, the sensing area, pixel size, full-well capacity and quantum efficiency of a sensor can be used to determine whether the individual pixels could detect the local intensity.

The program thus compared a number of Gaussian and LG beam combinations of various charges so that a suitable combination of components and polarization states could be determined. Figure 4.1 and figure 4.2 show an example of the plots generated by the program, while table 4.1 shows the numerical results printed for a combined $LG_{0,0}$ and $LG_{0,2}$ beam where 75% of the beam power is directed towards the $LG_{0,2}$ beam path. In a lossless system, the intensity profile would be given by equation (4.1), where I_{LG} and I_{G} are given by equation (2.6) with $p = 0$ for both, $\ell = 0$ for the Gaussian path and the charge of the SPP for the vortex path.

$$I_{\text{Total}} = \cos^2(2\theta_{\text{hwp}})I_{\text{LG}} + \sin^2(2\theta_{\text{HWP}})I_{\text{G}} \tag{4.1}$$

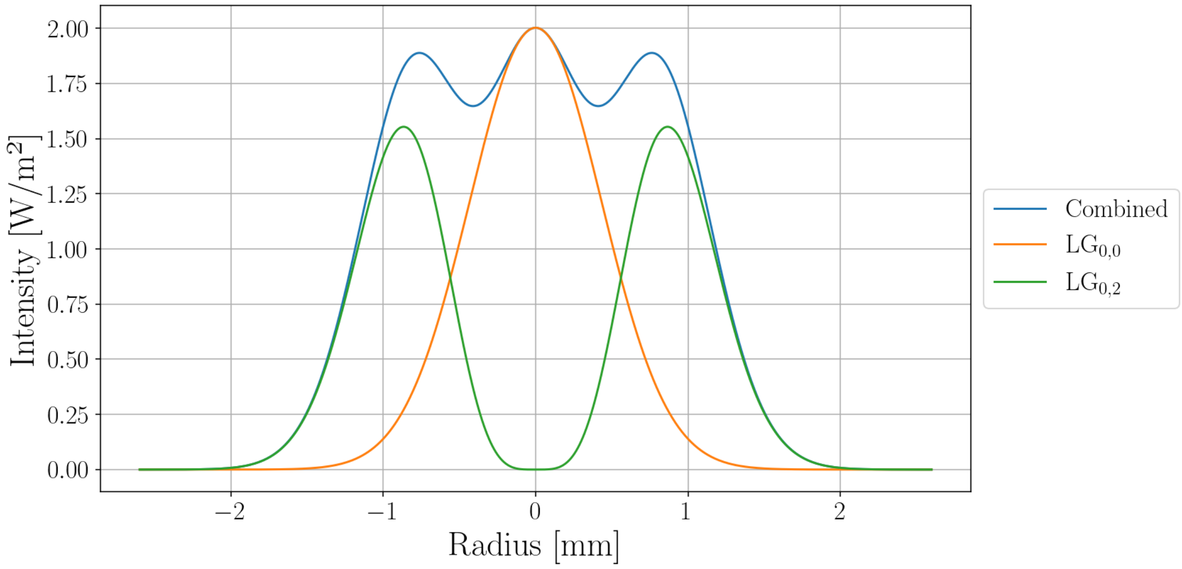

Figure 4.1: Intensity graph of a combined $LG_{0,0}$ and $LG_{0,2}$ beam.

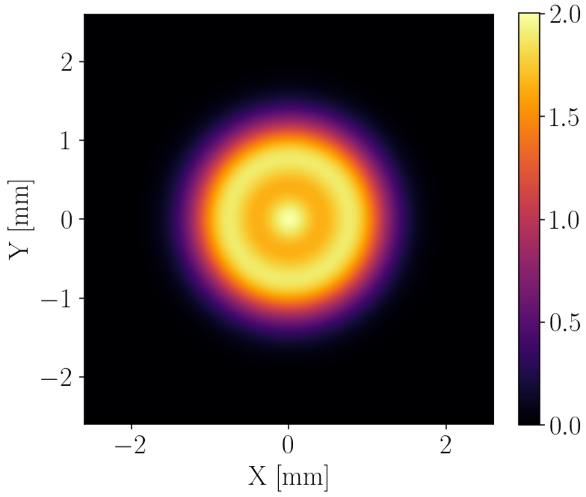

Figure 4.2: 2D Intensity profile of a combined $LG_{0,0}$ and $LG_{0,2}$ beam.

Calculated component	Value
I_{max}	$1.62W/m^2$
$I_{r=1.5mm}$	$0.06W/m^2$
$e^-_{generated}$	1431
$I_{max,allow}$	$12.45W/m^2$
$I_{min,allow}$	$0.023W/m^2$

Table 4.1: Numerical results for a combined $LG_{0,0}$ and $LG_{0,2}$ beam.

This table shows the calculated maximum intensity, the intensity at a distance such that 90% of the beam power lies within said distance, the maximum allowable intensity and the minimum allowable intensity for the sensor.

4.2. Component selection

Looking at affordable suggested components (Edmund optics for source, Vortex Photonics for SPP and Thorlabs for sensor and other standard components), important values such as transmissivity or reflectivity, power ranges, sensitivity and size could be entered to verify if they would work together under different linear polarisation states. This started an iterative process to choose a laser of a desired wavelength and power, an SPP of a sufficient charge and a sensor which could accurately report on the beam profile.

Quickly, a few conclusions became apparent:

- **SPP:** The list of vendors for vortex beam generators was very limited, especially since it had to be a non-polarisation-dependent component. The provider Vortex Photonics was selected, offering SPPs for 1" and 2" optics [96]. Given that most of the already available equipment in the lab were 1" optics, that was the size chosen moving forward. The next parameter to be chosen was the charge. In the original paper [1], charges 1, 2, 3 and 4 were considered, where $\ell = 2$ or 3 came out as the best candidates. The charge and polarisation state would also determine the visibility of the peaks (higher charge means distant peaks but less intensity) and so charge 2 was chosen. Later on in the project an SPP of charge 1 was also obtained, also allowing the superposition of SPP's to create an $\ell = 3$ vortex beam
- **Sensor:** From the limited list of affordable cameras on Thorlabs, their 1.6 MP monochrome camera (CS165MU/M) was considered the best option [97]. It had suitable sensitivity and pixel size and was to set up and use. Furthermore, any component not further specified, such as a PBS, lenses and various mounts that had to be ordered were chosen from Thorlabs' catalogue, since Thorlabs components were by far the most abundant in the lab, ensuring future compatibility.
- **Source:** Given that the sensor chosen had a peak quantum efficiency at around 500-600 nm wavelengths, a 532nm (green) laser was chosen. The visible light would also make rough alignment and problem solving easier. From the available options, a 1mW diode laser produced by Edmund Optics was chosen [98]. This was the lowest powered laser in its section, but the radiometric budget quickly showed that the intensity would be on the order of 2 magnitudes too strong for the sensor, thus an Optical Density (OD) filter would be a must.

From further discussions, some changes to the setup were proposed. First, as stated above, an OD filter (a neutral density filter to be specific) had to be used to avoid saturation or even damage to the sensor. Second, the beam width and divergence of the laser would make the beam far too large for the sensor area and thus two lenses would be required to construct a beam contractor. Third, the supervising professor suggested using a pair of mirrors as an adjustable ”periscope”, since the laser did not come with a multi-axis rotatable mount, thus allowing for fine steering of the beam.

After this phase, a list of materials was made and is shown in table 4.2, where the mounts include the necessary post and holder when not mentioned.

Component	Accessories	component reference	Amount
Source	cable,mount	[98]	1
Mirror	tip tilt mount, rotating post holder	[99]	4
100mm Lens	mount	[100]	1
50mm Lens	mount, post slider	[101]	1
ND Filter	mount	[102]	1
HWP	rotatable mount	[58]	1
PBS	mount	[103]	2
SPP	5-axis kinematic mount	[96]	1
Sensor	mount	[97]	1

Table 4.2: Simplified BOM of first setup

4.3. First setup version

The alterations to the proposed system and selections in components resulted in the revised setup seen in figure 4.3 and figure 4.4 to be built and tested. Components have to be placed in mounts before they can be attached to an optical bench. These mounts can be much larger than the components themselves and have protruding elements such as adjustment knobs for fine alignment. Thus ample space was left between the components where possible, also indicated in the diagrams.

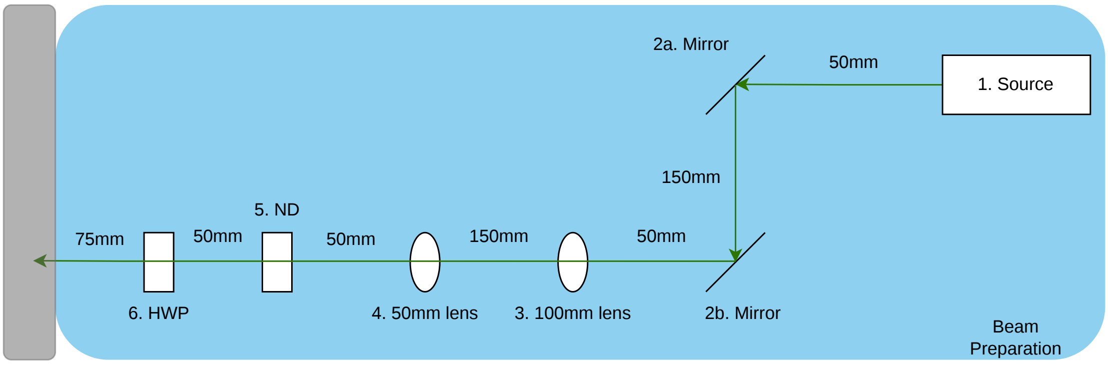

Figure 4.3: Diagram of first setup beam preparation section

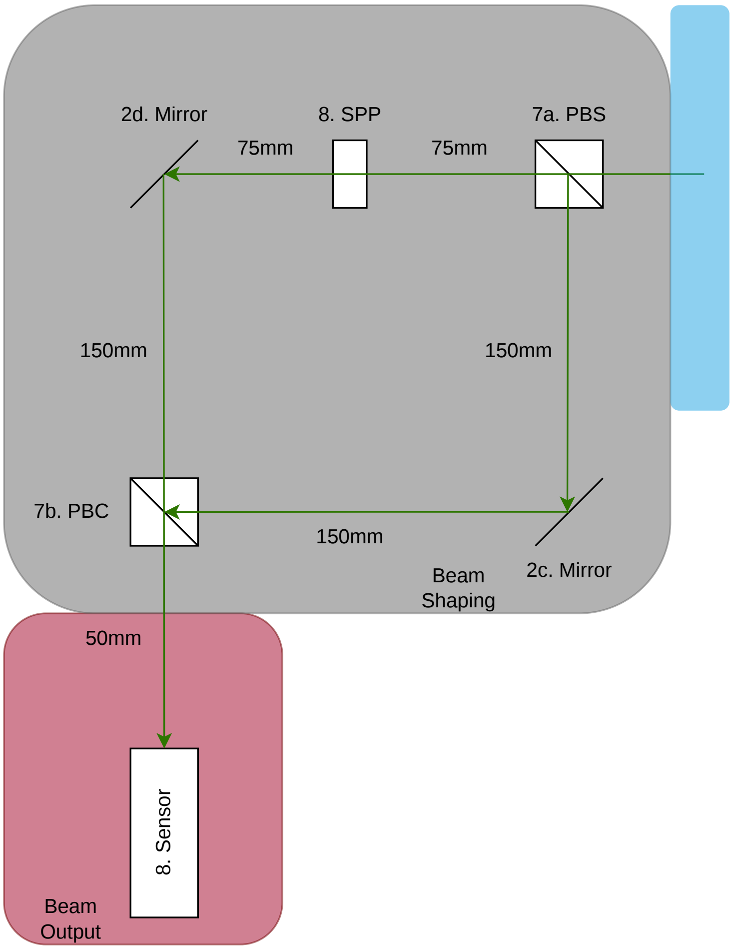

Figure 4.4: Diagram of first setup beam shaping and output section

While the core components of the proposed system remain present in this version, the discussed periscope mirrors, beam contraction lenses and neutral density filter are all added before the HWP.

Before the construction of this setup, it was expected that the main difficulties would come from the aiming of the beam and the proper alignment of the lenses. Most issues with the aiming were solved with the two periscope mirrors, but in order to properly re-collimate the beam, utmost precision in placing the lenses would be required. A single lens already requires precise placement, as the incoming beam has to be aimed exactly in the centre and impinge the lens head on. The second lens would then require the same, in addition to being placed exactly at the distance that is the sum of their focal lengths from the initial lens. For these reasons it was decided that the lenses would be the driving components when aligning the system and determining the operating height.

During the setup process many practical lessons were learnt, such as how to mount components in a way that minimizes tip tilt, how to use back-reflected light to more closely align lenses, how to use frosted alignment discs and many more. At the end of the alignment process, figure 4.5a and figure 4.5b were taken, representing the vortex beam path without and with the SPP respectively.

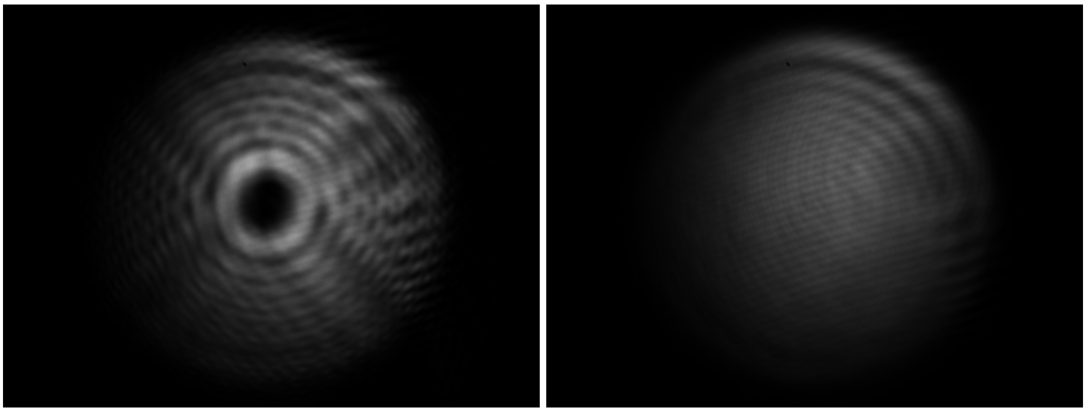

(a) Image of the vortex beam path without the SPP **(b)** Image of the vortex beam path with the SPP

Figure 4.5: Images of the vortex beam path with and without SPP

At this point the analysis tool was updated to calculate the R^2 fit (equation (3.18)) against the equation for a Gaussian and LG beam for the beam path without and with SPP respectively, shown in figure 4.6 and figure 4.7.

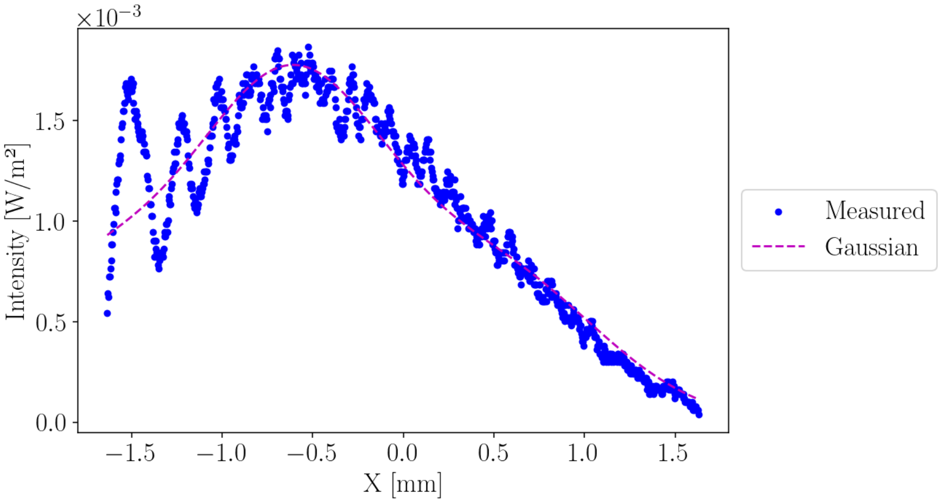

Figure 4.6: R^2 fit of the Gaussian beam path

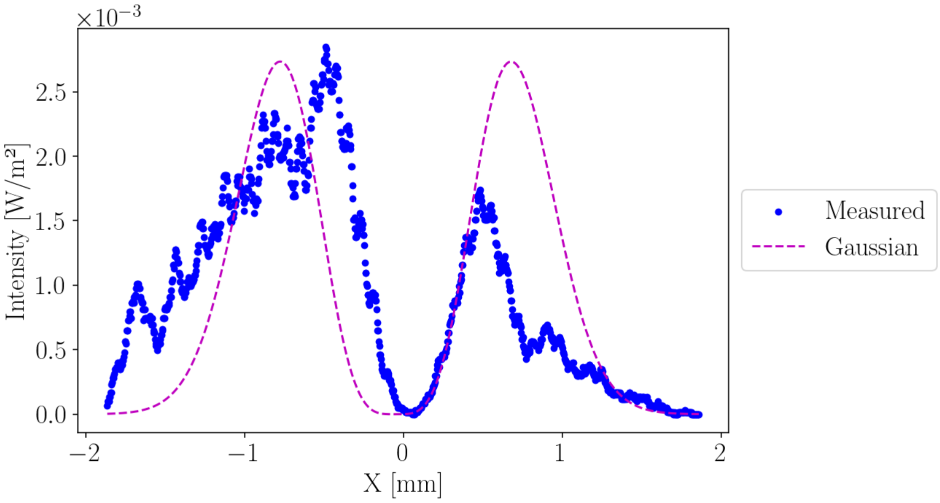

Figure 4.7: R^2 fit of the vortex beam path

From the images and the fit plots, a few conclusions can be drawn. Regarding the Gaussian beam path, the averaged intensity follows a close approximation of a Gaussian curve, but a ripple pattern is present, as well as a peak intensity shift to one specific side. This peak shift was due to a misalignment in the system, potentially at the beam contractor lenses. The ripple pattern seems to be a more fundamental problem however, as SPPs require accurate Gaussian input to be able to output a proper vortex beam [104]. Stepwise removal of components shows that the origin of this pattern lies at the laser source, and the pattern strongly invokes an issue regarding diffraction, spherical aberration or the overlapping of multiple fundamental modes.As can be seen from the vortex beam image and plot, this non-Gaussian nature of the beam profile negatively affects the output of the SPP and thus removing this issue will be at the core of the first major iteration upon the design in section 4.5.

4.4. PBS characterisation

During the period between iterations, characterisation tests on the PBS could already be done. To decide the placement of the SPP and to characterise the polarisation state of both beam arms, linear polarisers (LPs) and beam blockers were used at various positions and orientations, in combination with a simple power meter. As for the alignment convention, it was decided that the direction of the LP which blocked the least amount of power from the beam before the HWP, corresponding to the source's fast axis, would be called the horizontal direction, while the direction orthogonal to this would be called the vertical direction. First, the total beam power before and after LP1 was measured for orientations of the HWP at 0°, 22.5° and 45° (with respect to the fast axis of the incoming beam) and for different orientations of LP1. After this, the beam power right after LP2 and LP3 in figure 4.8 was measured for varying orientations of linear polarisers at LP1, 2 and 3 (also for no polariser present) and again under varying rotations of the HWP. The variations of the components are summarised in table 4.3.

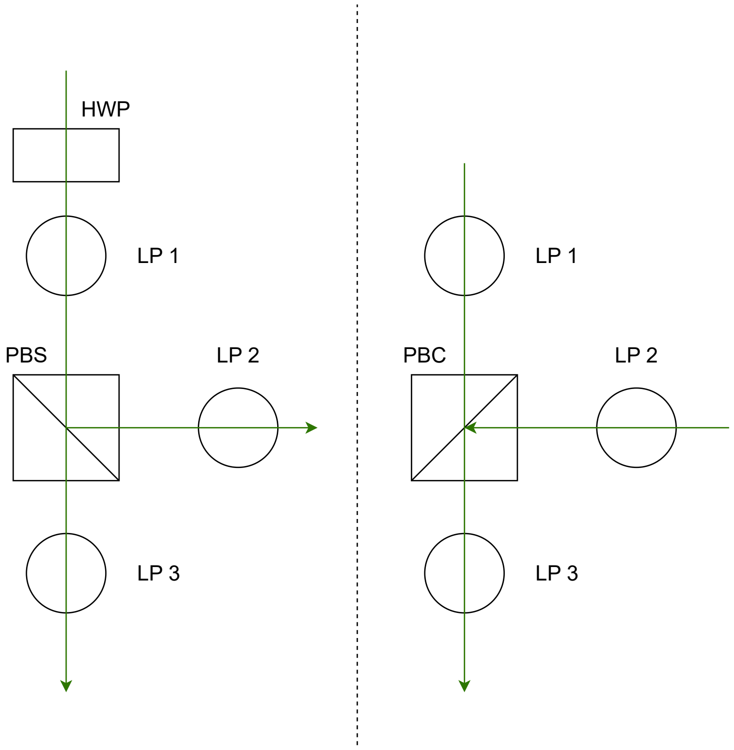

Figure 4.8: Placement of linear polarisers for the PBS and PBC

Component	Variations
HWP	0°, 22.5° and 45°
LP1	None, horizontal and vertical
LP2	None, horizontal and vertical
LP3	None, horizontal and vertical

Table 4.3: Relevant components and their states in which the measurements were conducted

These variations gave rise to a total of 63 measurements from which a number of conclusions could be drawn:

- **Polarisation state of source:** From measuring the beam power after a polariser in both orientations, the beam consisted of $55.281\mu W$ horizontal light and $0.047\mu W$ vertical light and no true zero could be found when rotating the LP freely. This indicated that the beam is elliptically or partially polarised, but the large difference between horizontal and vertical indicates it is very close to having a linear polarisation.
- **HWP characterisation:** This might seem somewhat trivial, but the measurements at LP1 for different orientations of the HWP and LP1 showed that the HWP was able to produce a rotated, nearly linear beam (due to the source beam not being linearly polarised), with the rotation angle of the beam w.r.t. the beam before the HWP being twice the rotation angle indicated on the HWP.
- **PBS transmission and reflection coefficients:** The total power of the beam after certain polariser states was too low for the available power meter (Thorlabs S121c), so a definitive quantitative characterisation was not performed. From the different measurements, the transmission

arm showed a 97.1% efficiency and an extinction ratio of $1900/1$. The reflection arm on the other hand showed 95% efficiency and an $190/1$ extinction ratio, consistent with the values reported by Thorlabs. Due to the transmissivity being higher than the reflectivity, the SPP was to be placed in the transmission arm.

A similar characterisation was also done for the PBC, with the polariser positions shown on the right hand side in figure 4.8. From this, mostly the same conclusions were drawn as for the PBS. The main goal of this characterisation was to confirm whether the polarisation state of the recombined beam would be as predicted in the setup, which it was.

From the decision of the placement for the SPP, the HWP was realigned such that the transmitted beam path would be maximum at 0° HWP orientation and called the horizontal direction. The beam path without SPP would then be at its maximum when the HWP is rotated to 45° and this polarisation state would be called the vertical direction.

4.5. Modal filtering using optic fiber

After the detrimental ripple pattern was discovered, discussions were held to find a way to filter or remove these ripples. Two main solutions were considered: clipping the beam such that only the central lobe remains or coupling the beam into an optic fiber, which would filter out the unwanted modes.

Regarding clipping, using a pinhole would require finding one which exactly matches the width of the central lobe at or near the beam waist. This requirement turned out to be difficult to meet with available components. Additionally, the placement of such a pinhole would likely require a degree of accuracy which would be very hard to obtain.

As for fiber coupling, this came with new requirements. In order to efficiently couple into a fiber, the incoming beam would need to have its beam waist match the Mode Field Diameter (MFD) of the fiber, as well as have its divergence angle match the fiber's Numerical Aperture (NA) [105]. Illustrations of these requirements are shown in figure 4.10 and figure 4.9.

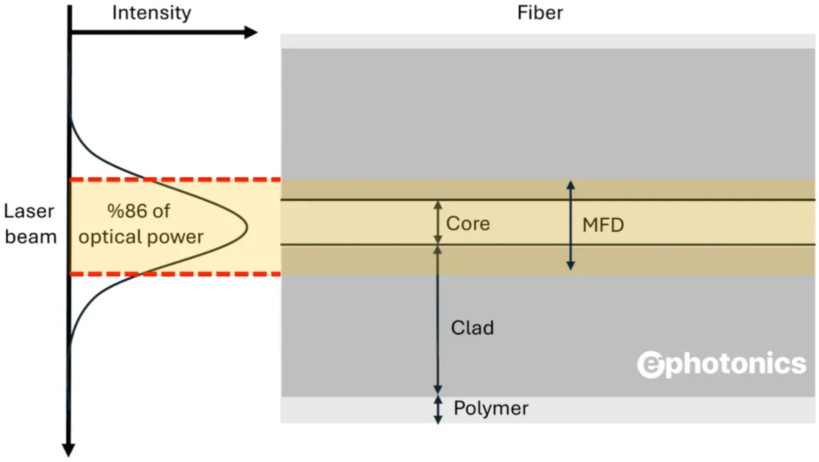

Figure 4.9: Influence of MFD on fiber coupling, image taken from [106]

The MFD of a fiber is functionally the same as the beam waist is for a Gaussian laser beam, that is, the width where the measured intensity is a fraction of e^{-2} of the peak intensity. The closer the match between the MFD of the fiber and the beam waist of the incoming laser, the better the coupling efficiency will be.

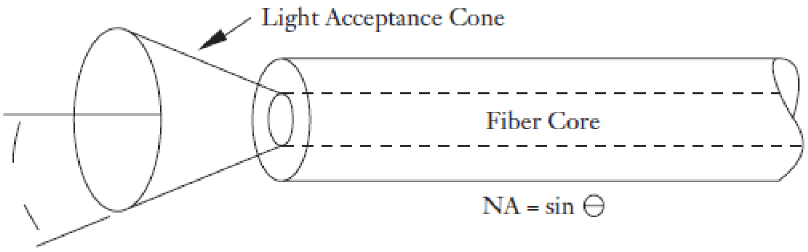

Figure 4.10: Influence of NA on fiber coupling, image taken from [107]

The NA of a fibre is a measurement of the maximum angle at which incident light can enter the core of the fiber and continue propagating inside. This angle forms what is called the light acceptance cone around the entry point of the fiber.

Usually, fiber coupling is done with the help of a fiber collimator instead of a bare fiber [108], so it was decided to follow this guidance. Alongside this, given that the divergence of a beam out of a fiber is quite significant, a collimator would also be placed at the output of the fiber, which in the new setup would take the position of the source.

To decide the optimal fiber-collimator combination, the two requirements mentioned above need to be fulfilled (assuming perfect alignment of the propagation axes of the laser and the entrance of the fiber). Their mathematical representation is shown in equations (4.2) and (4.3).

$$2w_0 = \frac{4\lambda f}{\pi D} \leq MFD \tag{4.2}$$

$$\theta_{\text{div}} = \frac{\lambda}{\pi w_0} \leq NA_{\text{fiber}} \tag{4.3}$$

In equation (4.2) D is the beam diameter at $z = 0$. From these requirements, it can be seen that a larger initial beam diameter would give a smaller beam waist, but a larger divergence angle. The opposite is true for the lens' focal length. In the case where a collimator receives a collimated beam, this focal length is the effective focal length of the collimator. The choice was made to include a lens between the source and the collimator, as the source's output has a minimum focal length of 200 mm.

A python program was written to determine the spot size and divergence angle given the focal length of the lens and the effective focal length of the collimator. These two values are then compared to the MFD and NA of a fiber, and a coupling efficiency is calculated by overlapping two normalised Gaussian distributions, one with the MFD as its waist and the other with the obtained spot size [109]:

$$\eta_{\text{coupling}} = \frac{|\int E^*_{\text{laser}} E_{\text{fiber}} dA|^2}{\int |E_{\text{laser}}|^2 dA \int |E_{\text{fiber}}|^2 dA} \tag{4.4}$$

From these comparisons, keeping in mind component compatibility with the operating wavelength, the fiber chosen was Thorlabs' 460HP fiber [110] alongside with their F220FC-532 collimator [111]. By using a 50 mm focal length lens, a theoretical coupling efficiency of 83.09% could be achieved, more than sufficient given the overabundance of power available.

Finally, as an output collimator, Thorlabs' TC12FC-532 triplet collimator [112] was chosen, as this collimator would produce the highest quality beam (with the smallest amount of aberrations) out of all available components. The collimator's triplet lenses also specifically minimise spherical aberrations, helping evade the issue present before the fiber coupling.

4.6. Final setup

Aside from the placement of the optic fiber components shown in figure 4.11, the beam path after the PBC was lengthened by using three mirrors at 45° angles in a spiral shape, bringing the path length from collimator to sensor to about 4 meter, shown in figure 4.13. This was done since during the calculation phase for the fiber coupling discussions were also held with the SPP manufacturer regarding beam development and propagation, an important issue which will be explained in section 5.3. Finally, the half-wave plate was mounted inside of a controllable electric mount to streamline the rotation process and make it more consistent.

The functionally separated diagrams of the newly proposed setup are shown in figures 4.11, 4.12 and 4.13 while the full diagram is shown in appendix B.

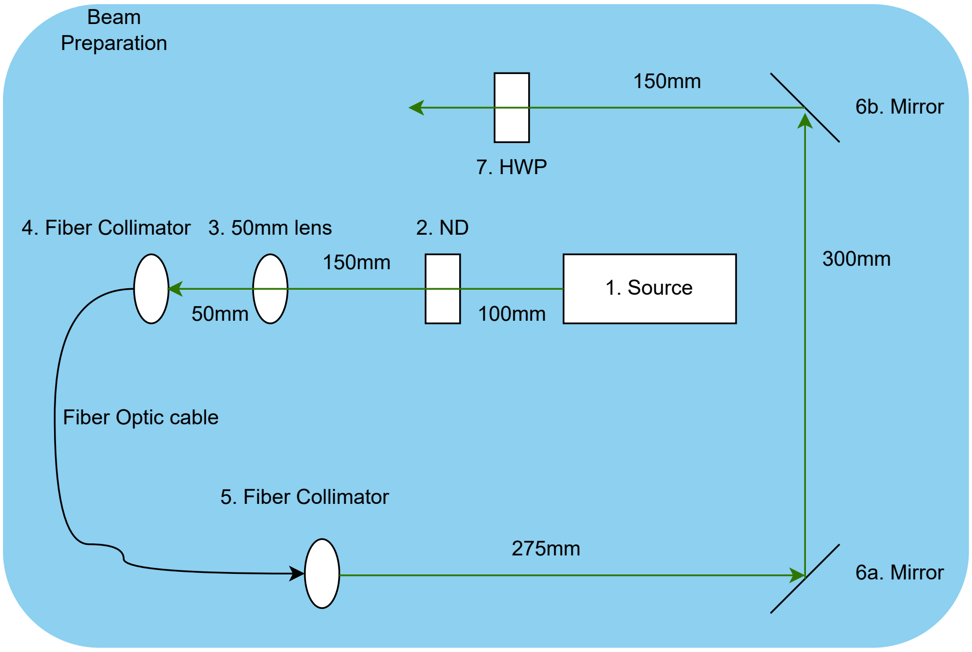

Figure 4.11: Diagram of beam preparation section with fiber coupling

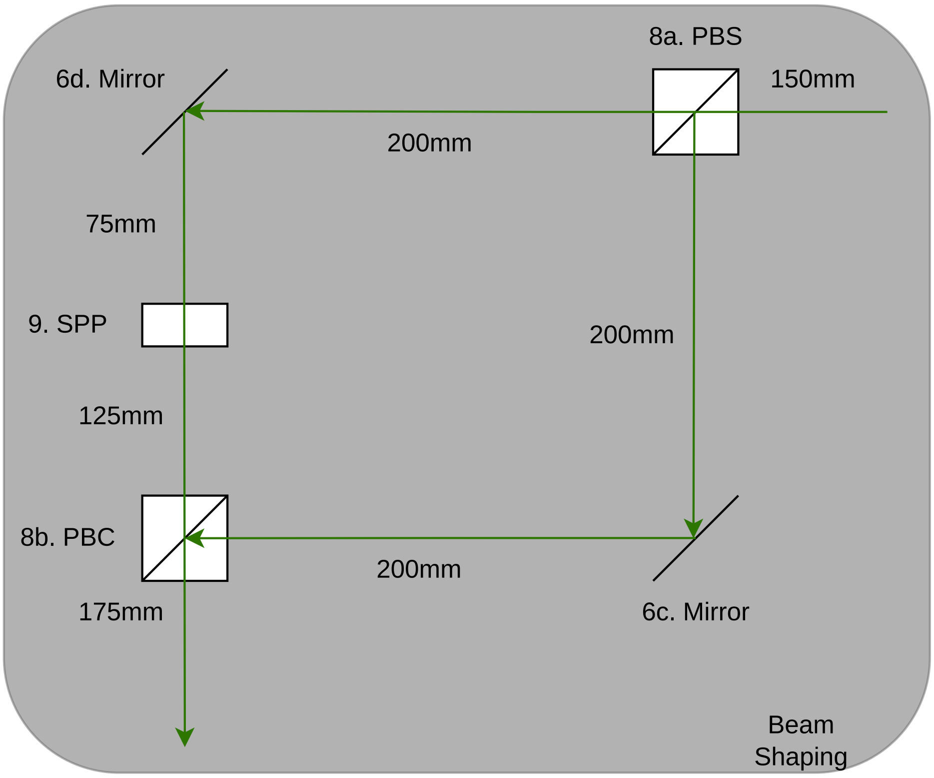

Figure 4.12: Diagram of beam shaping with fiber coupling

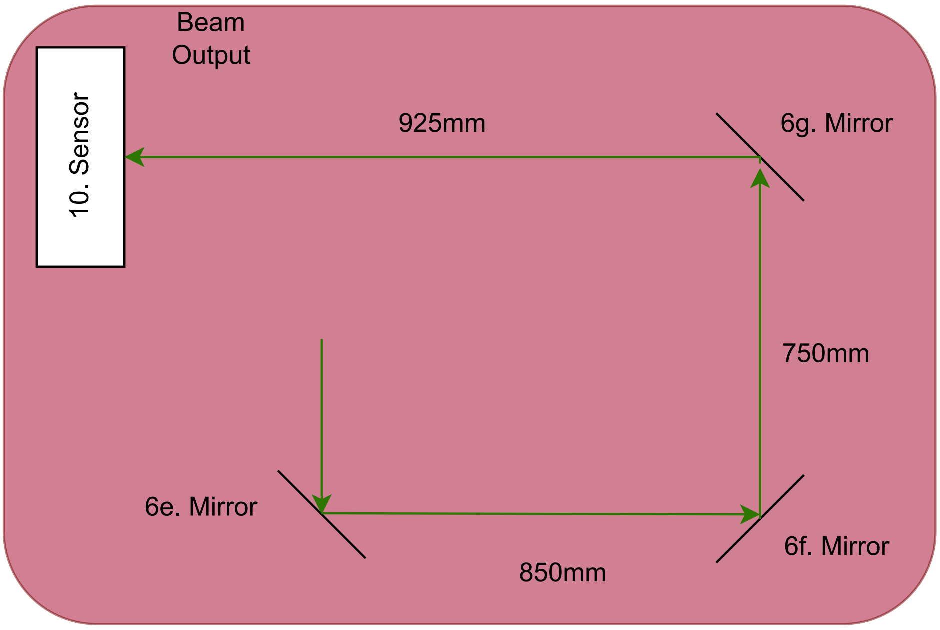

Figure 4.13: Diagram of beam output with fiber coupling

With these components, the setup was finalised and measurements could be taken, a picture taken of the setup is shown in figure 4.15 with labels and arrows pointing in the propagation direction. Different types of experiments were performed, but most important were those measuring the different ratios of vortex beam and Gaussian beam. These were achieved by rotating the HWP from 0° to 45° in steps of 4.5°, some examples are shown in figures 4.14a to 4.14e. In addition, measurements were also taken around the half-wave plate orientation which were predicted to produce the optimum beam shape for jitter management in the preceding paper [1]. These optima in the paper differ depending on the charge of the SPP, but typically lie around a HWP rotation of $10 - 20^\circ$. This is when the peaks of the vortex beam and the Gaussian beam have roughly the same value and thus the flattest possible beam profile is obtained. Thinking back to the reason for choosing a different beam profile in chapter 2, any displacement away from the beam centre here does not necessarily decrease the measured intensity, thus increasing communication performance under jitter.

Generally the experiment was performed according to these steps:

1. Power on source and controller for HWP and allow the laser output to stabilise ($\geq$15 minutes). Connect HWP controller and sensor to computer.
2. Turn off all lights and orient the computer screen away from setup.
3. Set HWP at 0° and tune sensor exposure time such that pixels would not be over-exposed for the Gaussian beam.
4. Set HWP at desired orientation, make desired changes (add or change SPP, add polariser, ...) to the setup and collect measurement.
5. Repeat until all desired data has been collected.
6. Return HWP to 0° and place setup in baseline configuration. Turn off electronics.

Another type of measurement set important to mention were those those involving interferometry. Given that the setup already shares a lot of its components and beam paths with common interferometers [113], a grid polariser could be added after the PBC to align the polarisation angle of both beams and allow them to interfere. The resulting pattern could then be compared to the simulation tool and used to determine how well the two separate beams overlapped and what their individual polarisation state were.

Something curious which was observed during the taking of images was the presence of a fringe pattern. This pattern seemed to originate from the sensor, but only rotation of the sensor around the vertical axis has any visible effect. At certain orientations the pattern showed a lot of thin lines, while at others the lines were fewer in number but thicker. It is suspected that the pattern was the result of an interference phenomenon occurring between the sensor's protective glass plate and the actual sensing area, but no conclusive cause was found. Given that the pattern was consistent regardless of the vortex-to-Gaussian ratio of the beam, it was left as an issue for the future.

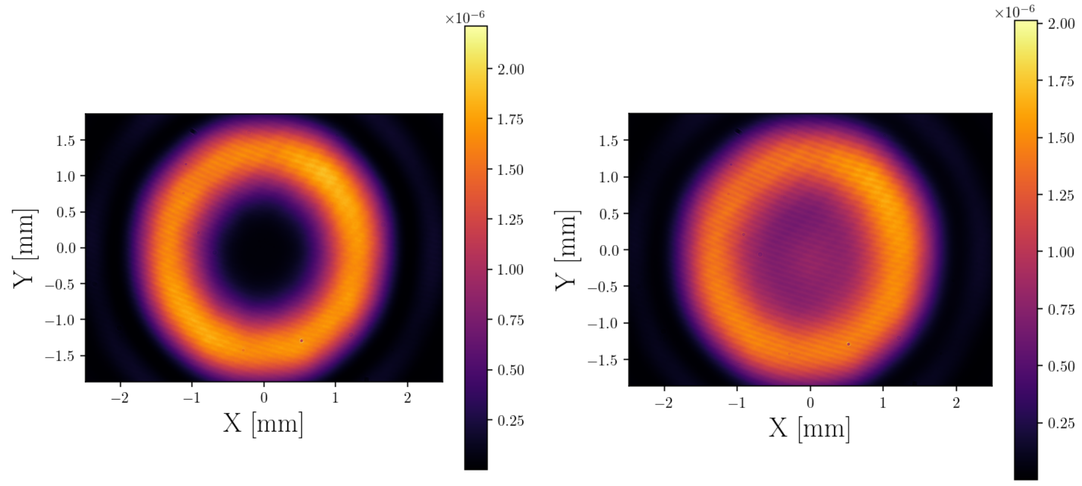

(a) Intensity profile for HWP at $0°$ (full vortex)

(b) Intensity profile for HWP at $13.5°$

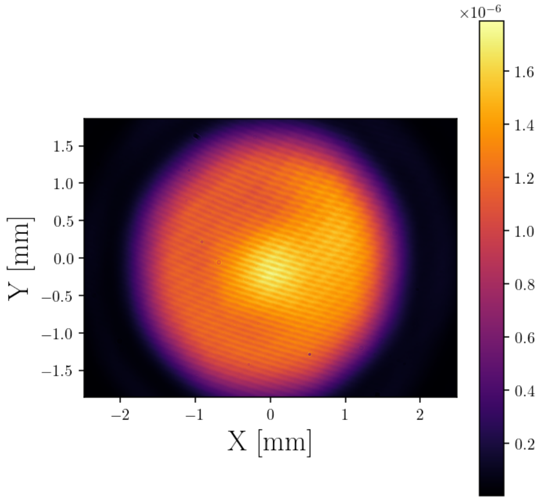

(c) Intensity profile for HWP at $22.5°$

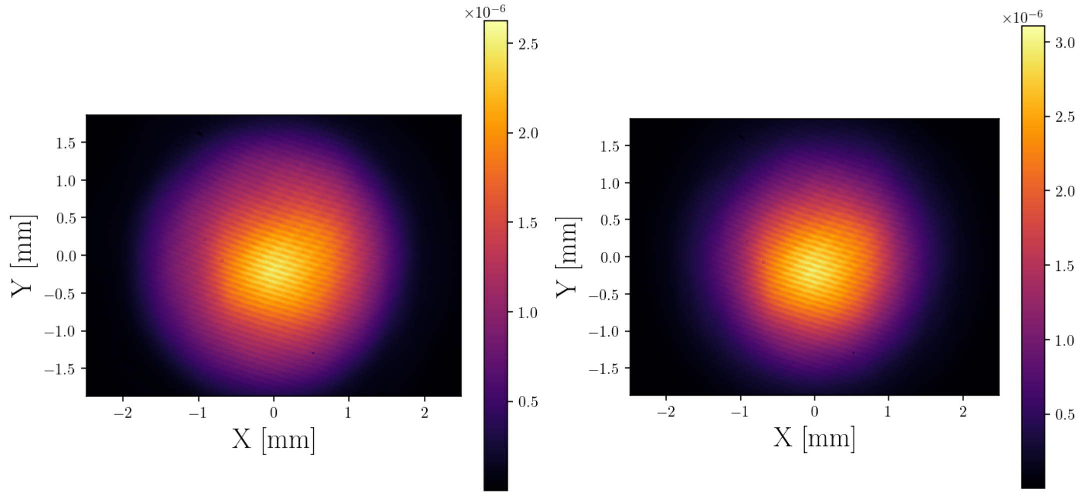

(d) Intensity profile for HWP at $31.5°$

(e) Intensity profile for HWP at $45°$ (full Gaussian)

Figure 4.14: Measured intensity profiles at various HWP orientations

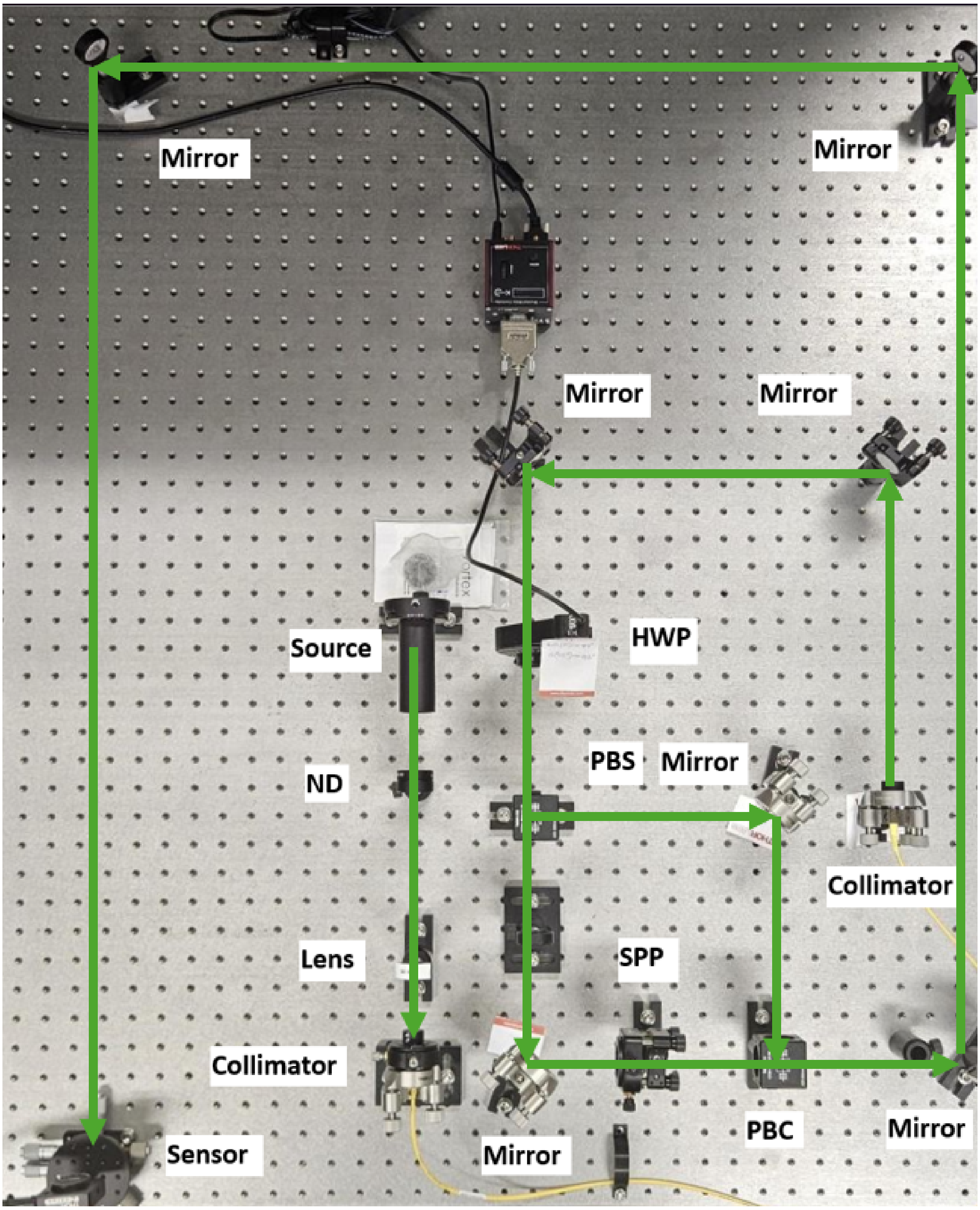

Figure 4.15: Image of the final setup in the lab

5

Verification and Validation

Although the physical setup and the programs to accompany it have now been constructed, both have to be verified before their results can be used to draw conclusions. The easiest to verify is the analysis program, as it uses simple calculations and data reading/comparing functions. Second, the setup is a physical thing and thus errors in alignment and imperfections in the components must be accounted for. Finally, the simulation program uses both complex and abstract calculations in order to simulate electric fields. It will require thorough verification by comparing it with the real world before one can trust its results.

5.1. Verification and validation of the analysis program

The main procedures used to verify the analysis program were consistency checks and looking at known or predictable results. Given the large variety of dataset gathered and simulated, it was important to ensure that all measurements be read correctly at the right time, and that data types remained constant. At certain steps throughout the construction of the analysis program, checks were made to verify whether all datasets were being read correctly and assigned to correct variables.

To validate the calculations performed by the program, such as the generation of the theoretical beams and the R^2 determination, sanity checks were applied such as using extremes, nonsensical values and comparing data to itself to verify that the results made sense.

5.2. Beam waist retrieval

The waist of a beam, w_0, is defined as the smallest radius said beam achieves. As seen from equation (5.1), the radius of a collimated beam at any other point along the propagation axis is dependent on this beam waist, the propagation distance z and the Rayleigh range z_R, which is in turn dependent on the beam waist and the wavelength.

$$w(z) = w_0\sqrt{1+\left(\frac{z}{z_R}\right)^2} \tag{5.1}$$

While the triplet collimator acting as the starting point of the system produced a beam with a theoretical beam waist diameter of $2.2mm$ with a full angle divergence of $0.017°$ [112], some imperfections in the mounting and fiber coupling could cause this to differ in reality. To find the true beam waist, simulations were made for a variety of different beam waist of both the Gaussian and the vortex beam paths. A couple of examples are shown in figures 5.1a to 5.1d. These simulations were then compared to the measured beams and each R^2 value was plotted, shown in figure 5.2.

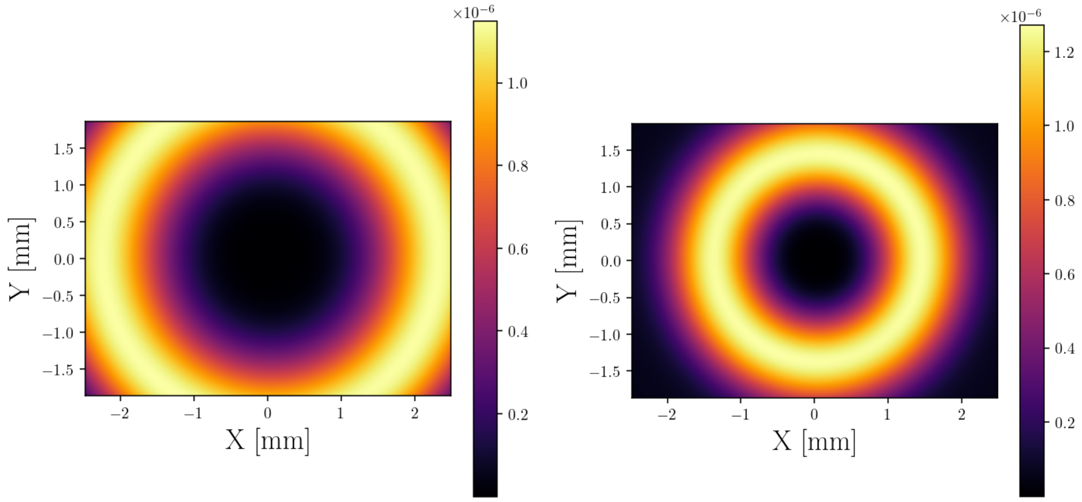

(a) Intensity profile for a simulated vortex beam with $w_0 = 0.2$mm

(b) Intensity profile for a simulated vortex beam with $w_0 = 0.6$mm

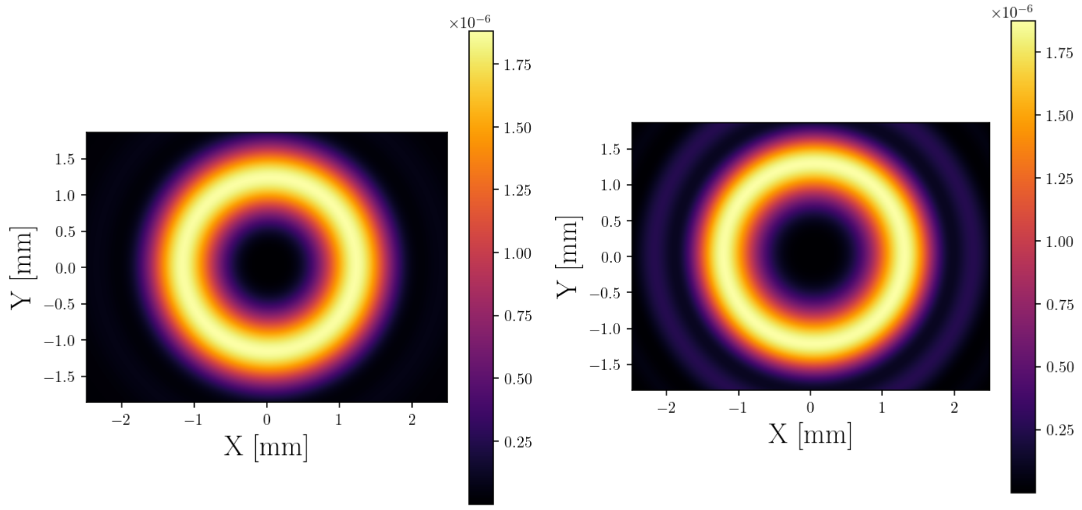

(c) Intensity profile for a simulated vortex beam with $w_0 = 1$mm

(d) Intensity profile for a simulated vortex beam with $w_0 = 1.8$mm

Figure 5.1: Intensity profiles of vortex beams simulated with various beam waists

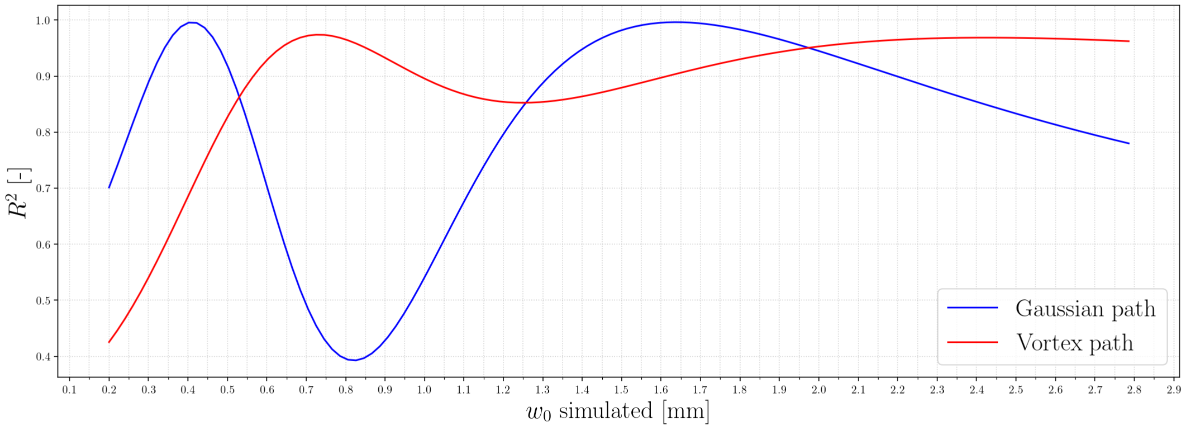

Figure 5.2: R^2 values for the Gaussian and vortex beam paths for simulations of different beam waists

In this plot, it can be seen that both the Gaussian and the vortex beam simulation can produce results that match the real measurements well, with R^2 values very close to one. The values are the highest for the Gaussian path, to be expected as it is the beam path which encounters the least amount of components and the Gaussian is already the fundamental mode carried through the fiber into the collimator.

The nature of the graphs, with the double peaks, also makes sense when one considers that the R^2 value will also be highly dependent on beam radius, dictated by $w(z)$ seen in equation (5.1). Plotting $w(z)$ for a variety of different w_0 shows that at a specific propagation distance, two different beam waists can result in the same beam radius. This means that the simulations will produce two beams which look roughly the same, and thus will receive almost the same R^2 value.

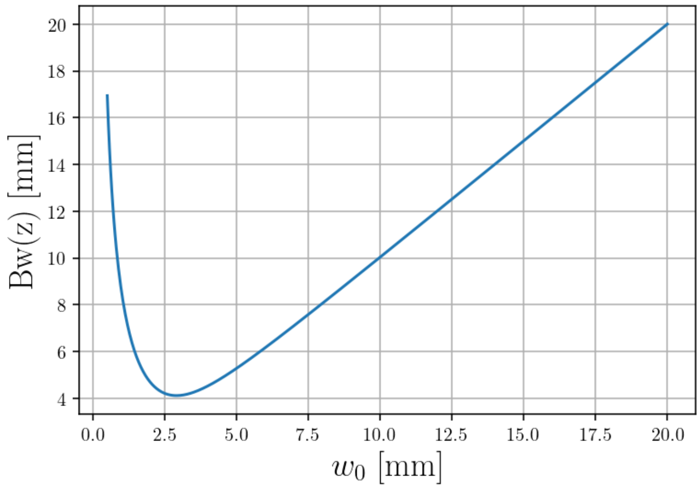

Figure 5.3: Beam radius for a given propagation distance and different beam waists

When looking at the R^2 graphs, one issue that was initially clear was that none of the peaks were particularly close to the theoretical w_0 of 1.1mm indicated by the data sheet of the collimator. Another substantial problem is that the values of w_0 where the peaks occur for the Gaussian and the vortex beam do not overlap. While it is to be expected that the values for R^2 themselves would differ, with the Gaussian results being better, the w_0 at which they occur should be the same for two beams originating from a singular source. The shift in the peaks' location suggests a lens-like effect affecting the vortex beam path only or in a different manner as the Gaussian path.

In order to narrow down the possible origins of this effect, a few additional tests were conducted. First, to see if the SPP itself was acting like a lens of sorts, measurements were taken of the SPP flipped around the vertical axis by 180°. When compared to the original SPP orientation the R^2 peaks occurred at the same w_0, seen in figure 5.4. Were the SPP to be acting like a lens, a shift in the location of the peaks would have been expected.

Measurements were also taken of the setup without the SPP present to completely remove suspicions of the SPP being the culprit of the discrepancy. Once again, in figure 5.5 it can be seen that the peaks occurred at the same location.

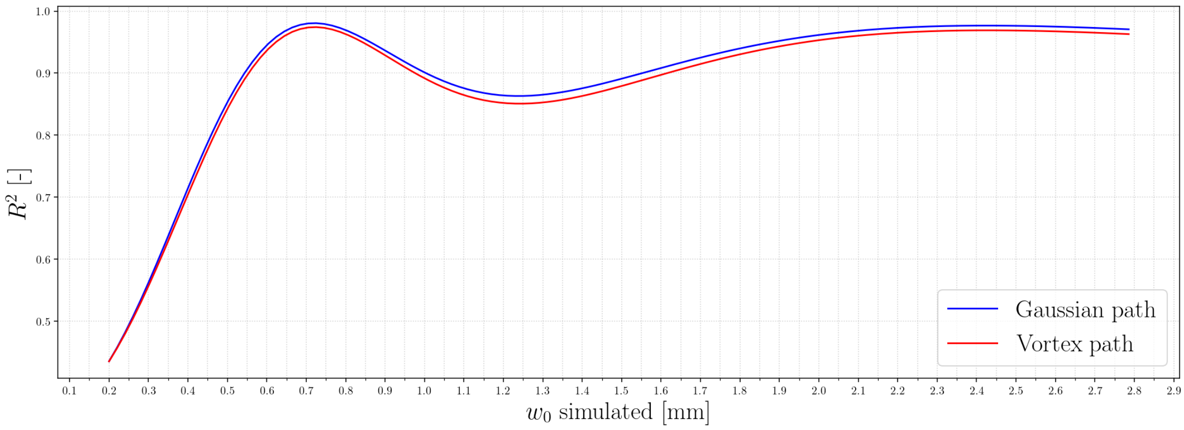

Figure 5.4: R^2 values for the original and flipped SPP orientation for simulations of different beam waists

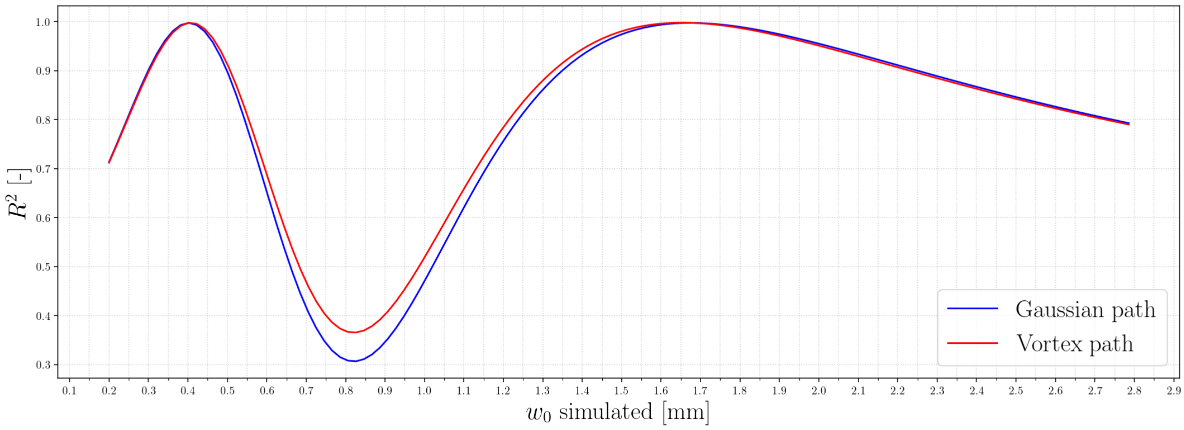

Figure 5.5: R^2 values for the Gaussian and vortex beam path without SPP for simulations of different beam waists

Outside of the SPP, there was no substantial difference in the beam paths, and so the next potential cause was that the beam exiting the collimator was not perfectly collimated, and that the resulting radius of curvature affected the vortex beam in a different way to the Gaussian beam path.

Thus, new simulations were made by simulating a thin lens at the collimator, starting a two-dimensional parameter search for w_0 and the focal length of the lens f. To obtain initial guess values, a least-squares search for w_0 and z using equation (5.1) was performed. z in this case consisted of z_{Prop}, the distance from the collimator, and z_{Col}, the virtual distance a collimated beam would need to have travelled before the collimator in order to achieve the $w(z)$ of measurements taken of the Gaussian beam at different distances from the collimator. From these results, an initial guess for w_0 of 1.05mm and z_{col} of 3.89m were obtained. From equation (5.2), the radius of curvature of the beam would have to be around 13.7m, which would equal to a thin, divergent lens with a focal length of 13.7m.

$$R(z) = z\left[1 + \left(\frac{z_R}{z}\right)^2\right] \tag{5.2}$$

$$z = z_{\text{prop}} + z_{\text{col}} \tag{5.3}$$

Around these initial guesses a grid of simulations was set up for various values of w_0 and f, and compared to the measurements in a similar fashion to the original w_0-search. Their results are shown in figure 5.6a and figure 5.6b, while the product of both R^2 values is shown in figure 5.6c.

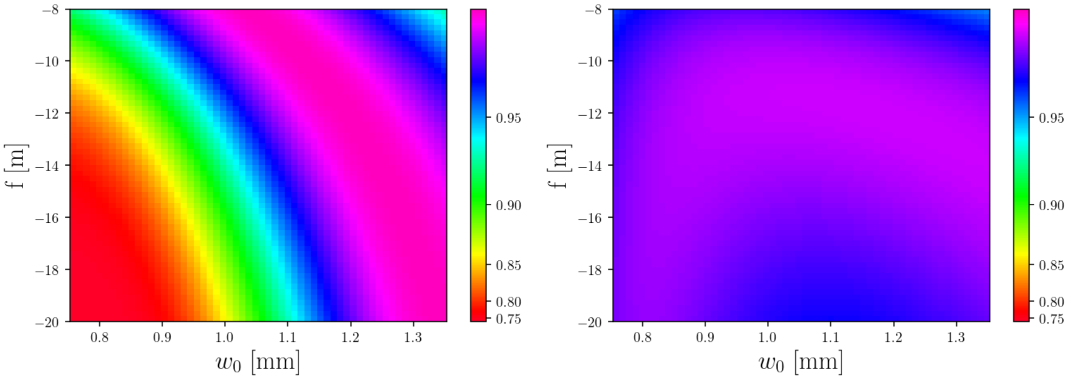

(a) R^2 values between measured and simulated Gaussian beam for varying focal lengths and beam waists

(b) R^2 values between measured and simulated vortex beam for varying focal lengths and beam waists

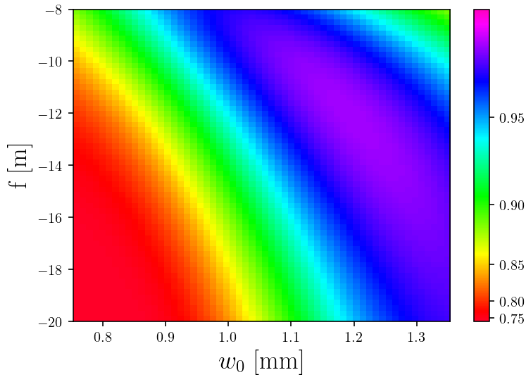

(c) Product of the R^2 values between measured and simulated beams for varying focal lengths and beam waists

Figure 5.6: Resulting R^2 values for varying focal lengths and beam waists simulated

The peak value of the product occurs at $f = 12$m and $w_0 = 1.1951$mm, where the Gaussian beam simulation shows an R^2 of 0.996 and the vortex beam shows 0.986. The resulting w_0 also closely matches the 1.1mm one indicated on the collimator data sheet, which lends credit to the idea that this approach might be the correct one.

These checks were also done for different datasets, such as using a different $\ell = 2$ SPP or an $\ell = 1$ SPP, and all produced similar numbers. Thus going forward, all simulations would be made using this beam waist and applying a thin lens at the collimator to simulate the non-perfect collimation at the aperture.

5.3. Propagation and beam development

Now that a matching beam waist and radius of curvature had been determined, the development of the beam is discussed. During the setup process, the observation was made that after the Gaussian input had encountered the SPP, the shape of the beam changed depending on propagation distance. This meant that the intensity profile of the vortex beam was not stable from the start in the same way as the Gaussian was. Unfortunately, there was not enough space on the optical bench to capture the fully developed beam and as such the decision was made to ensure the simulation program could match the developing stages of the beam which could be captured. Then the propagation distance within the program could be increased to show what the developed beam would look like.

Figures 5.7, 5.8, 5.9 and 5.10 show the intensity profile of the beam at different distances from the SPP, for the simulation and the experimental beam respectively. Apart from imperfections stemming from a variety of sources (misalignment, imperfect input beam, simulation distance being too short for the Fresnel approximation, ...), the developmental stages of the beam are well captured in the simulation. The leftmost image is the experimental beam as captured by the sensor, the middle image is the simulated beam and the rightmost image is the resultant of subtracting the simulation from the measurement, to clearly visualise mismatches.

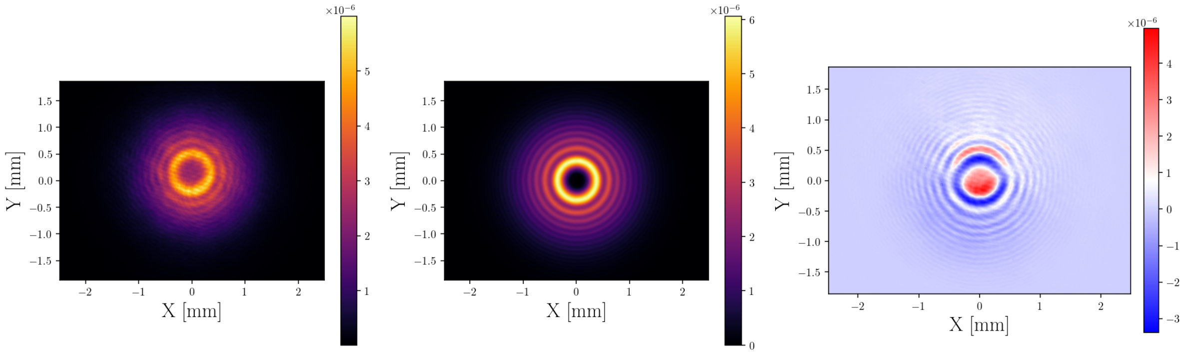

Figure 5.7: Measurement, simulation and resultant 200 mm after the SPP

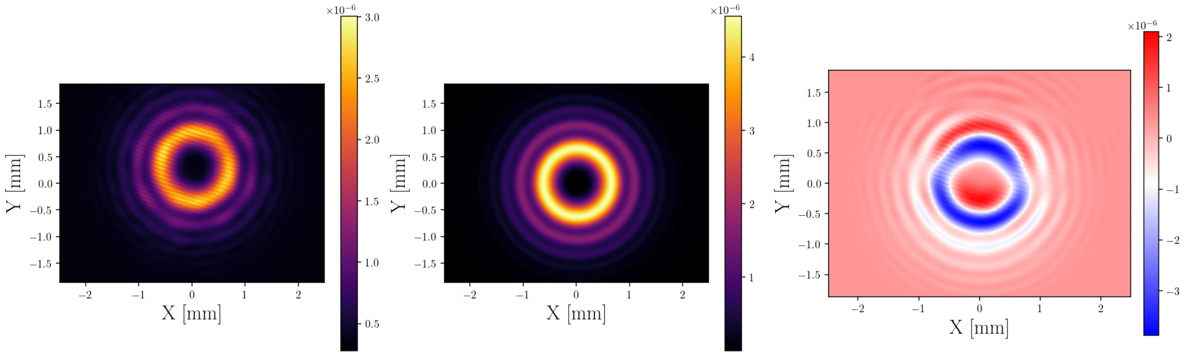

Figure 5.8: Measurement, simulation and resultant 625 mm after the SPP

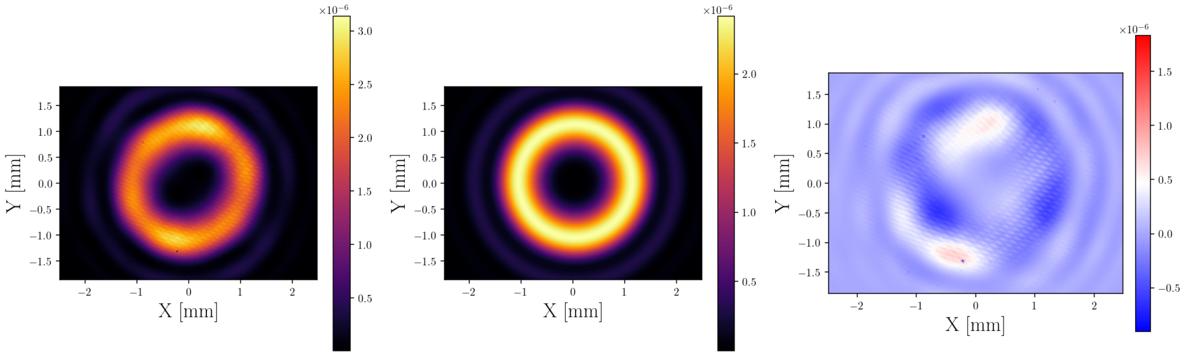

Figure 5.9: Measurement, simulation and resultant 1900 mm after the SPP

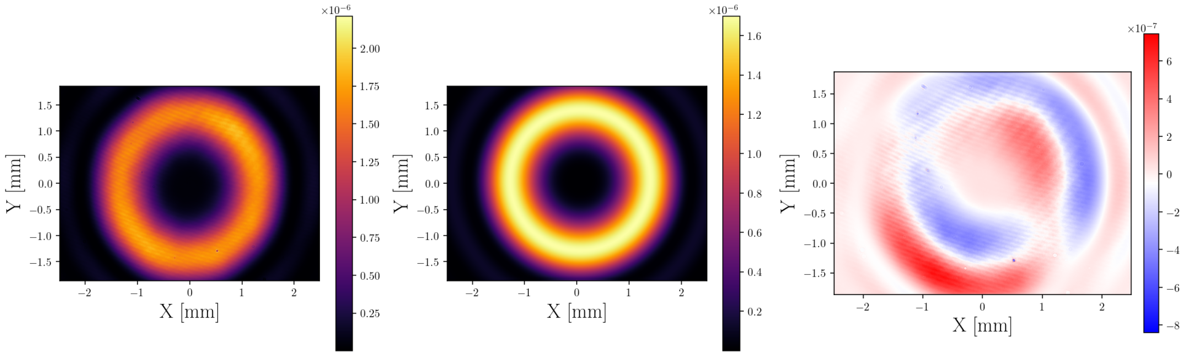

Figure 5.10: Measurement, simulation and resultant 2825 mm after the SPP

With the simulation program capable of showing how the beam would develop beyond the spatial capability of the lab, the investigation into its final shape and its correspondence to the LG distribution could start, since it had been assumed from the start that a Gaussian beam impinging an SPP would result in a pure LG beam.

Quickly it became obvious that something was not as expected. While the shape stabilised into something strongly resembling a pure LG beam, it never completely matched. Shown in figures 5.11 and 5.12, the difference is especially visible when forcing the maxima to overlap. The ring of the simulated beam seems to be wider and more diffuse than one would expect from a true LG beam.

Furthermore, while in theory the definition of beam radius varies depending on the Gaussian or charge of LG under consideration, the rate at which it increases with propagation should follow the same formula (equation (5.1)). However, looking at either the beam waist for the best fit or for the derivative-based maximum intensity location, the beams radius of the simulated beam did not follow this formula.

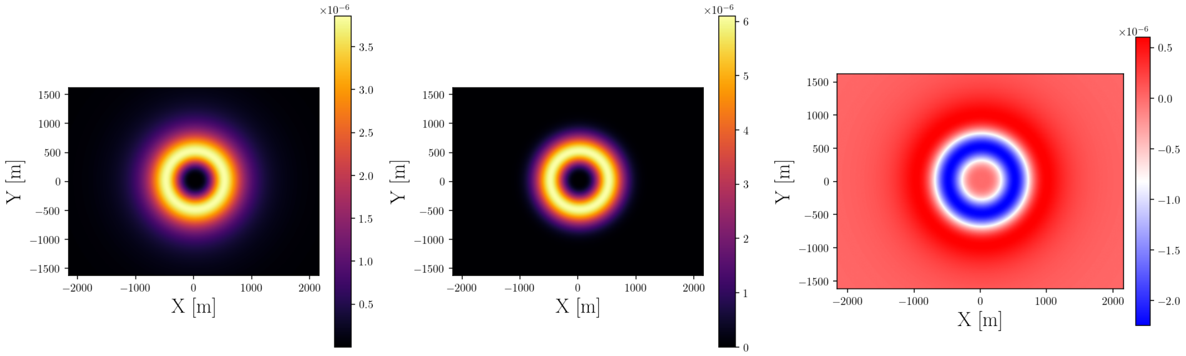

Figure 5.11: 2D simulated $\ell = 2$ beam against LG expression at a propagation distance of $\sim 3e12m$

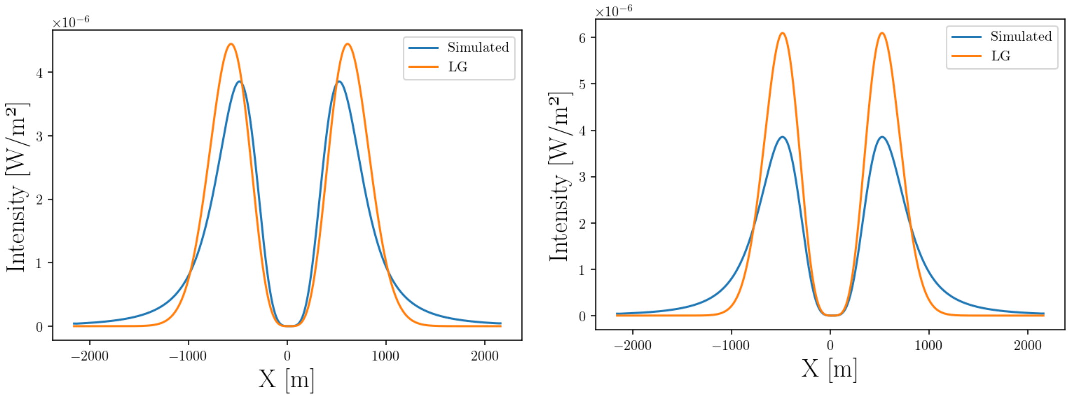

(a) Best fit for the simulated $\ell = 2$ beam

(b) simulated beam and LG beam with maximum intensity at the same position

Figure 5.12: Results for the comparison between the simulated and LG beam using an SPP of charge 2 at a distance of $\sim 3e12$m.

In order to discover the source behind these inconsistencies simulations were for exponentially increasing propagation distances and with a variety of different setup configurations. Simulations were made for SPP's with charges 1, 2 and 3, no SPP, Fraunhofer propagation instead of Fresnel (thus using a different, generally less accurate approximation), placing an LG beam directly at the input field, and many more.

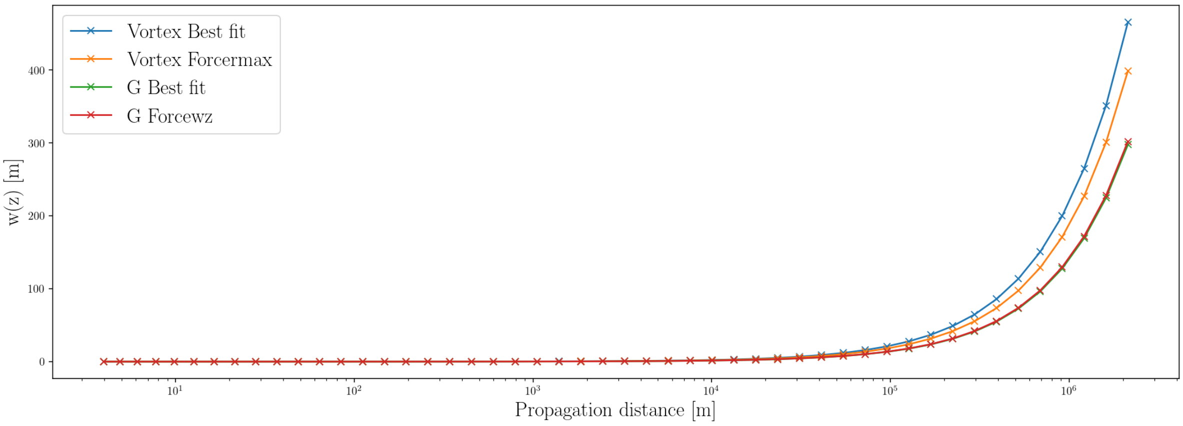

Figure 5.13: $w(z)$ estimated by the analysis program for single step propagation of an SPP with charge 1

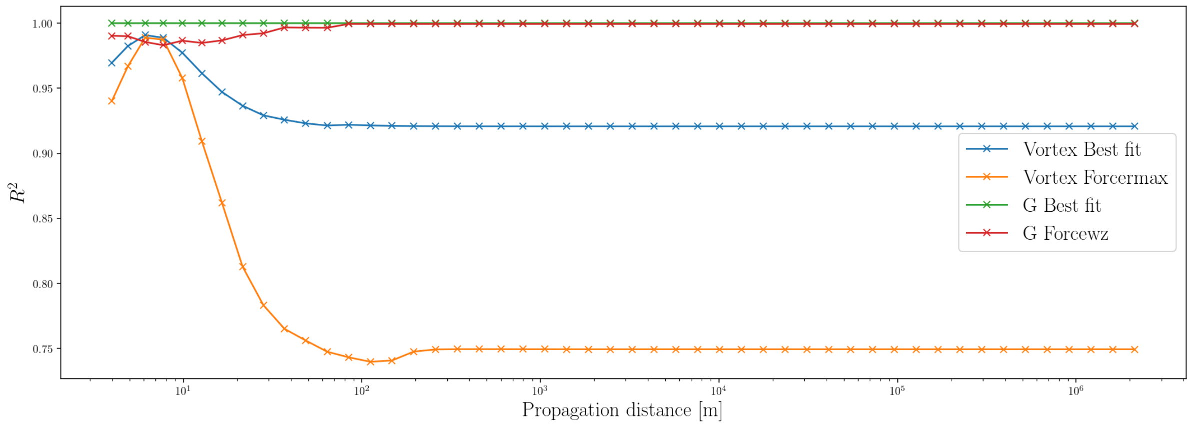

Figure 5.14: R^2 calculated by the analysis program for single step propagation of an SPP with charge 1

Figures 5.13 and 5.14 show the results of one of these configurations. For both graphs, the horizontal axis represents the simulated propagation distance in a logarithmic scale, up to a distance of 213 km, a reasonable distance for orbital inter satellite communication. The red line shows the radius the beam should have when following equation (5.1), the green line shows the estimated beam radius of the Gaussian case, the orange line the beam radius when forcing the maxima to coincide and the blue line shows the beam radius of the best fitting LG profile for the simulation. The first graph shows the disconnect between $w(z)$ of the vortex beam path and that of the Gaussian path, and while the values differ between different configurations, each test which included an SPP showed this trend, while those that did not had all 4 curves coincide, as was expected previously. The graph representing the R^2 values shows that while the simulated vortex beam eventually develops into a stable profile, it never matches a pure LG after this development. These conclusions are drawn from the fact that R^2 converges, but not to one, especially for the overlapping maxima of the *Forcermax* function.

These outcomes confirmed a rising suspicion that the beam produced by an SPP is not truly a LG beam, although it does share many characteristics. It is in fact a superposition of true LG beams [54]. To determine the true expression of this beam, the co-supervisor of this project, Mario Badás Aldecocea, analytically derived the effect of applying an SPP using the Fraunhofer approximation, given in appendix A. The expression in polar cylindrical coordinates is given in equation (5.4).

$$E^{\ell}_{\text{SPP}}(\rho,\theta,z) \propto 2\pi(j^{\ell})\,\text{exp}(j\ell\theta)\,\text{exp}(jkz)\,\text{exp}\left(\frac{jk\rho^2}{2z}\right)\frac{1}{j\lambda z}\frac{\pi^{3/2}\rho w_0^3}{4\lambda z}\,\text{exp}\left(-\frac{\pi^2\rho^2 w_0^2}{2\lambda^2 z^2}\right)$$
$$\left(\mathcal{I}_{\frac{\ell-1}{2}}\left(\frac{\pi^2\rho^2 w_0^2}{2z^2\lambda^2}\right)-\mathcal{I}_{\frac{\ell+1}{2}}\left(\frac{\pi^2\rho^2 w_0^2}{2z^2\lambda^2}\right)\right) \tag{5.4}$$

In this equation, ℓ denotes the charge of the SPP,k is the wave number $\frac{2\pi}{\lambda}$, ρ the radial coordinate, θ the angular coordinate and $\mathcal{I}$ is the modified Bessel function of the first kind.

Using the square of this expression as a substitute for the LG (equation (2.6)) results in a shape which closely matches the simulation, as seen in figures 5.15 and 5.16.

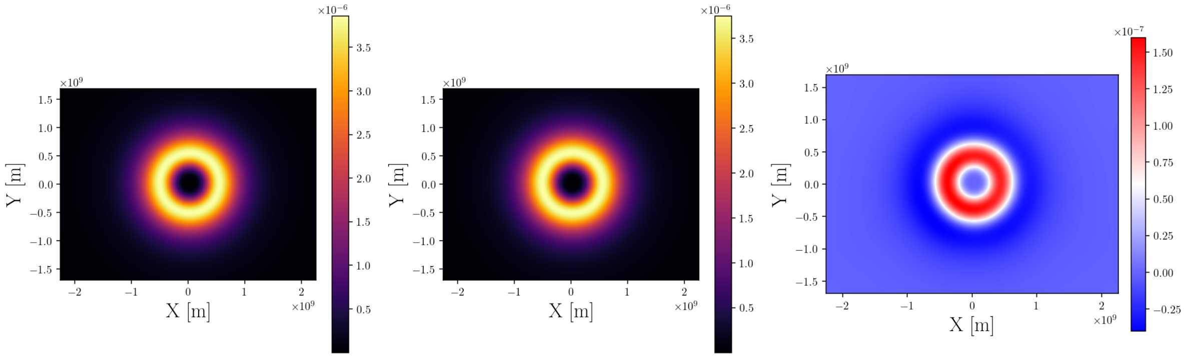

Figure 5.15: 2D simulated $\ell = 2$ beam against new electric field expression at a propagation distance of $\sim 3e12$m

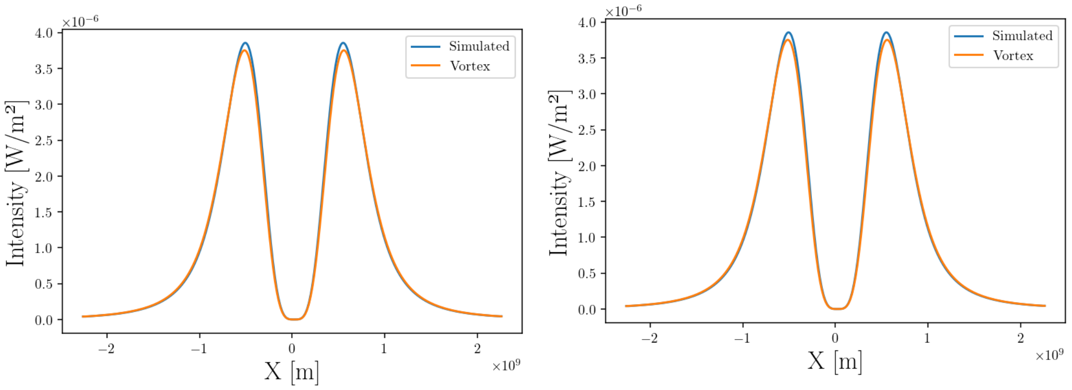

(a) Best fit for the simulated $\ell = 2$ beam

(b) simulated beam and new electric field expression with maximum intensity at the same position

Figure 5.16: Results for the simulated and new electric field expression using an SPP of charge 2 at a distance of $\sim 3e12$m.

While for this new expression the equation for the evolution of the beam radius equation (5.1) no longer holds, the beam waist w_0 from which the analysis program estimates both beam paths to originates now once again matches.

From literature [114], the vortex beam resulting from an SPP can be represented as an infinite sum of LG beams, also known as a Kummer beam [115], where over 80% of the total energy is carried by the main LG beam of the same charge as the SPP. This value is verified by the fact that the integral overlap between LG and vortex varies from 80% to 90% depending on the SPP charge used. Thus the generated vortex beam can serve as a good replacement for a pure LG beam.

5.4. Validation of the setup

Now that the simulation program could produce a satisfying result to compare the baseline setup, the sensitivity analysis can be performed.

The first major misalignments to analyse are those of the SPP, both linear and angular (figure 3.4. This was accomplished by first aligning the SPP as well as was possible with the naked eye (estimated to be accurate in the range of tens of micrometres) and then purposefully misaligning by use of the linear/angular adjuster screws (mount with screws shown in figure 5.17). The smallest and largest linear displacements measured are shown in figure 5.18a and figure 5.18b respectively.

Figure 5.17: Thorlabs K5X1 mount used to hold the SPP. Image taken from [116]

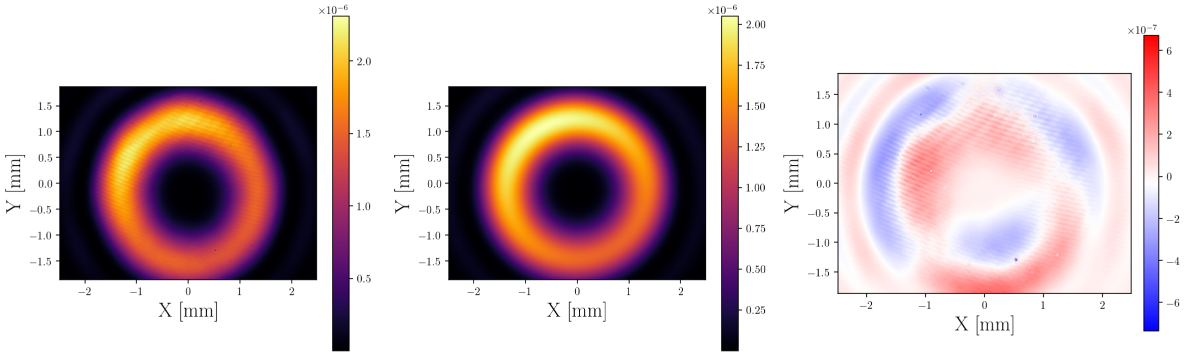

(a) Linear displacement of $127\mu m$

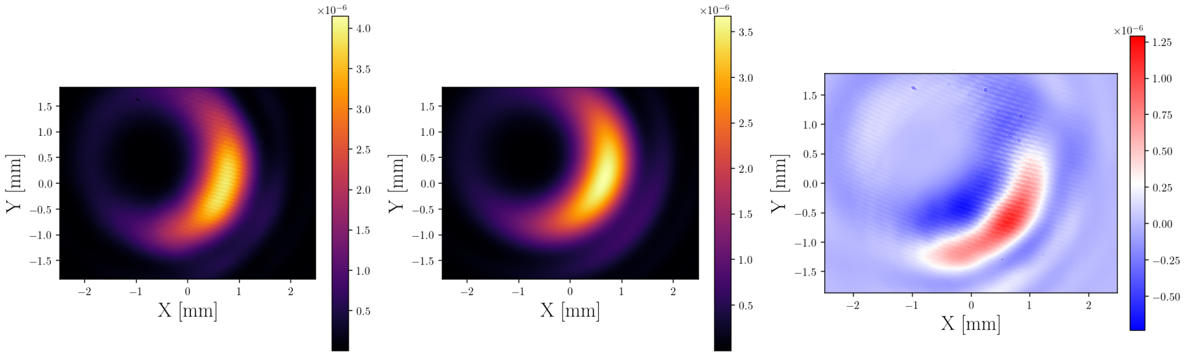

(b) Linear displacement of $359\mu m$

Figure 5.18: Effect of a linear displacement between the centre of the beam and the centre of the SPP

From these measurements and simulations it becomes clear that the simulation program is capable of accurately simulating linear displacements and that the SPP is particularly sensitive to these displacements

Regarding the angular misalignment however, the SPP showed very little sensitivity for small angles. The 5-axis mount upon which the SPP was situated allowed for a maximal angular displacement of $4°$, at which point the physical beam showed little to no alteration. Alteration did become apparent with larger angles, on the order of tens of degrees. However, in order to achieve these the SPP had to be taken out of its mount and held manually, making stable measurements impossible. With the simulation program it becomes possible to simulate the effect of large angular misalignments, shown in section 5.4, section 5.4 and section 5.4.

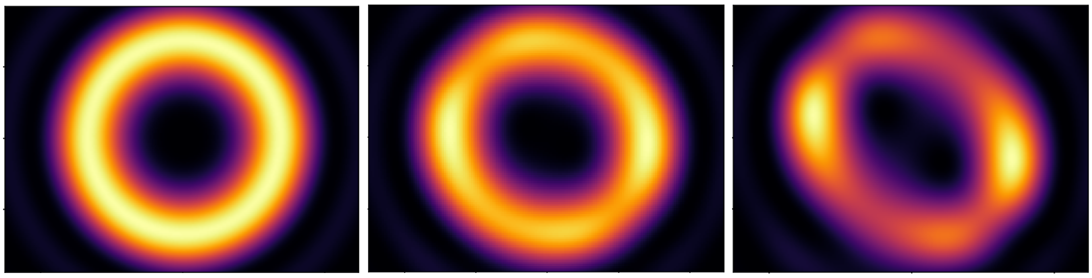

Figure 5.19: Angular displacement simulation of $0°$, $20°$ and $40°$ from left to right.

These simulations show the magnitude of misalignment required in order to show visible deformation, and the type of deformation also matches that which was seen in the lab. From these results leads that the SPP is not sensitive to angular misalignments on the scale that can be expected within an aligned setup.

The second major type of misalignment that can occur in the system lies between the two different beam paths. When recombining it is imperative that both beam paths align completely. There are at least two ways to verify this: simulate the beam simply with a physical misalignment between the beams, or simulate the system including a grid polariser after the PBC to induce interference fringes. Section 5.4 and Section 5.4 show the measured beam with the HWP at $22.5°$ and the grid polariser at $45°$, the point where the maximum amount of interference should take place.

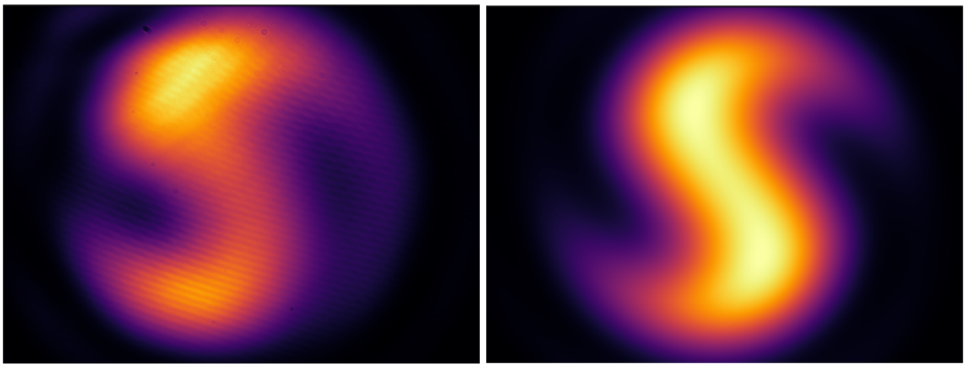

Figure 5.20: Interference patterns obtained through measurement on the left and simulation on the right

The interference patterns break the circular symmetry of the total beam and shift rapidly with even small misalignments, making it easier to visually confirm the nature of the misalignment. The effect of a linear misalignment of the beam centres of 0.1mm is shown in figure 5.21a and figure 5.21b for both with and without interference.

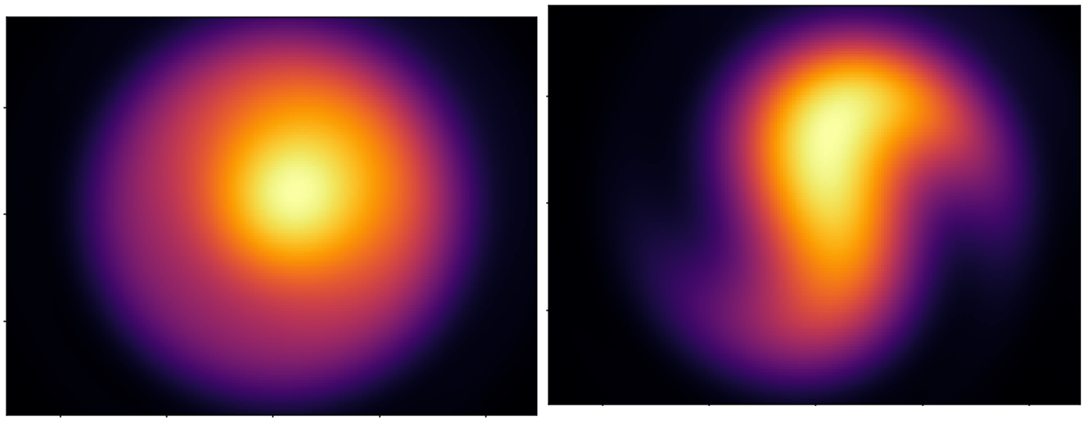

(a) Linear displacement of vortex and Gaussian paths by 0.1mm

(b) Linear displacement of vortex and Gaussian paths by 0.1mm with interference

Figure 5.21: Difference in intensity profile for orthogonally polarised beams on the left and parallel polarised beams on the right with a linear displacement

The use of these figures by comparing them to the real beam allowed for a more accurate alignment than was possible with the naked eye alone.

Finally, other types of possible misalignment are those regarding other components such as the mirrors, but these would only result in the beam as a whole shifting and could easily be fixed by aiming at the sensor, while they did not affect the shape of the beam.

6

Results, analysis and recommendations

In this chapter, all of the previously presented information will be used in order to answer the research questions posed at the start of this project. At first, the total transmissivity of the core beam shaping components (PBS, SPP, mirrors and PBC) will be evaluated against the theoretical gains from [1]. Second, the obtained intensity profile of the beam will be compared to the simulated profile and the simulation will be compared to the profile created using the theoretical expression obtained in section 5.3, answering the question if it is possible to accurately generate these vortex beams. The last question to be answered then will be how well the obtained beam shape performs when put under the same performance analysis for power outage probability as a pure LG beam.

6.1. Power Efficiency

To compare the transmissivity of the system constructed during this project against a standard FSOC system, only the main difference, the beam shaping section, has to be considered, as in an operational system the source would be selected such that the beam preparation steps are not needed by determining beforehand the optimum polarisation state of the source. This section starts right after the HWP and ends after the PBC and contains the beam splitter, two mirrors, the SPP and the beam combiner. In theory, the combined transmissivity of this section should follow equation (6.1).

$$\eta_{\text{BS}} = \alpha \eta_{\text{PBS}_T} \eta_M \eta_{\text{SPP}} \eta_{\text{PBC}_T} + (1-\alpha) \eta_{\text{PBS}_R} \eta_M \eta_{\text{PBC}_R} \tag{6.1}$$

In this equation, α is the fraction of vortex beam to Gaussian beam power given by $\cos^2(2\theta_{\text{HWP}})$ similar to equation (4.1), η_{PBS_T} and η_{PBS_R} are the transmissive and reflective efficiencies of the PBS, η_{PBC_T} and η_{PBC_R} are those of the PBC and have the same values as for the PBS, η_{SPP} is the SPP transmissivity and η_M is the reflectivity of the mirrors. At a HWP orientation of $22.5°$ the fraction α becomes 0.5, and the expression simplifies to:

$$\eta_{\text{BS}} = \frac{1}{2}\eta_M \left(\eta_{\text{PBS}_T}^2 \eta_{\text{SPP}} + \eta_{\text{PBS}_R}^2\right) \tag{6.2}$$

The efficiencies of the beam splitters were obtained in section 4.4 and the efficiency of the mirrors is close to 99% [99]. To obtain the SPP efficiencies, a power meter was used before and after various SPPs, resulting in an efficiency of 94% for $\ell = 1$ and 85% for $\ell = 2$. These figures give a total theoretical beam shaping efficiency of 84%. Measurements using the power meter after the HWP and after the PBC, using an SPP of charge 2, read $60.55\mu W$ and $50.5\mu W$ respectively, resulting in an actual efficiency of 83.4%, close to the theoretical value.

In the original paper, potential power savings were calculated to be ranging from 20% to 40%, showing that even with the increased losses incurred by shaping the beam, this novel setup could still result in lower power requirements. This efficiency could be further improved by using components more fine tuned for the wavelength in question.

6.2. Beam shape comparison

While section 5.2 and section 5.3 have shown how the size and shape of both beam paths can be closely matched in the simulation tool, neither the vortex beam nor the Gaussian beam alone was given as the optimal combination of Gaussian and LG beam in the original paper [1]. Simulations and measurements were made with different rotations of the HWP, ranging from $0°$ to $45°$ in $4.5°$ increments and then compared to one another. The box plots of the R^2 values obtained by using equation (3.18) of these orientations for SPP's with charge 1, 2 and 3 are shown in figure 6.1, figure 6.2 and figure 6.3 respectively. The distribution parameters were obtained by calculating the R^2 values of one dimensional slices of the two dimensional beam profile taken by rotating around the central point of the beam. In this way, the distribution and minimum/maximum also serve as an indication of rotational symmetry.

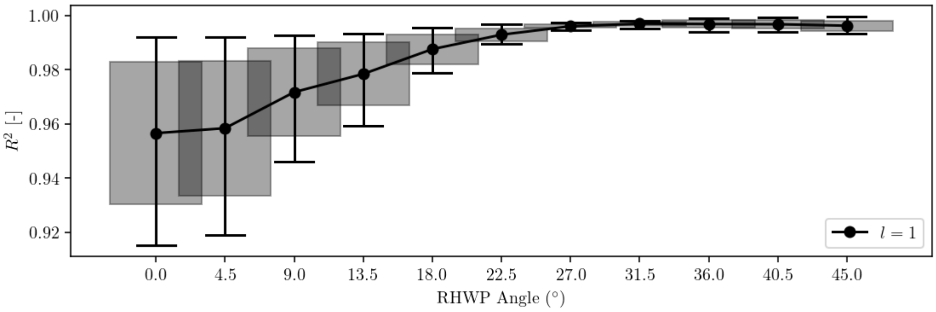

Figure 6.1: Box plot of the R^2 values for $\ell = 1$

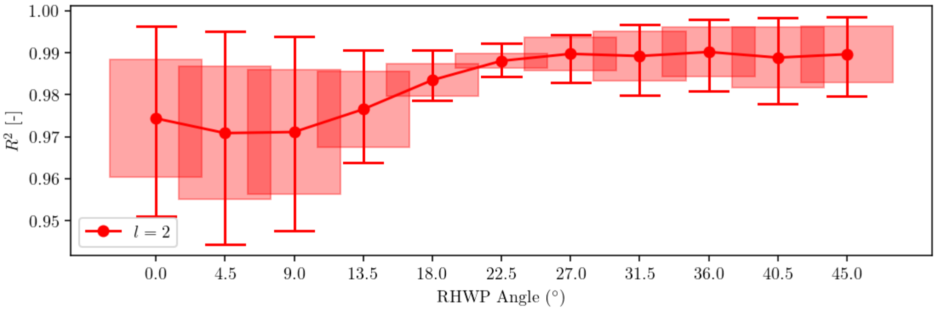

Figure 6.2: Box plot of the R^2 values for $\ell = 2$

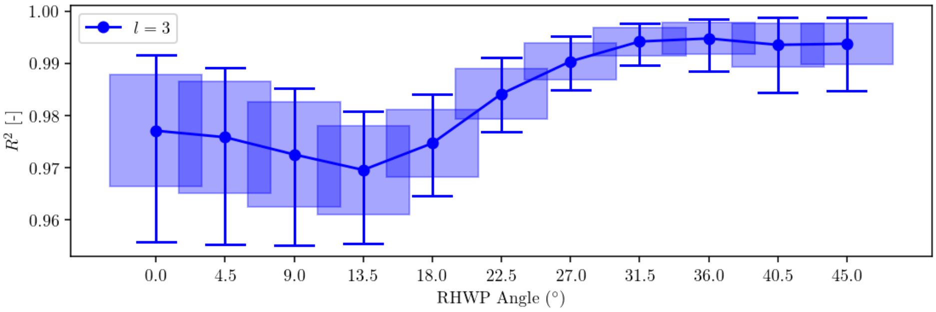

Figure 6.3: Box plot of the R^2 values for $\ell = 3$

From these box plots it can be seen that the measurements closely match the measurements, especially when the Gaussian beam starts to dominate, typically around a HWP orientation of $22.5°$. The difference in calculated R^2 between the vortex ($0°$ HWP) and the Gaussian ($45°$ HWP) extremes can largely be explained by the previously discovered inability of the SPP to produce a pure LG beam as discussed in section 5.3. The sensitivity analysis capabilities of the simulation tool were also used to increase the accuracy of alignment of the various components.

From these results, it can be concluded that while creating an LG beam is impossible with an SPP alone, it is still possible to create a highly accurately aligned setup and to closely match the theoretical outcome predicted by the simulation tool. This produced intensity distribution also has a $\geq 80\%$ power overlap with a pure LG beam of the same charge as the SPP, showing it to be a suitable replacement.

6.3. Communication performance

Given that the beam produced by this setup does not match the LG beam envisioned by the previous paper [1], it is important to apply the same algorithm in order to compare the outage probability of the obtained beam to both a standard Gaussian and to a pure LG beam. The same person who originally computed the power outage probabilities in [1] performed similar calculations on both the measured beam profile and the simulated fully developed vortex beam with the same link parameters. The power outage probability calculated here is the probability that due to jitter, the BER is so great that any bit error correction method or algorithm employed is unable to restore the signal.

	$\ell = 0$	$\ell = \{1,0\}$	$\ell = \{2,0\}$	$\ell = \{3,0\}$
Measurements	8.1×10^{-4}	5.1×10^{-5}	2.1×10^{-5}	1.5×10^{-5}
Simulation	8.8×10^{-4}	4.6×10^{-5}	6.0×10^{-6}	1.2×10^{-6}

Table 6.1: Power outage probability of different vortex beams as captured by the sensor

	$\ell = 0$	$\ell = \{1,0\}$	$\ell = \{2,0\}$	$\ell = \{3,0\}$
SPP-produced	5.2×10^{-7}	1.1×10^{-7}	5.0×10^{-8}	7.6×10^{-8}
LG	5.2×10^{-7}	9.6×10^{-9}	2.9×10^{-10}	1.4×10^{-10}

Table 6.2: Power outage probability of different vortex beams in the far field

Table 6.1 shows the optimum power outage probability obtained for both the measured beams and the beams simulated using the same propagation distance as achieved in the lab. The columns indicate the charges of the superposed beams making up the total intensity profile, with a pure Gaussian beam as a baseline on the left. Given that the power outage probability is a failure criterion, it is desirable to have this number be as low as possible.

From this table, it can be seen that all tested higher-order vortex beams captured by the sensor perform better than the fundamental Gaussian beam, often by an order of magnitude or more. The simulated beams also outperform their experimental counterparts, showing the presence of errors in the experimental setup.

However, certain limitations were observed during this analysis. The finite sensor size meant that part of the beam produced in the experiment was not captured, and thus clipping occurred. To keep the comparison between measurement and simulation consistent, the same sensor size was implemented for the simulation. The second limitation is that of the development of the beam. As discussed in section 5.3, the beam that could be produced in the lab was not yet fully developed. From figure 5.14, it can be seen that the R^2 of the simulated beam largely stops changing after 100m and it can thus be assumed that this distance would be needed to fully develop an experimental beam. This means that the results shown in table 6.1 are not completely valid for applications in space communication.

Table 6.2 shows the resulting power outage probability in the simulated far field compared to that of pure LG beams. Once again, the vortex beams produced by an SPP have a lower power outage probability than the Gaussian beam, but a beam superposition using a pure LG beam still outperforms the vortex beam superpositions. A potential reason for this could be that for the same w_0, the SPP vortex beam have a larger beam radius, which would increase the intensity fluctuation from the peaks of the vortex beam part to the Gaussian beam part, leading to an increased BER when jitter causes an instantaneous pointing error in between these peaks. However, perhaps somewhat decoupling the ratio between vortex and Gaussian from the HWP or decoupling the vortex and Gaussian beam divergences would allow the system to once again approximate the optimal profile.

These results show that even with the output of an SPP a superposed vortex and Gaussian beam can be produced which offers an intensity profile for use in Free-Space Optical Communication which when compared to a Gaussian profile allows for up to 20% power reduction under the same communication performance criteria or for an order of magnitude lower power outage probability when using the same amount of power.

7

Conclusion and next steps

In this thesis, an experimental investigation into the use of vortex beam combinations for inter-satellite Free-Space Optical Communication (FSOC) was conducted. Motivated by the theoretical predictions of a preceding paper [1] suggesting reduced sensitivity to transmitter jitter, an optical system was designed to generate adjustable superpositions of Gaussian and vortex beams generated by Spiral Phase Plates (SPPs). In addition, a pre-existing optical propagation program using Fourier optics was extended to model beam propagation, polarisation effects, and component alignment sensitivities for the experimental setup to be built.

Analysis of total power before and after the beam shaping indicates that the additional losses introduced by beam shaping components like the SPP and polarising beam splitters partially decrease the theoretical power savings predicted for superpositions of Gaussian and pure Laguerre-Gaussian beams, but still maintain potential gains when compared to a system using only a fundamental Gaussian beam.

While an SPP interacting with a Gaussian beam does not create a pure Laguerre-Gaussian beam but rather an infinite sum of these Laguerre-Gaussian beams, the experimental results show that high-quality Gaussian–vortex beam combinations can be generated with R^2 values over 0.9 when compared to simulated profiles. The obtained intensity profile also shows an integrated area overlap of over 80% when compared to the pure Laguerre-Gaussian electric field expression, meaning that over 80% of the obtained beam has its power within the pure Laguerre-Gaussian mode indicated by the charge of the SPPs.

Quantitative comparisons using beam waist estimation and coefficient-of-determination analysis confirm that the beam propagation program accurately captures the physical behaviour of the experimental setup. The experiments, alongside the beam propagation program, reveal that the setup is highly sensitive to displacement of the SPP, the misalignment of both beam paths and propagation distance, but relatively unaffected by minor rotational errors of the SPP and displacement of the beam as a whole.

Subjecting the obtained beam profile, both measured and simulated, to similar power outage probability analysis as the ideal Laguerre-Gaussian superpositions leads to the conclusion that while not being ideal, the produced vortex beam still performs better than a fundamental Gaussian beam would by itself by an order of magnitude or more reduction in said power outage probability.

Overall, this work provides experimental validation of key aspects of vortex beam generation for FSOC and increases the evidence for practical potential. While positive results were obtained, room for improvement is still present. More efficient and optimal components could be used, the propagation development further than 4m has been simulated but not yet verified, and a decoupling of beam radii between the beam paths could further improve the approximation of a pure Laguerre-Gaussian beam. As a next step, the experimental setup could be extended to include a controlled jitter simulation stage to directly measure communication performance metrics such as outage probability and bit error rate under dynamic pointing errors or the development of the beam at distances larger than those obtained in the lab could be compared to the intensity profiles produced by the simulation tool. Such experiments would enable a more complete assessment of the true robustness gains offered by non-Gaussian beam shaping in realistic spacecraft conditions and inform future FSOC system design choices.

Bibliography

[1] Badás Aldecocea, M., Piron, P., Bouwmeester, J., and Jerome, L., "On the optimum far-field irradiance distribution using Laguerre-Gaussian beams for intersatellite free-space optical communications," *Optics Express*, Vol. 32, 2024, pp. 31597–31620. https://doi.org/10.1364/OE.533250.

[2] Bromberg, J. L., "The Birth of the Laser," *Physics Today*, Vol. 41, 1988, pp. 26–33.

[3] Jeff, H., and News, O., "Lasers and the Glory Days of Industrial Research," , 2010. https://www.optica-opn.org/home/articles/volume_21/issue_5/features/lasers_and_the_glory_days_of_industrial_research.

[4] Kenichi, A., Yoshinori, A., Motokazu, S., Masahiro, T., Morio, T., Tetsuo, T., Seiji, K., and Koichi, S., "Performance evaluation of laser communication equipment onboard the ETS-VI satellite," *SPIE*, Vol. 2699, 1996.

[5] Shikatani, M., Yoshikado, S., Arimoto, Y., Suzuki, Y., Takahashi, Y., and Aruga, T., "Optical intersatellite link experiment between the earth station and ETS-VI," *Free-Space Laser Communication Technologies II*, Vol. 1218, edited by D. L. Begley and B. D. Seery, International Society for Optics and Photonics, SPIE, 1990, pp. 2 – 12. https://doi.org/10.1117/12.18169.

[6] Gotthard Oppenhäuser, E., "Perfect images transmitted via a laser link between Artemis and SPOT 4," , 2001. https://www.esa.int/Applications/Satellite_navigation/Perfect_images_transmitted_via_a_laser_link_between_Artemis_and_SPOT_4.

[7] Toni, T.-N., and Gotthard, O., "In Orbit test result of an Operational Optical Intersatellite Link between ARTEMIS and SPOT4, SILEX," *SPIE*, 2002.

[8] Davis, S., Lichter, M., and Raible, D., "Development and Characterization of a Small Spacecraft Electro-Optic Scanner for Free-Space Laser Communications," *NASA*, 2016.

[9] Xiaoli, S., John F., C., James C., S., and Arlin E., B., "MERCURY LASER ALTIMETER INSTRUMENT DESIGN, TESTING, AND PERFORMANCE VERIFICATION," *ILRC*, Vol. 22, International Laser Radar Conference, 2004, pp. 961 – 964.

[10] Fields, R., Lunde, C., Wong, R., Wicker, J., Kozlowski, D., Jordan, J., Hansen, B., Muehlnikel, G., Scheel, W., Sterr, U., Kahle, R., and Meyer, R., "NFIRE-to-TerraSAR-X Laser Communication Results: Satellite Pointing, Disturbances, and Other Attributes Consistent With Successful Performance," *Proc SPIE*, 2009, pp. 20–. https://doi.org/10.1117/12.820393.

[11] Smutny, B., Kaempfner, H., Muehlnikel, G., Sterr, U., Wandernoth, B., Heine, F., Hildebrand, U., Dallmann, D., Reinhardt, M., Freier, A., Lange, R., and Boehmer, K., "5.6 Gbps optical intersatellite communication link," *Proc SPIE*, Vol. 7199, 2009. https://doi.org/10.1117/12.812209.

[12] Overton, G., "NASA demonstrates laser communication between Earth and Lunar orbiter," , 2013. https://www.laserfocusworld.com/test-measurement/research/article/16560812/nasa-demonstrates-laser-communication-between-earth-and-lunar-orbiter.

[13] Sun, X., Skillman, D. R., Hoffman, E. D., Mao, D., McGarry, J. F., McIntire, L., Zellar, R. S., Davidson, F. M., Fong, W. H., Krainak, M. A., Neumann, G. A., Zuber, M. T., and Smith, D. E., “Free space laser communication experiments from Earth to the Lunar Reconnaissance Orbiter in lunar orbit,” *Opt. Express*, Vol. 21, No. 2, 2013, pp. 1865–1871. https://doi.org/10.1364/OE.21.001865.

[14] Belz, L., “Optical data link successfully demonstrated between fighter plane and ground station,” , 2013. https://web.archive.org/web/20131230233648/http://www.cassidian.com/en_US/web/guest/optical-data-link-successfully-demonstrated.

[15] Sven, M., and Ahmed, A.-M., “Laser terminals and ground stations for LEO missions - Status, way forward and feedback to ScyLight Workplan,” , 2017. https://connectivity.esa.int/sites/default/files/AM%2002_20170712_ViaLight_LaserComms_Muncheberg.pdf.

[16] NASA, “OPALS: Light Beams Let Data Rates Soar,” , 2014. https://www.jpl.nasa.gov/news/opals-light-beams-let-data-rates-soar/.

[17] ESA, “Laser link offers high-speed delivery,” , 2014. https://www.esa.int/Applications/Observing_the_Earth/Copernicus/Sentinel-1/Laser_link_offers_high-speed_delivery.

[18] Zech, H., Heine, F., Tröndle, D., Seel, S., Motzigemba, M., Meyer, R., and Philipp-May, S., “LCT for EDRS: LEO to GEO Optical communications at 1,8 Gbps between Alphasat and Sentinel 1a,” *SPIE*, Vol. 9647, 2015. https://doi.org/10.1117/12.2196273.

[19] JAXA, “Small Optical Link for International Space Station (SOLISS) Succeeds in Bidirectional Laser Communication Between Space and Ground Station - Optical ground station receives high-definition images from the International Space Station via Ethernet -,” , 2020. https://global.jaxa.jp/press/2020/04/20200423-1_e.html.

[20] Komatsu, H., Ohta, S., Yamazoe, H., Kubo, Y., Nakao, T., Ito, T., Koda, D., Sawada, H., Ikeda, T., Munemasa, Y., Kunimori, H., Kubooka, T., Toyoshima, M., and Iwamoto, K., “The pointing performance of the optical communication terminal, SOLISS in the experimentation of bidirectional laser communication with an optical ground station,” *Free-Space Laser Communications XXXIII*, Vol. 11678, edited by H. Hemmati and D. M. Boroson, International Society for Optics and Photonics, SPIE, 2021, p. 116780F. https://doi.org/10.1117/12.2577067.

[21] Riesing, K., Bilyeu, B., Chang, J., Garg, A., Gilbert, N., Horvath, A., Murphy, D., Nowak, W., Reeve, R., Robinson, B., Schieler, C., and Wang, J., “TBIRD: Two years demonstrating 200 Gbps optical downlink,” *IEEE Journal of Selected Topics in Quantum Electronics*, Vol. PP, 2025, pp. 1–12. https://doi.org/10.1109/JSTQE.2025.3616273.

[22] NASA, “NASA’s Optical Comms Demo Transmits Data Over 140 Million Miles,” , 2024. https://www.nasa.gov/missions/psyche-mission/nasas-optical-comms-demo-transmits-data-over-140-million-miles.

[23] Meenehan, S., Velasco, A., Wright, M., Beregovski, Y., Brewer, M., Buehlman, W., Richard, N., Alerstam, E., Biswas, A., Rogalin, R., Ortiz, G., Garkanian, V., Matthews, K., Allmaras, J., and Srinivasan, M., “Operational results from the deep space optical communications project ground laser transmitter,” *Free-Space Laser Communications XXXVII*, Vol. 13355, edited by H. Hemmati and B. S. Robinson, International Society for Optics and Photonics, SPIE, 2025, p. 133550K. https://doi.org/10.1117/12.3041400.

[24] Carrasco-Casado, A., Toyoshima, M., Do, P. X., Kolev, D., Hosonuma, T., Shiratama, K., Kunimori, H., Trinh, P. V., Abe, Y., and Nakasuka, S., “Intersatellite-Link Demonstration Mission between CubeSOTA (LEO CubeSat) and ETS9-HICALI (GEO Satellite),” *2019 IEEE International Conference on Space Optical Systems and Applications (ICSOS)*, IEEE, 2019, p. 1–5. https://doi.org/10.1109/icsos45490.2019.8978975.

[25] NASA, “LunaNet: Empowering Artemis with Communications and Navigation Interoperability,” , 2025. https://www.nasa.gov/humans-in-space/lunanet-empowering-artemis-with-communications-and-navigation-interoperability/.

[26] Atomics, G., “General Atomics and Kepler Communications Successfully Demonstrate Air-to-Space Optical Communications Capability,” , 2025. https://www.ga.com/ga-and-kepler-communications-successfully-demonstrate-air-to-space-optical-communications-capability.

[27] ITU, “ITU-R: Managing the radio-frequency spectrum for the world,” , 2025. https://www.itu.int/en/mediacentre/backgrounders/Pages/itu-r-managing-the-radio-frequency-spectrum-for-the-world.aspx.

[28] Parker, M., “Chapter 12 - Error Correction Coding,” *Digital Signal Processing 101*, edited by M. Parker, Newnes, Boston, 2010, pp. 125–142. https://doi.org/https://doi.org/10.1016/B978-1-85617-921-8.00016-X.

[29] cafe, R., “Electronic Warfare and Radar Systems Engineering Handbook - Antenna Introduction / Basics -,” , 2025. https://www.rfcafe.com/references/electrical/ew-radar-handbook/antenna-introduction-basics.htm.

[30] Gentec-eo, “The laser wavelength chart explained,” , 2022. https://www.gentec-eo.com/blog/the-laser-wavelength-chart-explained.

[31] Badas Aldecocea, M., Piron, P., Bouwmeester, J., Loicq, J., Kuiper, J., and Gill, E., “Opto-thermo-mechanical phenomena in satellite free-space optical communications: survey and challenges,” *Optical Engineering*, Vol. 63, No. 4, 2023, pp. 1–29. https://doi.org/10.1117/1.OE.63.4.041206.

[32] Ambrosi, R., and Denby, M., “The effect of radiation damage on optical CCDs operating in time-delay integration mode,” *Nuclear Instruments and Methods in Physics Research Section A: Accelerators, Spectrometers, Detectors and Associated Equipment*, Vol. 547, No. 2, 2005, pp. 346–358. https://doi.org/https://doi.org/10.1016/j.nima.2005.03.149.

[33] LaBel, K. A., Marshall, C. J., Marshall, P. W., Luers, P. J., Reed, R. A., Ott, M. N., Seidleck, C. M., and Andrucyk, D. J., “On the Suitability of Fiber Optic Data Links in the Space Radiation Environment: A Historical and Scaling Technology Perspective,” *IEEE*, 2015.

[34] Popoola, W., Ghassemlooy, Z., Lee, C., and Boucouvalas, A., “Scintillation effect on intensity modulated laser communication systems—a laboratory demonstration,” *Optics & Laser Technology*, Vol. 42, No. 4, 2010, pp. 682–692. https://doi.org/https://doi.org/10.1016/j.optlastec.2009.11.011.

[35] Frijns, J. J. M., “EXPERIMENTAL VERIFICATION OF BEAM WANDER, BEAM SPREAD AND SCINTILLATION IN AN OPTICAL LASER LINK THROUGH A TURBULENT ATMOSPHERE,” , 2023. Delft University of Technology.

[36] Aliverti, M., Pariani, G., Riva, M., Saggin, B., and Tarabini, M., “Mechanical alignment of optical systems: practical limits and accuracy estimation,” *SPIE*, 2018, p. 153. https://doi.org/10.1117/12.2313819.

[37] Thorlabs, “Protected Aluminum Mirrors,” , 2025. https://www.thorlabs.com/newgrouppage9.cfm?objectgroup_id=264.

[38] Thorlabs, “N-BK7 Bi-Convex Lenses, Uncoated,” , 2025. https://www.thorlabs.com/newgrouppage9.cfm?objectgroup_id=4847&pn=LB1676.

[39] Optics, E., “Chromatic and Monochromatic Optical Aberrations,” , 2025. https://www.edmundoptics.com/knowledge-center/application-notes/optics/chromatic-and-monochromatic-optical-aberrations/?srsltid=AfmBOoqbn_SAhIby1koORC6abof905cx-K99Rs11-_xlQq8XWew21Jce.

[40] Wang, X., Li, C., Jia, J., Wu, J., Shu, R., Zhang, L., and Wang, J., “Angular micro-vibration of the Micius satellite measured by an optical sensor and the method for its suppression,” *Appl. Opt.*, Vol. 60, No. 7, 2021, pp. 1881–1887. https://doi.org/10.1364/AO.416811.

[41] Wittig, M., van Holtz, L., Tunbridge, D. E. L., and Vermeulen, H. C., “In-orbit measurements of microaccelerations of ESA’s communication satellite Olympus,” *Photonics West - Lasers and Applications in Science and Engineering*, 1990, pp. 1–1.

[42] Toyoshima, M., Takayama, Y., Kunimori, H., Jono, T., and Yamakawa, S., “In-orbit measurements of spacecraft microvibrations for satellite laser communication links,” *Optical Engineering - OPT ENG*, Vol. 49, 2010. https://doi.org/10.1117/1.3482165.

[43] Arnon, S., “Minimization of outage probability of WiMAX link supported by laser link between a high-altitude platform and a satellite,” *J. Opt. Soc. Am. A*, Vol. 26, No. 7, 2009, pp. 1545–1552. https://doi.org/10.1364/JOSAA.26.001545.

[44] Zhu, Y., Xu, G., Gao, M., Chu, H., and Song, Z., “Average bit-error rate analysis of an inter-satellite optical communication system under the effect of perturbations,” *Opt. Express*, Vol. 32, No. 21, 2024, pp. 36796–36810. https://doi.org/10.1364/OE.533202.

[45] Farid, A. A., and Hranilovic, S., “Outage Capacity Optimization for Free-Space Optical Links With Pointing Errors,” *Journal of Lightwave Technology*, Vol. 25, No. 7, 2007, pp. 1702–1710. https://doi.org/10.1109/JLT.2007.899174.

[46] Toyoshima, M., Jono, T., Nakagawa, K., and Yamamoto, A., “Optimum divergence angle of a Gaussian beam wave in the presence of random jitter in free-space laser communication systems,” *J. Opt. Soc. Am. A*, Vol. 19, No. 3, 2002, pp. 567–571. https://doi.org/10.1364/JOSAA.19.000567.

[47] Zaman, I. U., and Boyraz, O., “Impact of receiver architecture on small satellite optical link in the presence of pointing jitter,” *Appl. Opt.*, Vol. 59, No. 32, 2020, pp. 10177–10184. https://doi.org/10.1364/AO.409144.

[48] Lu, Z., Guo, Z., Fan, M., Guo, M., Li, C., Yao, Y., Zhang, H., Lin, W., Liu, H., and Liu, B., “Tunable Bessel Beam Shaping for Robust Atmospheric Optical Communication,” *Journal of Lightwave Technology*, Vol. 40, No. 15, 2022, pp. 5097–5106. https://doi.org/10.1109/JLT.2022.3172134.

[49] Zhu, L., Wang, A., Deng, M., Lu, B., and Guo, X., “Free-space optical communication with quasi-ring Airy vortex beam under limited-size receiving aperture and atmospheric turbulence,” *Opt. Express*, Vol. 29, No. 20, 2021, pp. 32580–32590. https://doi.org/10.1364/OE.435863.

[50] Yang, D., Yu, Z., Wang, W., Hu, Z.-D., and Zhu, Y., “Underwater entanglement propagation of auto-focusing Airy beams,” *Opt. Express*, Vol. 32, No. 4, 2024, pp. 4887–4901. https://doi.org/10.1364/OE.510758.

[51] Siems, M. P., Thomas, J. U., Gross, H., Schöneberg, A., and Nolte, S., “Avoiding the tip: spiral optics for robust high power beam shaping of Bessel beams,” *Opt. Express*, Vol. 33, No. 7, 2025, pp. 15415–15422. https://doi.org/10.1364/OE.547789.

[52] Bae, J. Y., Jeon, C., Pae, K. H., Kim, C. M., Kim, H. S., Han, I., Yeo, W.-J., Jeong, B., Jeon, M., Lee, D.-H., Kim, D. U., Hyun, S., Hur, H., Lee, K.-S., Kim, G. H., Chang, K. S., Choi, I. W., Nam, C. H., and Kim, I. J., “Generation of low-order Laguerre-Gaussian beams using hybrid-machined reflective spiral phase plates for intense laser-plasma interactions,” *Results in Physics*, Vol. 19, 2020, p. 103499. https://doi.org/https://doi.org/10.1016/j.rinp.2020.103499.

[53] Ruffato, G., Carli, M., Massari, M., and Romanato, F., “Spiral phase plates for the generation of high-order Laguerre-Gaussian beams with non-zero radial index,” *Proceedings of SPIE*, Vol. 9379, 2015. https://doi.org/10.1117/12.2079471.

[54] Sueda, K., Miyaji, G., Miyanaga, N., and Nakatsuka, M., “Laguerre-Gaussian beam generated with a multilevel spiral phase plate for high intensity laser pulses,” *Opt. Express*, Vol. 12, No. 15, 2004, pp. 3548–3553. https://doi.org/10.1364/OPEX.12.003548.

[55] Photonics, V., “Vortex Lenses - Spiral Phase Plates,” , 2020. https://vortex-photonics.de/vortex-lenses-spiral-phase-plates.html.

[56] Campbell, G., Hage, B., Buchler, B., and Lam, P. K., “Generation of high-order optical vortices using directly machined spiral phase mirrors,” *Appl. Opt.*, Vol. 51, No. 7, 2012, pp. 873–876. https://doi.org/10.1364/AO.51.000873.

[57] Wang, J., Padgett, M. J., Ramachandran, S., Lavery, M. P., Huang, H., Yue, Y., Yan, Y., Bozinovic, N., Golowich, S. E., and Willner, A. E., “Chapter 12 - Multimode Communications Using Orbital Angular Momentum,” *Optical Fiber Telecommunications (Sixth Edition)*, edited by I. P. Kaminow, T. Li, and A. E. Willner, Optics and Photonics, Academic Press, Boston, 2013, sixth edition ed., pp. 569–615. https://doi.org/https://doi.org/10.1016/B978-0-12-396960-6.00012-2.

[58] Thorlabs, “WPH10M-532 - Ø1” Zero-Order Half-Wave Plate, SM1-Threaded Mount, 532 nm,” , 2000. https://www.thorlabs.com/thorproduct.cfm?partnumber=WPH10M-532.

[59] Photonics, R., “Resonator Modes,” , 2021. https://www.rp-photonics.com/resonator_modes.html.

[60] Optics, E., “Laser Beam Shaping Overview,” , 2025. www.edmundoptics.com/knowledge-center/application-notes/optics/laser-beam-shaping-overview.

[61] Dickey, F. M., Weichman, L. S., and Shagam, R. N., “Laser Beam Shaping Techniques,” *U.S. Department of Defense*, 2000.

[62] Moore, D., “Projected Pinhole Diffraction,” *Department of Physics, California Polytechnic University SLO*, 2011.

[63] Bonomo, M., “A brief study of pinhole diffraction,” , 2021. https://www.stonybrook.edu/laser/_melia/miniproject.html.

[64] Khadley, “Thin lenses,” , 2020. http://www.khadley.com/courses/physics/ph_212/topics/rayOptics/lenses.html.

[65] Thorlabs, “Mounted Axicons, UV Fused Silica,” , 2020. https://www.thorlabs.com/newgrouppage9.cfm?objectgroup_id=16616.

[66] Hermerschmidt, A., Eichler, H. J., Teiwes, S., and Schwartz, J., “Design of diffractive beam-shaping elements for nonuniform illumination waves,” *Diffractive and Holographic Device Technologies and Applications V*, Vol. 3291, edited by I. Cindrich and S. H. Lee, International Society for Optics and Photonics, SPIE, 1998, pp. 40 – 48. https://doi.org/10.1117/12.310592.

[67] Katz, S., Kaplan, N., and Grossinger, I., “Using Diffractive Optical Elements: DOEs for beam shaping - fundamentals and applications,” *Laser Technik Journal*, Vol. 15, 2018, pp. 29–32. https://doi.org/10.1002/latj.201800021.

[68] Pampaloni, F., and Enderlein, J., “Gaussian, Hermite-Gaussian, and Laguerre-Gaussian beams: A primer,” *arXiv*, 2004.

[69] Thorlabs, “Zero-Order Vortex Half-Wave Retarders,” , 2020. https://www.thorlabs.com/newgrouppage9.cfm?objectgroup_id=9098.

[70] Kovalev, A. A., Kotlyar, V. V., and Porfirev, A. P., “Optical trapping and moving of microparticles by using asymmetrical Laguerre–Gaussian beams,” *Opt. Lett.*, Vol. 41, No. 11, 2016, pp. 2426–2429. https://doi.org/10.1364/OL.41.002426.

[71] Trichili, A., Mhlanga, T., Naidoo, D., Dudely, A., Zghal, M., and Forbes, A., “Laguerre Gaussian beam multiplexing through turbulence,” *SPIE*, Vol. 9194, 2014, pp. 0–0. https://doi.org/10.1117/12.2062217.

[72] Rubinsztein-Dunlop, H., Forbes, A., Berry, M. V., Dennis, M. R., Andrews, D. L., Mansuripur, M., Denz, C., Alpmann, C., Banzer, P., Bauer, T., Karimi, E., Marrucci, L., Padgett, M., Ritsch-Marte, M., Litchinitser, N. M., Bigelow, N. P., Rosales-Guzmán, C., Belmonte, A., Torres, J. P., Neely, T. W., Baker, M., Gordon, R., Stilgoe, A. B., Romero, J., White, A. G., Fickler, R., Willner, A. E., Xie, G., McMorran, B., and Weiner, A. M., “Roadmap on structured light,” *Journal of Optics*, Vol. 19, No. 1, 2016, p. 013001. https://doi.org/10.1088/2040-8978/19/1/013001.

[73] Paschotta, R., “Hermite–Gaussian Modes,” RP Photonics Encyclopedia, Jan 2008. https://doi.org/10.61835/oqg”title=”Thislinkwillreloadthecurrentpage., https://www.rp-photonics.com/hermite_gaussian_modes.html.

[74] Chu, S.-C., Chen, Y.-T., Tsai, K.-F., and Otsuka, K., “Generation of high-order Hermite-Gaussian modes in end-pumped solid-state lasers for square vortex array laser beam generation,” *Opt. Express*, Vol. 20, No. 7, 2012, pp. 7128–7141. https://doi.org/10.1364/OE.20.007128.

[75] Meyrath, T. P., Schreck, F., Hanssen, J. L., Chuu, C. S., and Raizen, M. G., “A high frequency optical trap for atoms using Hermite-Gaussian beams,” *Opt. Express*, Vol. 13, No. 8, 2005, pp. 2843–2851. https://doi.org/10.1364/OPEX.13.002843.

[76] Singh, S. K., Haginaka, H., Jackin, B. J., Kinashi, K., Tsutsumi, N., and Sakai, W., “Generation of Ince–Gaussian Beams Using Azocarbazole Polymer CGH,” *Journal of Imaging*, Vol. 8, No. 5, 2022. https://doi.org/10.3390/jimaging8050144.

[77] Bandres, M. A., and Gutiérrez-Vega, J. C., “Ince–Gaussian modes of the paraxial wave equation and stable resonators,” *J. Opt. Soc. Am. A*, Vol. 21, No. 5, 2004, pp. 873–880. https://doi.org/10.1364/JOSAA.21.000873.

[78] Bandres, M., and Gutierrez Vega, J., “Ince–Gaussian beams,” *Optics Letters*, Vol. 29, 2004, pp. 144–146. https://doi.org/10.1364/OL.29.000144.

[79] Aguirre-Olivas, D., nor, G. M.-V., de-la Llave, D. S., and Arrizón, V., “Efficient generation of Hermite–Gauss and Ince–Gauss beams through kinoform phase elements,” *Appl. Opt.*, Vol. 54, No. 28, 2015, pp. 8444–8452. https://doi.org/10.1364/AO.54.008444.

[80] Baghdasaryan, B., and Fritzsche, S., “Enhanced entanglement from Ince-Gaussian pump beams in spontaneous parametric down-conversion,” *Phys. Rev. A*, Vol. 102, 2020, p. 052412. https://doi.org/10.1103/PhysRevA.102.052412.

[81] Sakpal, S., Milione, G., Li, M.-J., Nouri, M., Shahoei, H., LaFave, T., Ashrafi, S., and MacFarlane, D., “Stability of Ince-Gaussian beams in elliptical core few-mode fibers,” *Opt. Lett.*, Vol. 43, No. 11, 2018, pp. 2656–2659. https://doi.org/10.1364/OL.43.002656.

[82] M., G., and S., Y., “single-cell biological lasers,” *Nature Photon*, 2011, pp. 406–410.

[83] Yu, Y., Chen, Y., Wang, C., Wang, J., Sun, Z., Cao, M., Gao, H., and Li, F., “Optical storage of Ince–Gaussian modes in warm atomic vapor,” *Opt. Lett.*, Vol. 46, No. 5, 2021, pp. 1021–1024. https://doi.org/10.1364/OL.414762.

[84] Yang, Y., Ren, Y., Chen, M., Arita, Y., and Rosales-Guzmán, C., “Optical trapping with structured light: a review,” *Advanced Photonics*, Vol. 3, No. 3, 2021, p. 034001. https://doi.org/10.1117/1.AP.3.3.034001.

[85] Kalkman, J., “Advanced optical imaging,” , 2022. https://qiweb.tudelft.nl/aoi/frontmatter.html.

[86] Paschotta, R., “Fourier Optics,” RP Photonics Encyclopedia, 2019. https://doi.org/10.61835/i0t”title=”Thislinkwillreloadthecurrentpage., https://www.rp-photonics.com/fourier_optics.html.

[87] Adam, A. J., and Urbach, H. P., *BSc Optics: 2nd edition*, TU Delft OPEN Books, 2024. https://doi.org/10.59490/tb.91.

[88] Goodman, J. W., *Introduction to Fourier Optics*, 3rd ed., Roberts and Company Publishers, Englewood, Colorado, 2005.

[89] Zürich, E., “Chapter 7 - Angular Spectrum Representation,” , 2020. https://ethz.ch/content/dam/ethz/special-interest/itet/photonics-dam/documents/lectures/EandM/AngularSpectrumRepresentation.pdf.

[90] FOSCO, "Jones Vector Representation of Polarization States," , 2020. https://www.fiberoptics4sale.com/blogs/wave-optics/102087110-jones-vector-representation-of-polarization-states?srsltid=AfmBOooMvkCv3dtwnZRuZSWDrzsYBrsaUvWsoBglgOXgSaOr59JhUHb4.

[91] FOSCO, "Jones Matrix Calculus," , 2020. https://www.fiberoptics4sale.com/blogs/wave-optics/102261126-jones-matrix-calculus?srsltid=AfmBOoqzRksJcFE7GsNz9dyRQ0rMpitRYp998j_aoLSnhnKnFLae_dDT.

[92] Schmidt, J. D., *Numerical Simulation of Optical Wave Propagation with Examples in MATLAB*, SPIE, 2010, Chap. 7, pp. 115–130.

[93] Cross, E. W., "Alignment and focusing tolerance influences on optical performance," *SPIEE*, Vol. 40, 1983.

[94] Sun, J., Chen, Q., Zhang, Y., and Zuo, C., "Efficient positional misalignment correction method for Fourier ptychographic microscopy," *Biomed. Opt. Express*, Vol. 7, No. 4, 2016, pp. 1336–1350. https://doi.org/10.1364/BOE.7.001336.

[95] scipy, "scipy.optimize curve_fit," , 2000. https://docs.scipy.org/doc/scipy/reference/generated/scipy.optimize.curve_fit.html.

[96] Photonics, V., "Vortex Lenses - Spiral Phase Plates," , 2000. https://vortex-photonics.de/vortex-lenses-spiral-phase-plates.html.

[97] Thorlabs, "1.6 MP CMOS Compact Scientific Cameras," , 2000. https://www.thorlabs.com/newgrouppage9.cfm?objectgroup_id=13677&pn=CS165MU/M#ad-image-0.

[98] optics, E., "Z-Laser Green Focusable Diode Modules," , 2000. https://www.edmundoptics.eu/p/1mw-harsh-environment-green-diode/18589.

[99] Thorlabs, "PF10-03-G01-10 - Ø1" Protected Aluminum Mirror, 10 Pack," , 2000. https://www.thorlabs.com/thorproduct.cfm?partnumber=PF10-03-G01-10.

[100] Thorlabs, "LB1676 - N-BK7 Bi-Convex Lens, Ø1", f = 100.0 mm, Uncoated," , 2000. https://www.thorlabs.com/thorproduct.cfm?partnumber=LB1676.

[101] Thorlabs, "LB1471 - N-BK7 Bi-Convex Lens, Ø1", f = 50.0 mm, Uncoated," , 2000. https://www.thorlabs.com/thorproduct.cfm?partnumber=LB1471.

[102] Thorlabs, "NE10A - Ø25 mm Absorptive ND Filter, SM1-Threaded Mount, Optical Density: 1.0," , 2000. https://www.thorlabs.com/thorproduct.cfm?partnumber=%20NE10A.

[103] Thorlabs, "CCM1-PBS251/M - 30 mm Cage Cube-Mounted Polarizing Beamsplitter Cube, 420-680 nm, M4 Tap," , 2000. https://www.thorlabs.com/thorproduct.cfm?partnumber=CCM1-PBS251/M.

[104] Grigore, O.-V., and Craciun, A., "Method for exploring the topological charge and shape of an optical vortex generated by a spiral phase plate," *Optics & Laser Technology*, Vol. 141, 2021, p. 107098. https://doi.org/https://doi.org/10.1016/j.optlastec.2021.107098.

[105] Thorlabs, "Improving the Coupling Efficiency of Light into Single Mode Fibers," , 2000. https://www.thorlabs.com/newgrouppage9.cfm?objectgroup_id=14205.

[106] ephotonics, “What is Mode Field Diameter in Optical Fibers?” , 2000. https://ephotonics.com/mode-field-diameter-in-optical-fibers/.

[107] FOSCO, “What Are Optical Fiber Core Size, Mode Field Diameter and Numerical Aperture?” , 2000. https://www.fiberoptics4sale.com/blogs/archive-posts/95052742-what-are-optical-fiber-core-size-mode-field-diameter-and-numerical-aperture?srsltid=AfmBOoqeoh0Qy-I0eptwW92lkeMce2Joq-wf6Rd8NxSElkyMjfSRztIB.

[108] Demirbas, E., Serna-Otalvaro, S. F., and Deveney, E. F., “A free-space to fiber coupling lab as part of an optics and fiber kit being developed for undergraduate curricula and outreach,” *SPIEE*, Vol. 0, 2020, p. 0.

[109] RP-photonics, “Mode Matching,” , 2000. https://www.rp-photonics.com/mode_matching.html.

[110] Thorlabs, “460HP - Single Mode Optical Fiber, 450 - 600 nm, Ø125 µm Cladding,” , 2000. https://www.thorlabs.com/thorproduct.cfm?partnumber=460HP.

[111] Thorlabs, “F220FC-532 - 532 nm, f = 10.90 mm, NA = 0.25 FC/PC Fiber Collimation Pkg.” , 2000. https://www.thorlabs.com/thorproduct.cfm?partnumber=F220FC-532.

[112] Thorlabs, “TC12FC-532 - 532 nm, f=11.75 mm, NA=0.28, FC/PC Triplet Collimator,” , 2000. https://www.thorlabs.com/thorproduct.cfm?partnumber=TC12FC-532.

[113] Samuel J. Ling, W. M., Jeff Sanny, *University Physics*, OpenStax, 2025, Chap. 3, pp. 115–130.

[114] Massari, M., Ruffato, G., Gintoli, M., Ricci, F., and Romanato, F., “Fabrication and characterization of high-quality spiral phase plates for optical applications,” *Appl. Opt.*, Vol. 54, No. 13, 2015, pp. 4077–4083. https://doi.org/10.1364/AO.54.004077.

[115] Marín-Suárez, M., “Properties of Kummer beams in the structure of metamaterials,” *SPIE*, 2013, p. 888420. https://doi.org/10.1117/12.2027832.

[116] Thorlabs, “5-Axis Kinematic Mounts,” , 2000. https://www.thorlabs.com/5-axis-kinematic-mounts?pn=K5X1&tabName=Overview.

A

SPP vortex beam derivation

In this appendix, the analytical derivation for the output of an SPP interacting with a Gaussian beam is shown using the Fraunhofer approximation. This derivation was performed by PhD candidate and supervisor Mario Badás Aldecocea.

Starting from the Fraunhofer diffraction integral for a field $E(\rho', \theta')$ in the source plane:

$$E_{\mathsf{FF}}(\rho,\theta,z) = \frac{e^{ikz}e^{ik\frac{\rho^2}{2z}}}{i\lambda z}\int_0^{2\pi} d\theta' \int_0^{\infty} \rho' d\rho'\ E(\rho',\theta') e^{-i\frac{2\pi}{\lambda z}\rho\rho' \cos(\theta-\theta')}. \tag{A.1}$$

The field in question, a Gaussian beam encountering a Spiral Phase Plate is related as:

$$E(\rho',\theta') \propto\ e^{-\rho'^2/w_0^2} e^{i\ell\theta'}. \tag{A.2}$$

Combining both, we have

$$\begin{aligned} E_{\mathsf{FF}}(\rho,\theta,z) &\propto \frac{e^{ikz}e^{ik\frac{\rho^2}{2z}}}{i\lambda z}\int_0^{2\pi} d\theta' \int_0^{\infty} \rho' d\rho'\ C\ e^{-\rho'^2/w_0^2} e^{i\ell\theta'} e^{-i\frac{2\pi}{\lambda z}\rho\rho' \cos(\theta-\theta')} \\ &\propto \frac{e^{ikz}e^{ik\frac{\rho^2}{2z}}}{i\lambda z}\int_0^{\infty} \rho' d\rho'\ C\ e^{-\rho'^2/w_0^2} \int_0^{2\pi} d\theta' e^{i\ell\theta'} e^{-i\frac{2\pi}{\lambda z}\rho\rho' \cos(\theta-\theta')}. \end{aligned} \tag{A.3}$$

Using the Jacobi-Anger expansion,

$$e^{iz \cos\theta} \equiv \sum_{n=-\infty}^{\infty} i^n\, \mathcal{J}_n(z)\, e^{in\theta}$$

where $\mathcal{J}_n(z)$ is the Bessel function of the first kind of order n, we have that the integral over θ' in (A.3) can be solved as

$$\begin{aligned} \int_0^{2\pi} d\theta' e^{i\ell\theta'} e^{-i\frac{2\pi}{\lambda z}\rho\rho' \cos(\theta-\theta')} &= \int_0^{2\pi} d\theta' e^{i\ell\theta'} \left(\sum_{n=-\infty}^{\infty} i^n \mathcal{J}_n\left(-\frac{2\pi\rho\rho'}{\lambda z}\right) e^{in(\theta-\theta')} \right) \\ &= \sum_{n=-\infty}^{\infty} \left[i^n e^{in\theta} \mathcal{J}_n\left(-\frac{2\pi\rho\rho'}{\lambda z}\right) \int_0^{2\pi} d\theta' e^{i(\ell-n)\theta'} \right] \\ &= \sum_{n=-\infty}^{\infty} \left[i^n e^{in\theta} \mathcal{J}_n\left(-\frac{2\pi\rho\rho'}{\lambda z}\right)\ 2\pi\ \delta_{\ell,n} \right] \\ &= 2\pi\ i^{\ell} e^{i\ell\theta} \mathcal{J}_{\ell}\left(-\frac{2\pi\rho\rho'}{\lambda z}\right) \end{aligned}$$

Introducing this result in equation (A.3), we have that

$$\begin{aligned} E_{\mathsf{FF}}(\rho,\theta,z) &\propto 2\pi\; i^{\ell} e^{i\ell\theta}\; \frac{e^{ikz}e^{ik\frac{\rho^2}{2z}}}{i\lambda z} \int_0^\infty \rho' d\rho'\; e^{-\rho'^2/w_0^2} \mathcal{J}_\ell\left(-\frac{2\pi\rho\rho'}{\lambda z}\right) \\ &\propto 2\pi\; i^{\ell} e^{i\ell\theta}\; \frac{e^{ikz}e^{ik\frac{\rho^2}{2z}}}{i\lambda z} \frac{\pi^{3/2}\rho\; w_0^3}{4\lambda z} e^{-\frac{\pi^2\rho^2 w_0^2}{2\lambda^2 z^2}} \left(\mathcal{I}_{\frac{\ell-1}{2}}\left(\frac{\pi^2\rho^2 w_0^2}{2z^2\lambda^2}\right) - \mathcal{I}_{\frac{\ell+1}{2}}\left(\frac{\pi^2\rho^2 w_0^2}{2z^2\lambda^2}\right)\right) \\ &\propto (-i)^{\ell}\; e^{i\ell\theta}\; e^{ikz}e^{ik\frac{\rho^2}{2z}} e^{-\frac{\pi^2\rho^2 w_0^2}{2\lambda^2 z^2}} \frac{\rho}{2i\lambda^2 z^2} \left[\mathcal{I}_{\frac{\ell-1}{2}}\left(\frac{\pi^2\rho^2 w_0^2}{2\lambda^2 z^2}\right) - \mathcal{I}_{\frac{\ell+1}{2}}\left(\frac{\pi^2\rho^2 w_0^2}{2\lambda^2 z^2}\right)\right] \end{aligned} \tag{A.4}$$

where $\mathcal{I}_n(x)$ is the modified Bessel function of the first kind of order n.

B

Full diagram of the final setup

This appendix shows the full diagram of the setup in its final state.

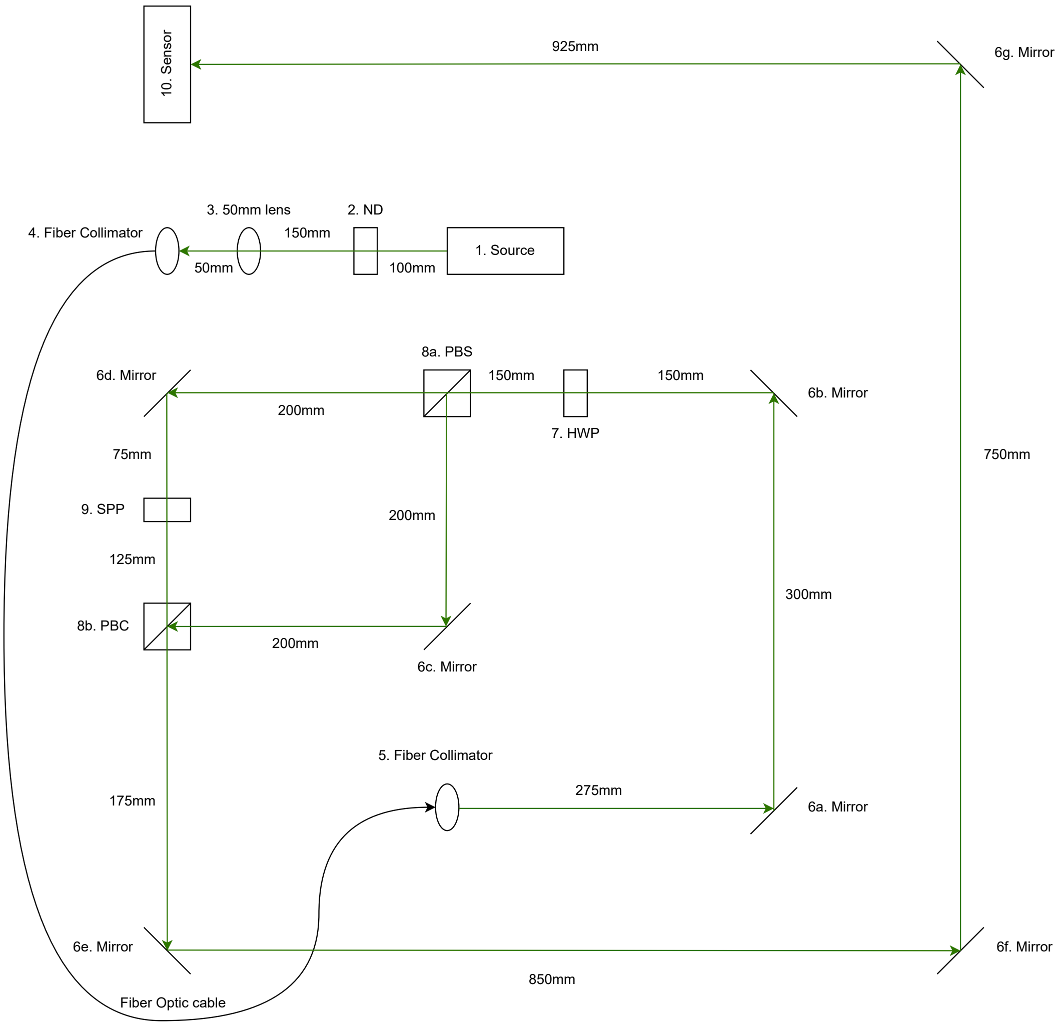

Figure B.1: Final setup diagram